Università degli Studi di Palermo

AREA QUALITÀ, PROGRAMMAZIONE E SUPPORTO STRATEGICO
SETTORE STRATEGIA PER LA RICERCA
UOR DOTTORATI

UNIVERSITÀ DEGLI STUDI DI PALERMO

Dottorato di Ricerca in Scienze Fisiche
Dipartimento di Fisica e Chimica-Emilio Segré
Settore Scientifico Disciplinare - FIS/05 - Astronomia e Astrofisica

Study on Supernova Remnants evolution and their gamma-ray emission

IL DOTTORE
ANTONIO TUTONE

IL COORDINATORE
PROF. GIOACCHINO MASSIMO PALMA

IL TUTOR
DR. GIANCARLO CUSUMANO

CO TUTOR
DR. ANTONINO D'Aì

CICLO XXXIV
ANNO CONSEGUIMENTO TITOLO 2022

Contents

Contents **2**

1 Supernova Remnants and their evolution **8**
1.1 Supernovae and their classification 9
1.1.1 Core-collapse Supernovae 10
1.2 Supernova Remnants and their classification 12
1.2.1 The evolution of Supernova Remnants 13
1.3 Shock waves 16
1.3.1 Particle Acceleration 21
1.4 The link between SNRs and SNe 22
1.4.1 State-of-the-art in the numerical simulation 23

2 Non-thermal Emission from SNRs **26**
2.1 γ-ray Observations of SNRs 28
2.1.1 Middle-aged SNRs 28
2.1.2 Young SNRs 30
2.2 Contents and Aims of the Thesis 32

3 γ-ray Instrumentation **33**
3.1 The *Fermi* instrument 34
3.1.1 The Large Area Telescope 35
3.1.2 The Gamma-Ray Burst Monitor 35
3.2 Cherenkov Telescopes 35
3.2.1 The ASTRI Mini-Array 36
3.2.2 The MAGIC telescopes 40

3.2.3 The VERITAS telescopes . . . 40
3.2.4 The HESS telescopes . . . 40

4 3D modeling from the onset of the SN to the full-fledged SNR 41
4.1 Introduction . . . 41
4.2 The numerical setup . . . 43
4.2.1 The initial conditions . . . 43
4.2.2 Modeling the evolution of the SNR . . . 45
4.2.3 Post-explosion large-scale anisotropy . . . 51
4.3 Results . . . 52
4.3.1 The case of a spherically symmetric explosion . . . 52
4.3.2 Effect of large-scale anisotropy . . . 56
4.3.3 Synthesis of X-ray emission . . . 65
4.4 Conclusions . . . 69

5 Multiple accelerated particle populations in the Cygnus Loop with *Fermi*-LAT 76
5.1 Introduction . . . 76
5.2 Observations and data reduction . . . 78
5.2.1 Gamma-ray band . . . 78
5.2.2 X-ray band . . . 80
5.2.3 Ultraviolet band . . . 81
5.2.4 Optical band . . . 82
5.2.5 Radio band . . . 83
5.3 Analysis . . . 83
5.3.1 Geometrical models . . . 86
5.3.2 Correlation with other wavelengths . . . 88
5.3.3 Spectral Analysis . . . 89
5.4 Modeling the Multiwavelength emission from the Cygnus Loop . . . 94
5.4.1 Ambient parameters . . . 95
5.4.2 Particle spectrum . . . 98
5.4.3 Non-radiative regions: DSA scenario . . . 100
5.4.4 Radiative regions: Re-acceleration of pre-existing ambient CRs 103

5.4.5 Modeling the entire Cygnus Loop 106

6 SNRs with the ASTRI Mini-Array 109

6.1 Introduction 109

6.2 SNRs of interest for the ASTRI Mini-Array 110

6.3 A PeVatron candidate: G106.3+2.7 113

6.3.1 Analysis and Results 114

6.4 A hadronic source: IC 443 118

6.4.1 Analysis and Results 118

7 Summary and Conclusions 120

8 Acknowledgments 126

Acronyms 127

List of Figures 130

Bibliography 138

Abstract

A Supernova (SN) is an astronomical event that occurs as the last evolution phase of a massive star, characterized by the collapse of the stellar core and the explosion of the star itself. After the explosion a heterogeneous nebula composed by the stellar debris in the form of gas and dust (the so called ejecta) termed Supernova Remnant (SNR) rapidly expands through the Circumstellar Medium (CSM), producing shocks which heat the expanding material and the CSM to temperatures of several million degrees and accelerate particles up to ultrarelativistic energies. The structure of the stellar progenitor and the complex phases in the evolution of the parent SN play an important role in determining the physical properties and morphology of the SNR. In particular, the remnant is expected to reflect the structure of the stellar progenitor and possible asymmetries and structures developed during the parent SN explosion. The remnant properties and environment also shape the spectrum of accelerated particles, which then diffuse through the Galactic Interstellar Medium (ISM).

This thesis is devoted to the study of SNRs, exploiting both multi-dimensional Magneto Hydrodynamics (MHD) models and the analysis of γ-ray emission. I focused on three main issues: the study of anisotropies in SN explosion and their effect on the remnant evolution, the analysis and interpretation of non-thermal emission from a middle-aged SNR and the analysis of a set of simulated observations with the Astrofisica con Specchi a Tecnologia Replicante Italiana (ASTRI) Mini-Array of two interesting SNRs to highlight the expected performance of the array and the scientific prospects of deep observations.

The manifold phases in the evolution of a Core-Collapse (CC) SN play an important role in determining the physical properties and morphology of the resulting SNR. Thus, the complex morphology of SNRs is expected to reflect possible asymmetries and structures developed during and soon after the SN explosion. I studied the gap be-

tween CC SN and their remnants by investigating how post-explosion anisotropies in the ejecta influence the structure and chemical properties of the remnant at later times. I performed three-dimensional magneto-hydrodynamical simulations starting soon after the SN event and following the evolution of the system in the CSM, which includes the wind of the stellar progenitor, for 5000 years, obtaining the physical scenario of a SNR. I focused the analysis on the case of a progenitor red supergiant of 19.8 $M_{\odot}$. I also investigated how a post-explosion large-scale anisotropy in the SN affects the ejecta distribution and the matter mixing of heavy elements in the remnant during the first 5000 years of evolution. In the case of a spherically symmetric SN explosion without large-scale anisotropies, the remnant roughly keeps memory of the original onion-like layering of ejecta soon after the SN event. Nevertheless, as the reverse shock hits the ejecta, the element distribution departs from a homologous expansion because of the slowing down of the outermost ejecta layers due to interaction with the reverse shock. In the case of a large-scale anisotropy developed after the SN, I found that the chemical stratification in the ejecta can be strongly modified and the original onion-like layering is not preserved. The anisotropy may cause spatial inversion of ejecta layers, for instance leading to Fe/Si-rich ejecta outside the O shell, and may determine the formation of Fe/Si-rich jet-like features that may protrude the remnant outline. The level of matter mixing and the properties of the jet-like feature are sensitive to the initial physical (density and velocity) and geometrical (size and position) initial characteristics of the anisotropy.

CSM is another important factor in determining the remnant evolution. A real case of a remnant whose physical properties have been affected by its environment is the Cygnus Loop.

The Cygnus Loop (G74.0-8.5) is a very well known nearby SNR in our Galaxy. Thanks to its large size, brightness and angular offset from the Galactic plane it has been studied in detail from radio to γ-ray. The γ rays, in the MeV-GeV band, probe the populations of energetic particles and their acceleration mechanisms at low shock speeds. I will present in Chapter 5 an analysis of the γ-ray emission detected by the Large Area Telescope onboard the *Fermi Gamma-ray Space Telescope* over 11 years in the Cygnus Loop region. I performed detailed morphological and spectral studies of the γ-ray emission toward the remnant from 100 MeV to 100 GeV, and compared it with X-ray, UV, optical and radio images. Thanks to the higher statistic with respect to the

previous studies I decomposed the emission from the remnant into two morphological components to model its non-thermal multi-wavelength emission. The extended γ-ray emission is well correlated with the thermal X-ray and UV emission of the SNR. Both components show a curved spectrum but the X-ray component is softer and more curved than the UV component, suggesting a different physical origin. The multiwavelength modeling of emission suggests that the non-thermal radio and γ-ray emission associated to the UV component is mostly due to the re-acceleration of pre-existing cosmic rays by radiative shocks in the adjacent clouds, while the non-thermal emission associated with the X-ray component arises from freshly accelerated cosmic rays.

A fundamental question in the particles acceleration mechanism in SNRs is the possibility of accelerating particles up to PeV energies. These particles emit γ-ray radiation in the TeV energy band that can only be detected by Cherenkov ground-based instruments, the so called imaging atmospheric Cherenkov telescopes (IACT). A new generation of IACT, such as ASTRI and CTA will explore the universe up to hundreds of TeV in the next future. The ASTRI Mini-Array will be composed of nine imaging atmospheric Cherenkov telescopes at the Observatorio del Teide site. The array will be best suited for astrophysical observations in the 0.5-200 TeV range with an angular resolution of few arcminutes and an energy resolution of $\sim 13\%$. I presented the expected results for two interesting SNRs: G106.3+2.7 and IC 443. The ASTRI Mini Array will allow to constrain the PeVatronic emission of the G106.3+2.7 and will significantly improve the spectral and morphological characterization of IC 443.

Chapter 1

Supernova Remnants and their evolution

In the final evolutionary stage of a massive star ($M > 8\ M_{\odot}$) the release of gravitational energy, of the order of $\simeq 10^{53}$ erg, due to the collapse of the innermost layers of the star, generates a rebound and an explosion that causes the ejection of the external stellar layers at very high velocities ($\simeq 10.000$ km/s) in the Circumstellar Medium (CSM) with a characteristic kinetic energy of $\simeq 10^{51}$ erg. These violent astronomical phenomena are called Supernova explosions (or supernovae, hereafter SNe). At the end of the process, a compact object (either a neutron star or a black hole) could be formed and the outer envelope is ejected in the surrounding medium. The relics of the progenitor star expelled at supersonic speed during the explosion are called ejecta. The supersonic expansion of the ejecta sweeps the environment surrounding the place of the explosion, causing the heating, compression, acceleration and chemical enrichment of the CSM and, in the later stages of the Interstellar Medium (ISM). The residual components of a SN and their subsequent interaction with the environment are collectively called Supernova Remnant (SNR).

SNRs play a central role in modern astrophysics, because they involve some aspects of physics (such as thermodynamics, magneto-hydrodynamics, gravitational theory and nuclear physics to name the most important) that are still of capital interest (especially when they are at play simultaneously and at extreme conditions of density, temperature and pressure), and because they enrich the Galactic medium of heavy elements and

energy. Moreover, SNRs are sources of primary interest for High Energy (HE) (radiation with photon energies of 100 keV to 100 GeV) and Very High Energy (VHE) (radiation with photon energies of 100 GeV to 100 TeV) Astrophysics: they are bright high energy radiation sources and they are thought to be the primary Cosmic Rays (CR) accelerators in the Galaxy (Blasi 2013; Amato 2014).

This thesis is aimed at studying the dynamical and physical properties of SNRs using the results from the numerical Magneto Hydrodynamics (MHD) simulation of SNR evolution and through the analysis of HE and VHE observations. This and next chapter is organized as follows: in Sect.1.1 I shortly describe the SN explosion mechanisms; the classification of SNRs is described in Sect.1.2; in Sect.1.3 I discuss the physics of shocks and their effects on the evolution of SNRs; in Chapter 2 I review the emission processes which occur in SNRs in the γ-rayband; finally, in Sect.2.2 I present the results of my research.

1.1 Supernovae and their classification

On average, SNe occur at a rate of ~ 2 per century in a typical spiral galaxy like our own (Vink 2012; Diehl et al. 2006), and every explosion produces a rich variety of observables such as neutrinos, cosmic rays and, probably, gravitational waves. In the course of the explosion, new elements are formed by explosive nucleosynthesis processes and the explosion scatters them into the interstellar space with other elements synthesized by nuclear burning and other processes previously occurred in the progenitor star. Although they are rare phenomena, the amount of the gravitational binding energy of the core of the original star transformed into kinetic energy amounts to approximately 10^{51} ergs, roughly 10 times the energy radiated by the Sun in its lifetime. The core collapses almost in free fall, approximately in a tenth of a second, so the energy release yields a luminosity up to 10^{54} erg s^{-1} (Longair 2011). Most of the gravitational energy is released, through the nuclear reactions, as neutrinos: 10^{53} ergs.

SNe can be divided into two main categories, type I and type II, (see Fig. 1.1) each with several sub-categories, based on their optical spectra (Longair 2011; Filippenko 1997).

- Type I SNe do not show hydrogen absorption lines in their spectra, because the

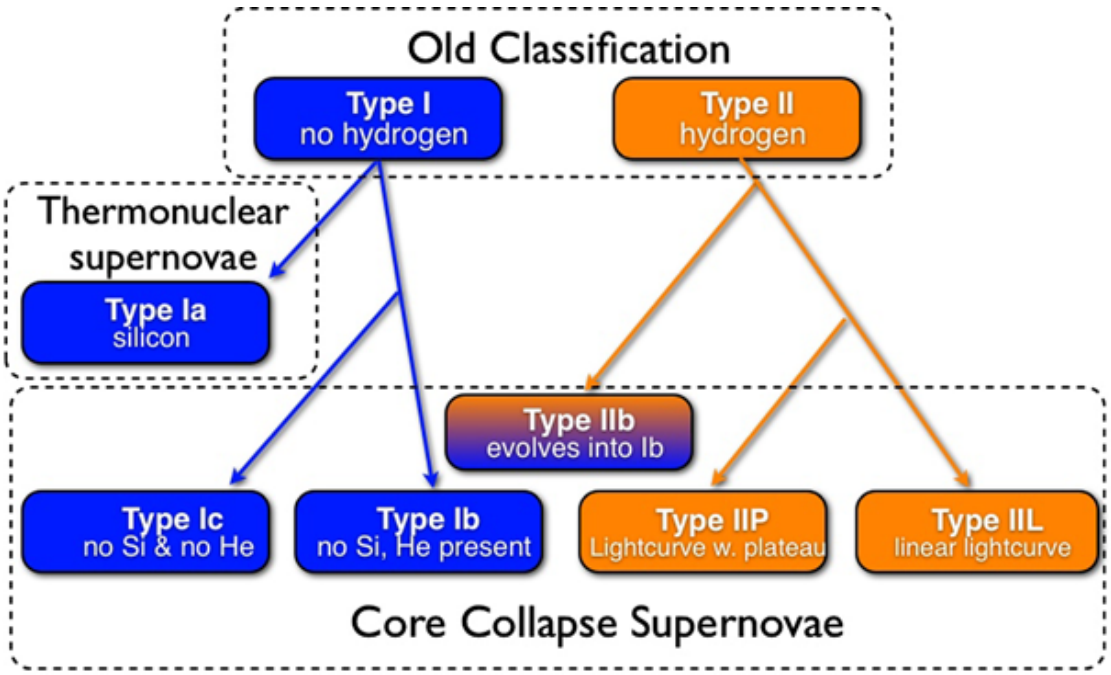

Figure 1.1: The classification of supernovae, based on optical spectroscopy and light-curve shape (Vink 2012).

progenitor star lacks the hydrogen-rich external layers as a result of past stellar wind mass loss or through binary interaction. Type I can be either core-collapse (see section 1.1.1) or thermonuclear SNe.

- Type II are exclusively core-collapse SNe which show hydrogen absorption in their spectra. The sub-division of the Type II class is based on a combination of two observational criteria: optical spectroscopy and light-curve shape (see Fig. 1.2).

1.1.1 Core-collapse Supernovae

The most massive stars, those with main sequence masses M$\geq$ 8M$_{\odot}$, end their life like Core-Collapse (CC) SNe.

The internal structure of the progenitors of these SNe are characterized by a sequence of almost concentric chemically homogeneous layers, each containing the products of the different consecutive nuclear burning stages, which occurred in different

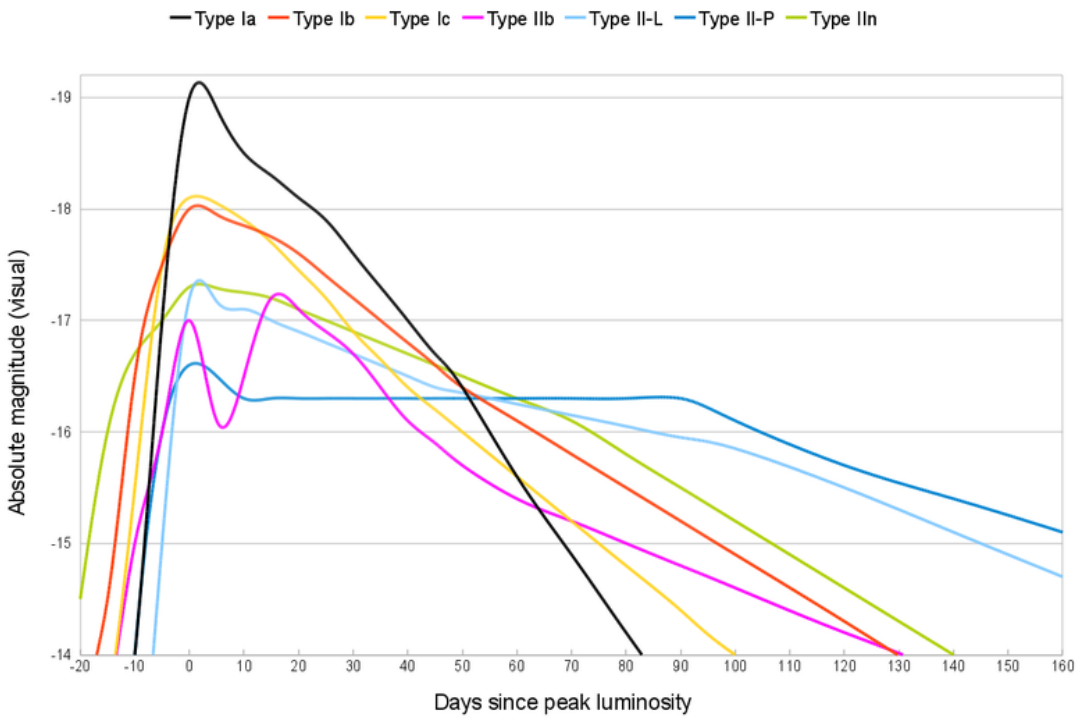

Figure 1.2: Bolometric light curves of representative SNe.

phases of the stars' life. From the core to the outer layers one expects: Fe, Si, O, C, He and then H.

When the iron core is generated as a product of nuclear burning, the final phase of the star's life begins, because no energy gain is possible from either fusion or fission of Fe. The less massive stars collapse into Neutron Star (NS), while the most massive can collapse into Black Hole (BH). The collapse of a star, caused by the vanishing of the pressure at the center of the star, may stop when a NS is formed; a shock wave is generated near the surface of the proto-NS and it accumulates energy because of the in-falling material. This energy is then released when the in-falling material is not enough to stop the expansion of the shock. Most of the gravitational energy released (E$\sim$ GM^2/R$_{NS}$ $\sim$ 10^{53} erg, with R$_{NS}$ $\sim$ 10 Km the NS radius) is in the form of neutrinos and they are responsible for triggering the SN explosion (see Hirata et al. (1987); Bionta et al. (1987)). The SN explosion mechanism itself, which requires that an energy $\geq$ 10^{51} erg is deposited in the outer layers, is not well understood (Vink 2012). The stellar mass thrown during the explosion, called ejecta, consists primarily of outer stellar material,

except for the innermost ejecta, which consist of explosive nucleosynthesis products, mostly Fe and Si-group elements. These elements are synthesized from the impact of protons and α-particles with heavy elements previously synthesized inside the star, in the innermost regions close to the collapsing core. Some of the explosive nucleosynthesis products are radioactive and the energy released by their decay (in particular the energy generated by the decay of $^{56}\mathrm{Ni} \rightarrow {}^{56}\mathrm{Co} \rightarrow {}^{56}\mathrm{Fe}$) heats the surrounding ejecta, providing a major imprint on the evolution of the supernova light curve (Barbarino et al. 2015; Huang et al. 2015). The yields of these elements depend sensitively on the details of the explosion, such as the mass cut (the boundary between material that accretes on the neutron star and material that is ejected), the explosion energy, the mass of the ejecta (and of the progenitor star) and the possible explosion asymmetries.

1.2 Supernova Remnants and their classification

The residual components of a SN explosion are collectively called Supernova Remnant (SNR). SNRs are important resources to study SNe; for example the presence of a NS inside the SNR makes it clear that the SNR must have had a core collapse origin, and also SNRs provide the best way to study the local population of SNe. But the most characteristic part of a SNR is the cloud of plasma, gas and dust of those elements mostly created during the life and the explosion of the star together with the interstellar medium in the star's neighborhood. The gas is shocked by the blast wave caused by the supersonic motion of the ejecta and by the reverse shock produced (see section 1.3) by the deceleration of the primary shock. It is possible to classify the SNRs on the basis of their morphology. Traditionally, this classification recognizes three classes: shell type, plerions, composite (Vink 2012).

- As the blast wave sweeps through the interstellar medium, a shell of plasma at several millions Kelvin is produced. These shell type SNRs are the most common in our Galaxy; their are characterized by a bright shell that surrounds the whole remnant (see Fig. 1.3a).

- Plerions (from Greek "$\pi\lambda\acute{\eta}\rho\eta\varsigma$"= full) SNRs are characterized by a nebula that is bright in the center, and does not show a shell (see Fig. 1.3b). The central brightness is typically associated with a NS, which, through its rotation, releases energy

and accelerates particles, in particular electrons and positrons, to ultrarelativistic energies.

- Composite SNRs are expected in remnants with an age less than ~ 20.000 yr and they are composed by a plerion surrounded by the SNR shock, which creates a shell (see Fig. 1.3c). This configuration evolves in time in a plerion morphology; a special case is the Crab Nebula, which although has less than 10^3 yrs has a plerion morphology.

1.2.1 The evolution of Supernova Remnants

The evolution of SNRs is usually divided in four phases, although this is a simplification and an idealization.

1. *Free-expansion phase* - The energy released by the explosion heats and pushes the external stellar layers, throwing them away with a velocity of $1 - 2 \cdot 10^4$ km s^{-1}. Assuming the gas expands spherically, its velocity is directly proportional to the radial distance from the centre and it does not decelerate as long as the mass of the interstellar medium invested by the shock wave (see sect. 1.3) is negligible with respect to that of the material ejected from the star. Assuming the temperature within the ejecta is uniform before the expansion, it decreases adiabatically according to the law

$$T \propto R^{-3(\gamma-1)} \tag{1.1}$$

where γ is the ratio between specific heats at constant pressure and constant volume, respectively. Since the expansion occurs with a highly supersonic velocity, a shock forms ahead of the ejecta. This shock heats, compresses, and accelerates the ambient medium (see section 1.3)

2. *Sedov-Taylor expansion phase* - When the mass of the shocked interstellar medium becomes greater than that of the ejecta the evolution of the remnant is described by Sedov-Taylor expansion. This model is based on the assumption that, under adiabatic conditions and spherical symmetry, the evolution of the remnant depends only on the energy of the explosion, E, and on the circumstellar medium density, ρ_0 (Longair 2011; Sedov 1959; Taylor 1950). The aim of this model is

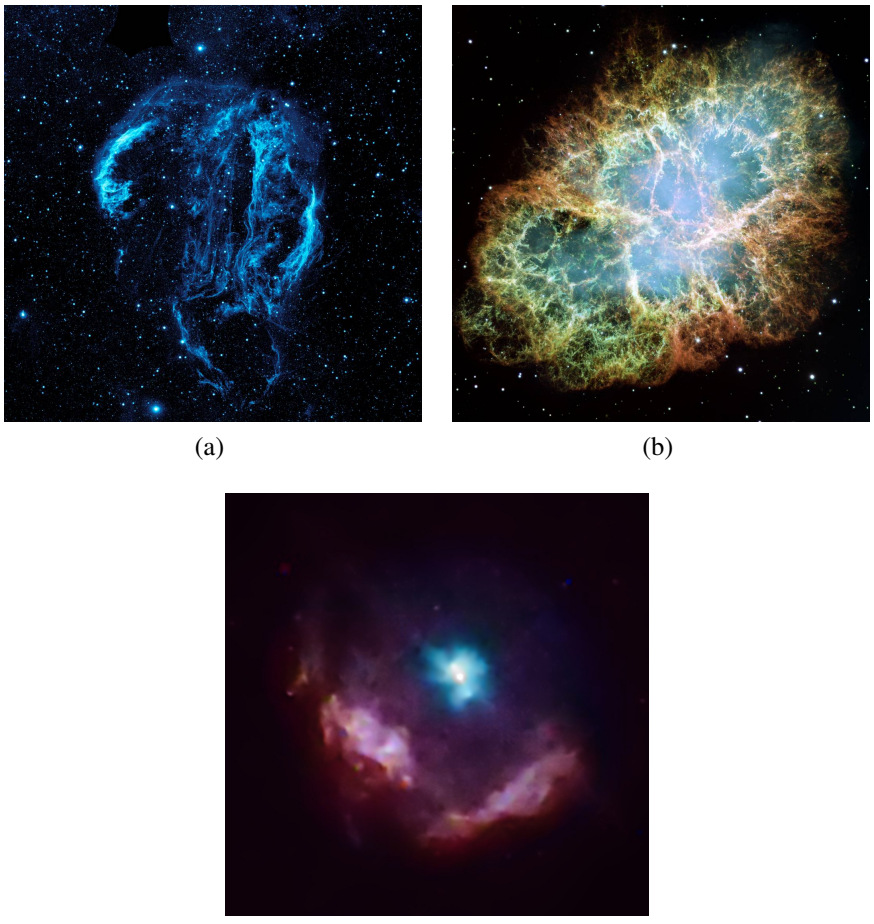

(a) (b)

(c)

Figure 1.3: Examples of SNRs morphology: a) Cygnus Loop, shell type SNR, b) Crab Nebula, plerion SNR, c) Kes 75, composite SNR.(Image Credit: NASA, ESA, J. Hester, A. Loll (ASU))

to obtain $r_s(t)$ and $v_s(t)$ that are the forward shock radius and velocity as a function of time. Through dimensional analysis, noting that the dimensions of $\frac{E}{\rho_0}$ are $[Lenght]^5[Time]^{-2}$ it is possible to conclude that:

$$r_s \propto \left(\frac{E}{\rho_0}\right)^{\frac{1}{5}} t^{\frac{2}{5}} \tag{1.2}$$

where r is the radial distance from the center of the explosion and t is the time. Deriving with respect to t, we obtain:

$$v_s \propto \left(\frac{E}{\rho_0}\right)^{\frac{1}{5}} t^{-\frac{3}{5}} \tag{1.3}$$

The outer shells of the expanding sphere are decelerated first and so the material inside the sphere catches up with the material in the outer layers. As the deceleration continues, the flow of gas into the outer layers becomes supersonic relative to the material inside the sphere itself and so a shock wave forms on the inner edge of the compressed outer layers (see Fig. 1.4). The formation of this internal shock wave has the effect of reheating strongly the matter in the outer shells. The net result is that, although the material inside the sphere cooled during the free-expansion phase, the gas is reheated by the conversion of a large fraction of the kinetic energy of expansion back into heat. The internal shock wave propagates back through the expanding gas towards the origin and in the process heats up all the ejected gas. A more detailed description can be found in McKee 1974. The internal shock structure is unstable to Rayleigh–Taylor instabilities which facilitate mixing between stellar debris and ISM.

3. *Radiative expansion phase* - As the remnant continues to expand, the temperature in the region behind the forward shock front, which now contains most of the expanding mass, drops below 10^6 K (corresponding to $v_s = v_{rad} \sim 200$ km s^{-1} Woltjer 1972) and cooling by line emission of heavy ions becomes important. During this phase the expansion is no longer adiabatic but radiative and the conservation of energy cannot be assumed. The evolution of the shock wave is now

governed by radial momentum conservation:

$$Mv_s = \frac{4\pi}{3}\rho_0 r_s^3 \frac{dr_s}{dt} = constant \tag{1.4}$$

knowing the age when the remnant enters the radiative phase, it is possible to estimate the value of the constant. It is possible to estimate the age t_{rad} when the remnant enters the radiative phase, using equations 1.2 and 1.3 since $v_{rad} = \frac{r_{rad}}{t_{rad}}$:

$$t_{rad} \sim 4.46 \times 10^4 \left(\frac{E_{51}}{n_H}\right)^{1/3} yr \tag{1.5}$$

$$r_{rad} \sim 23 \left(\frac{E_{51}}{n_H}\right)^{1/3} pc \tag{1.6}$$

where E_{51} is the explosion energy in units of 10^{51} erg and n_H the unshocked H density.

4. *Subsonic expansion phase* - The expansion eventually becomes subsonic, with $v < 20$ km s^{-1}, and the supernova remnant loses its identity melting with the ISM.

1.3 Shock waves

As already mentioned, the external stellar layers are thrown away by the SN explosion with a velocity of 1-2 $\cdot$ 10^4 km s^{-1}. Since the expansion is highly supersonic, a shock wave is characterized by abrupt variations in the density, temperature, and velocity in front of the expanding ejecta. The discontinuity is crossed by a flow of mass, momentum and energy described by a set of conservation relations, the Rankine-Hugoniot (Landau & Lifshitz 1959) conditions, discussed below, a specialized form of conservation laws of mass, momentum and energy (Eq. 1.10). Shocks in dense fluids occur over a few particle mean free paths. However, shock waves in the ISM propagates in a medium with very low density ($n \sim 1$ cm^{-3}) so that the mean free paths for particle-particle interactions are long compared to the typical size of shocks. As a consequence, SNR shock-heating process cannot be accomplished by particle-particle interactions, as it usually happens in denser media like Earth's atmosphere, but by interaction of

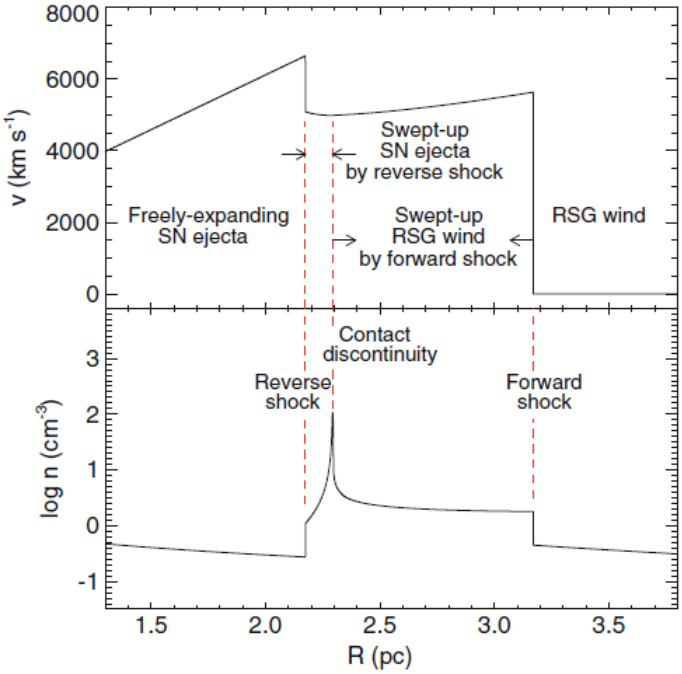

Figure 1.4: Spherically-symmetric hydrodynamic model of the Cas A SNR. Upper and lower frames show velocity and density profiles along the radial direction of the SNR at t = 330 year. The density profile of SN ejecta is composed of a inner flat portion and outer steep power-law portion. The ambient medium is RSG wind with a density profile of $\propto r^{-2}$ (Chevalier & Oishi 2003).

charged particles with the electromagnetic fields generated in plasma, often through turbulent processes. For this reason SNR shocks are collision-less shocks.

Let us take into account a propagating shock wave in the rest frame of the shock. The pre-shock conditions of density, velocity and temperature (ρ, v, T) are labelled by the subscript 1, while the subscript 2 labels the post-shock conditions. To derive the relations between the pre and post-shock conditions for a steady-state, plane-parallel shock ($\vec{v}$ perpendicular to shock front and fluid properties depend only on the distance from the shock) we consider the hydrodynamic equations for the conservation of mass, momentum and energy:

$$\frac{\partial \rho}{\partial t} + \vec{\nabla} \cdot (\rho \vec{v}) = 0 \tag{1.7}$$

$$\frac{\partial}{\partial t}(\rho \vec{v}) + \vec{\nabla} \cdot (\rho v^2 + p) = 0 \tag{1.8}$$

$$\frac{\partial}{\partial t}\left[\rho\left(\frac{1}{2}v^2 + \epsilon\right)\right] + \vec{\nabla} \cdot \left[\rho\left(\frac{1}{2}v^2 + \epsilon + \frac{p}{\rho}\right)\vec{v}\right] = 0 \tag{1.9}$$

where p is pressure and ϵ is energy in mass units and we ignored gravity and viscosity. Assuming steady-state and plane-parallel ($\frac{\partial}{\partial t} = 0, \frac{\partial}{\partial y} = 0, \frac{\partial}{\partial z} = 0, \frac{\partial}{\partial x} = \frac{d}{dx}$) we can obtain:

$$\frac{d}{dx}(\rho v) = 0 \tag{1.10a}$$

$$\rho v \frac{dv}{dx} = -\frac{dp}{dx} \tag{1.10b}$$

$$\frac{d}{dx}\left(\frac{\rho v^2 v}{2} + \rho \epsilon v\right) = -\frac{d}{dx}(p\rho) \tag{1.10c}$$

The equations 1.10 relating the fluid variables before and after a shock are known as Rankine-Hugoniot relations (Choudhuri 1998; Landau & Lifshitz 1959). The dimensionless quantity:

$$M_i = \frac{v_i}{c_i}, \quad i = 1, 2 \tag{1.11}$$

is known as the Mach number, where $c^2 = \frac{\gamma p}{\rho} = \frac{\gamma k T}{m}$ is the sound speed in the

medium of an ideal gas. Moreover, for an ideal gas, we have:

$$\epsilon + \frac{p}{\rho} = \frac{1}{\gamma - 1}\frac{p}{\rho} + \frac{p}{\rho} = \frac{\gamma p}{\rho(\gamma - 1)} = \frac{c^2}{\gamma - 1} \tag{1.12}$$

using these definitions, it is possible to solve the Rankine-Hugoniot relations and get:

$$\frac{\rho_2}{\rho_1} = \frac{v_1}{v_2} = \frac{(\gamma + 1)M_1^2}{(\gamma - 1)M_1^2 + 2} \tag{1.13a}$$

$$\frac{p_2}{p_1} = \frac{2\gamma M_1^2}{\gamma + 1} - \frac{\gamma - 1}{\gamma + 1} \tag{1.13b}$$

$$\frac{T_2}{T_1} = \frac{[2\gamma M_1^2 - (\gamma - 1)][(\gamma - 1)M_1^2 + 2]}{(\gamma + 1)^2 M_1^2} \tag{1.13c}$$

$$M_2^2 = \frac{2 + (\gamma - 1)M_1^2}{2\gamma M_1^2 - \gamma + 1}. \tag{1.13d}$$

In this way it is possible to connect the post-shock with the pre-shock quantities and the Mach number. It can be noticed that if $M_1 = 1$ the discontinuity cannot exist, while if $M_1 < 1$ the equations 1.13 give $v_1 < v_2$ and $T_1 > T_2$; in other words, the internal energy of the fluid would turn into kinetic energy with no other effect; but this is not possible for the second principle of thermodynamics because the entropy would decrease in an adiabatic transformation. So it always must be $M_1 > 1$. In the case of SNe, $M_1 \gg 1$ and relations 1.13 can be simplified as:

$$\frac{\rho_2}{\rho_1} = \frac{v_1}{v_2} = \frac{\gamma + 1}{\gamma - 1} \tag{1.14a}$$

$$\frac{p_2}{p_1} = \frac{2\gamma M_1^2}{\gamma + 1} \tag{1.14b}$$

$$\frac{T_2}{T_1} = \frac{2\gamma(\gamma - 1)M_1^2}{(\gamma + 1)^2} \tag{1.14c}$$

$$M_2^2 = \frac{(\gamma - 1)}{2\gamma} \tag{1.14d}$$

Thus, in the strong shock limit, the post-shock temperature and pressure can become extremely large, but the density ratio attains a maximum value of 4 for a mono-atomic

gas with $\gamma = \frac{5}{3}$, as it is typically the case for the interstellar medium. In the same way, assuming $M_1 = 1000$ one obtain a post-shock temperature 10^6 times bigger than pre-shock temperature. These results demonstrate how efficiently strong shock waves can heat gas to very high temperatures as it is found in SN explosions and SNRs. Moreover, Fig. 1.4 clearly shows how the shock velocity is strongly affected by the ambient density: the shock is faster in a low-density medium and slower in a high-density medium.

When the remnant enters the radiative phase the fluid properties right behind the shock front are still described by the previous relations. In the regions where the gas is able to radiate energy (the Radiative Relaxation Layer (RRL)) the fluid properties change to new values (v_3, ρ_3, T_3, p_3) further downstream. In the RRL, because of the drop of the temperature due to the emission of radiation, the density rise and, since $\rho v = constant$, the velocity decreases. This can be obtained by including in equations 1.10 the cooling term:

$$L(\rho, T) > 0 \tag{1.15}$$

combining the new equations we can write:

$$\frac{\left(\frac{\gamma p}{\rho}\right)^2 - v^2}{\gamma - 1}\frac{dv}{dx} = -L \tag{1.16}$$

Since the post-shock flow is subsonic ($v < \frac{\gamma p}{\rho}$) and $L > 0$, we conclude that $\frac{dv}{dx} < 0$, and mass conservation therefore implies that $\frac{d\rho}{dx} > 0$. The Rankine-Hugoniot relations (for mass and momentum) are therefore now:

$$\rho_3 v_3 = \rho_2 v_2 = \rho_1 v_1 \tag{1.17a}$$

$$\rho_3 v_3^2 + p_3 = \rho_2 v_2^2 + p_2 = \rho_1 v_1^2 + p_1 \tag{1.17b}$$

The main result is that a drop in temperature must be accompanied by a proportional rise in density to maintain the pressure to satisfy the jump conditions. This is the main difference between a non-radiative shock and a radiative shock: a non-radiative shock can only increase the density by a factor of ~ 4, but a radiative shock can increase the density by a very large factor.

1.3.1 Particle Acceleration

SNRs shocks are also considered one of the principal accelerators of Cosmic Rays (CR) in the Galaxy. CRs are charged particles (primarily protons, α particles and heavier nuclei (Gaisser 1990)) detected at the Earth and/or in the space around the Earth. The CR spectrum can be described as power-law with a bend at ~ 30 GeV (attributed to the screening effect of the Sun's magnetic field (Blasi 2013)) and a steepening (usually referred to as the *knee*) at 5×10^{15} eV. Particles with energy beyond the ankle, usually referred to as Ultrahigh-Energy Cosmic Rays (UHECRs), are thought not to be of Galactic origin. The reason is that their Larmor radius in the typical galactic magnetic field is of the same order of the Galaxy size or even larger, thus the particle deflection would be small enough to point the source's position in the sky, but the incoming spatial distribution of UHECRs is nearly isotropic; hence, the general opinion is that these particles come from extragalactic sources.

Galactic CRs, i.e. CRs up to the knee energy, are accelerated through a mechanism known as Diffusive Shock Acceleration (DSA; also known as first-order Fermi process, from the seminal idea of Enrico Fermi; see Blandford & Eichler 1987; Bell 1978a,b; Blandford & Ostriker 1978; Fermi 1949). According to this model, the charged particles in the shock region can cross the shock front back and forward, gaining energy every time. In particular, because of the turbulence of the magnetic field, particles from the shocked plasma can reach back the upstream region; once they are in the upstream plasma, they diffuse and can cross the shock again and the process can start again. The DSA mechanism produces a particle spectrum which is a universal power law, in agreement with what we measure on Earth from CR:

$$f(E) \propto E^{-2} \tag{1.18}$$

often expressed in momentum rather than energy, the relation between the two being $f(E)dE = 4\pi f(p)p^2 dp$, implying $f(p) \propto p^{-4}$.

However, SNR shocks remain efficient accelerators only for a relatively short time. As said in Section 1.2.1, immediately after the SN explosion, the SN ejecta expand in the ISM with a velocity that is almost constant and highly supersonic, the acceleration is consequently effective. When the interaction with ISM starts to be relevant, the shock velocity decreases and the acceleration becomes less effective. Moreover, the leptons

are also subject to energy losses due to both Synchrotron and inverse Compton process that can be fast enough to limit the acceleration process. Therefore, the maximum achievable energy in SNRs depends on the balance between the acceleration time and the minimum between the energy loss time and the age of the accelerator.

1.4 The link between SNRs and SNe

SNe are particularly difficult to observe and study. SNe are both relatively rare (only ~ 2 per century in a typical spiral galaxy (Diehl et al. 2006)) and there is little or no visible sign in the outer parts of the progenitor star that an explosion is imminent; thus SNe are unannounced. Another problem is caused by the observational difficulty of having a clear line of sight between the source and the observer. For example, the SN which gave rise to the SNR Cassiopaeia A must have exploded about 350 years ago (Thorstensen et al. 2001) but it was not recorded by astronomers, although its distance is only about 3.4 kpc (Reed et al. 1995); presumably it was obscured by the interstellar dust in the plane of the Galaxy. Moreover, the explosion develops on small scales and in short lapses of time. Because of the great distances SNe can be considered point sources and the spatial resolution of the current instruments does not allow a detailed observational analysis of the early SNe phases. Even if the explosion happened near the observer all the processes related to the CC take place inside the star, where our instruments cannot observe. The calculation of the physics of the collapse is also a complex problem involving many branches of physics such as thermodynamics, magneto-hydrodynamics, general relativity and nuclear physics. Numerical methods are challenging, with high-resolution steps required in both space and time. Additionally, the geometric model within which the calculation takes place may contain complicating factors such as rotation and asymmetry; indeed asphericity is a necessary complication to address some issues. The lack of observational data, for the reasons mentioned above, does not help the development of models. The range of circumstances, the rapidity of the development of the explosions, the poor spatial resolution, the observational shielding of the outer layers of the star, the challenging physics, and the range of significant dimensional scales in the various parts of the star, i.e. from the very small ones involved in the internal accretion shock to the whole size of the star, all make the observational and theoretical solution of the explosion extremely challenging.

In this discomforting scenario, SNRs are an important means to study SNe. In contrast to SNe, the evolution of SNR occurs on a scale of several thousands of years and the remnant expands in the CSM/ISM for several parsecs; SNRs are therefore easily observable astrophysical phenomena. SNRs can reveal details about the inherent asymmetries of the explosion itself (through the study of the spatial and velocity distribution of heavy elements) and the products of nucleosynthesis occurred during the explosion. Clumpiness, filaments, and directional variations of the elemental composition are interpreted as consequences and relics of explosion asymmetries whose origin could be linked to the earliest moments of the explosion. Moreover, SNRs probe the CSM/ISM surrounding the SNe, which are shaped by their progenitors, interacting with it during its evolution. Thus, studying the properties of SNRs, such as inhomogeneities in the morphology and distribution of heavy elements, may allow us to reconstruct the complex phases of the SN explosion going back to the asymmetries that may have occurred during the SN explosion and the interaction with the CSM/ISM modeled by the stellar progenitors during their lifetime, providing an insight where both observation and theoretical analysis fail. For this purpose, studying young SNRs (< 500 yrs) makes it easier to disentangle the effect of the interaction between the ejecta and the CSM/ISM from those related to the processes of SN explosion, although in the Milky Way less than a dozen SNRs are < 1000 years old (Ferrand & Safi-Harb 2012; Green 2014). In such a way, it is possible to link SNe to their remnants, and lead to a better understanding of the physical properties of the SN that otherwise we could not study.

1.4.1 State-of-the-art in the numerical simulation

In this scenario numerical simulations have a main role in bridging the gap between SNe and their remnants. Simulations of both SN explosions and SNR evolution have been conducted in recent years by several groups in 1, 2 and 3 dimensions. Of course, real astrophysical phenomena involve three spatial dimensions and the ultimate aim of first-principle modeling must therefore be 3D simulations. The increasing power of modern supercomputers and the development of highly parallelized numerical codes have made it possible only very recently to perform such 3D simulations with grid-based schemes. Most of the full-scale modeling of supernovae has been performed, and much of it is still performed, with the assumption of rotational symmetry around

a chosen axis (2D). The simplifying assumption of axisymmetry eases the modeling enormously by being computationally much less demanding than 3D simulations. Currently, 3D calculations of SNe are at the extreme limit of numerical feasibility because of their tremendous requirements of computing resources, which strongly increase with more elaborate neutrino treatment. Therefore 2D calculations have so far been the only way to perform high resolution studies with full-scale SN models and to explore larger model sets for the dependence of explosions on micro-physics and progenitor properties. 2D simulations of CC-SNe were conducted by the Oak Ridge (Bruenn et al. 2013), the Garching (Marek & Janka 2009) and Riken (Nakamura et al. 2015) groups and others, each using different transport solvers and approximations but also with different hydrodynamic schemes and computational grids, implying different numerical perturbations that seed the growth of instabilities. Although the different methods used make it difficult to compare all the results, all the groups are in agreement in supporting that 3D simulations are certainly needed to connect models to real observations. Infact, numerical simulations have demonstrated that multidimensionality plays a crucial role to explain why massive stars blow up; effects like hydrodynamical instabilities in collapsing stellar cores like convection and the Standing Accretion Shock Instability (SASI) (see Blondin et al. 2003) trigger asymmetries and nonradial mass motions on large scales and create turbulent flows on small scales. Multidimensional effects are not just a by-product or side-effect of the explosion, they are essential for the success of the mechanism.

In the last few years 3D CC-SNe calculations have been performed with a wide variety of hydrodynamics codes and modeling strategies, using different grids and resolutions, different gravity treatments, different equations of state and different approximations for the neutrino treatment, neutrino opacities, and neutrino reactions (see Couch & O'Connor 2014). There are others that instead of simulating a self-consistent CC, model the post-CC evolution of the SN; they initiate the explosion by injecting thermal and kinetic energy in the internal stellar layers (see Ono et al. 2013); this is a way to bypass all the problems and uncertainties related to the CC and to study the propagation of the shock inside the star from the CC to the shock breakout.

As for the numerical simulations of the evolution of a SNR, a main strategy has been followed in recent years. The method consists in simulating the free-expansion blast profiles, years after the explosion has occurred, using density and velocity profiles

obtained analytically by Truelove & McKee (1999) (see Dewey et al. 2012; Potter et al. 2014).

Recently a first attempt to study the connection between some properties of CC-SN (e.g., the composition and a parameterization of the CSM/ISM) to some observable properties of their SNR has been discussed by Patnaude et al. (2015), even though it is by adopting a 1D approach. Using models for the chemical composition of CC-SN ejecta, they model the dynamics and thermal X-ray emission from shocked ejecta and circumstellar material. Another model for studying the link between light curves and spectra with the properties of CC-SN has been attempted by Utrobin et al. (2015). They perform 3D simulations of neutrino-driven explosions but they assume that the SNR expands homologously, so they do not consider interaction of the ejecta with the CSM/ISM. A more complete model has been recently realized by Orlando et al. (2015, 2016); Ustamujic et al. (2021). Their strategy consists in setting the initial conditions of the simulation to mimic the physical properties of the ejected material after shock passage, following the CC with a 1D Lagrangian code with the scope to model the observations of CC- SNe, such as the bolometric lightcurve and the evolution of the photospheric velocity and temperature (Pumo & Zampieri 2011) and they describe the interaction of the remnant with the wind of the progenitor through 3D hydrodynamic simulations.

Only recently, seminal studies (Patnaude et al. 2015; Utrobin et al. 2015; Orlando et al. 2015, 2016; Wongwathanarat et al. 2017; Orlando et al. 2019; Ferrand et al. 2019; Orlando et al. 2020; Tutone et al. 2020) have described the whole evolution from the SN to the SNR and have shown that HD–MHD models can be very effective in studying the SN–SNR connection. Thus, these studies bring together two distinct physical scenarios (SN and SNR) on the logical and temporal level, creating continuity between the two.

Chapter 2

Non-thermal Emission from SNRs

SNRs are characterized by strong shock waves expanding in the CSM/ISM (see Section 1.3). These shock waves heat the plasma and accelerate particles (see Section 1.3.1) making SNRs bright sources throughout the entire electromagnetic spectrum, from radio to High Energy (HE) (radiation with photon energies of 100 keV to 100 GeV) and Very High Energy (VHE) (radiation with photon energies of 100 GeV to 100 TeV) γ-rays. Observations of synchrotron emission at radio and X-ray of young SNRs reveal the presence of electrons accelerated to energies of several tens of TeV (Vink 2012), suggesting that in the same sources protons could be accelerated beyond $\sim$ 100 TeV through DSA (see Malkov & Drury 2001). However, these observations do not allow to directly deduce the presence of ultra-relativistic protons as well.

High-energy protons, which are the most abundant component of the galactic CRs, do not emit electromagnetic radiation directly as electrons do. These high energy protons can be observed only when they interact with interstellar material through nuclear collisions, producing π^0s that subsequently decay as γ-rays. The presence of "target material", usually molecular clouds in the vicinity of the SNR, is therefore a necessary condition to observe γ-ray from protons.

One of the main difficulties in the analysis of the γ-ray emission is to disentangle the contributions to the emission from different radiation processes. Besides π^0 decay emission from protons, γ-rays can also be produced by ultra-relativistic electrons through Bremsstrahlung process and in interactions of electrons with photons of the 2.7 K Cosmic Microwave Background Radiation (CMB) (but also at infrared and visible

radiation) through the Inverse Compton (IC) scattering process. The latter can dominate over the π^0 decay process, because of its high efficiency at VHE energies, even in the case of small electron/proton ratio of particle acceleration $e/p \ll 10^{-2}$. A possible solution is to look at both low and high energies. At low energies, SNRs could show a peak at 67.5 MeV (half of the π^0 mass), the so called *pion bump*, which is absent in leptonic processes. At higher energies, instead, the leptonic emission drops significantly due to severe energy losses and to the Klein-Nishina suppression of the IC cross section. Also, thermal processes, i.e. process due to the heated plasma by the shock waves, can help for disentangling all these contributions. For example the thermal X-ray emission is important for determining the local plasma density, which in turn constraints the γ-ray non-thermal bremsstrahlung and pion-decay contributions.

A crucial role to understand the γ-ray emission is played by the synchrotron emission. The radio to X-ray synchrotron emission can be used to determine the local magnetic field. Some important properties of the accelerated electrons can be also derived from the study of the synchrotron emission: for example, the power-law index of the electrons distribution is derived from the radio data, while the information about the maximum attainable energy is contained in the X-ray part of the spectrum. The combination of magnetic field and synchrotron flux can then be used to infer the inverse Compton contribution to the γ-ray emission.

The study of γ-ray radiation in SNRs is fundamental to understand important properties of shock waves and, consequently, DSA. For this reason, SNRs have been therefore observed for many years at both HE and VHE. In the MeV–GeV band both Astroriv-elatore Gamma ad Immagini LEggero (AGILE) (Tavani et al. 2009) and Fermi-Large Area Telescope (LAT) (Atwood et al. 2009) have detected strong γ-ray emission from mid-aged SNRs interacting with molecular clouds, such as IC443 (Ackermann et al. 2013), W44 (Ackermann et al. 2013), W51C (Jogler & Funk 2016) (these three presenting the *pion bump*), Cygnus Loop (Katagiri et al. 2011) and W28 (Hanabata et al. 2014) (see also Acero et al. 2016 for a catalog of GeV-emitting SNRs). At VHE 24 distinct sources are classified as SNRs in the TeVcat[1] catalogue by the current generation of ground-based instruments imaging atmospheric Cherenkov telescopes (IACT): High Energy Stereoscopic System (H.E.S.S.) (Aharonian et al. 2006), Major Atmospheric Gamma-ray Imaging Cherenkov Telescopes (MAGIC) (Aleksić et al. 2012) and

[1] http://tevcat2.uchicago.edu/

Very Energetic Radiation Imaging Telescope Array System (VERITAS) (Weekes et al. 2002). Future generations of instruments such as Astrofisica con Specchi a Tecnologia Replicante Italiana (ASTRI) (Scuderi 2019) and Cherenkov Telescope Array (CTA) (Cherenkov Telescope Array Consortium et al. 2019) will provide new insight in the VHE portion of the electromagnetic spectrum. They are both expected to detect cosmic ray accelerating SNRs throughout the whole volume of the Galaxy, detecting both new remnants and adding information of the particle population responsible for the γ-ray emission in bright young SNRs.

2.1 γ-ray Observations of SNRs

It is believed that SNRs are able to produce CR below the so-called "knee" around 1 PeV. While observations of synchrotron emission at radio and X-ray energies indicate the presence of ultra-relativistic electrons (up to 100 TeV) for several SNRs, the acceleration of relativistic protons (the primary component of the galactic CRs) is harder to observe, for the reasons discussed previously, and we do not have yet a robust evidence of accelerated hadrons in SNRs. Moreover, the evolution of a SNR could affect the acceleration mechanism. For example, the spectrum of accelerated particles is expected to vary along different evolutionary stages of the remnant, probing a decreasing acceleration efficiency with a slowing shock and a decreased ability to keep accelerated particles in the shock region due to a dropping magnetic field (Caprioli 2012). In addition, these particles could in principle be subjected to an energy-dependent diffusion, escaping away from the remnant, or could be reaccelerated, rather than freshly accelerated at the SNR shock (Uchiyama et al. 2010; Cardillo et al. 2016; Tutone et al. 2021). In Figure 2.1 I show energy spectra for some typical SNR.

2.1.1 Middle-aged SNRs

From Figure 2.1 it is possible to see that middle-aged remnants show strong γ-ray emission in GeV band; these older remnants are located close to molecular clouds and also present the *pion bump* feature indicating a possible hadronic emission. It is possible that these remnants accelerated hadrons in the first part of their life, and when the shock speed dropped below 1000 km s^{-1} and the magnetic field weakened the more energetic

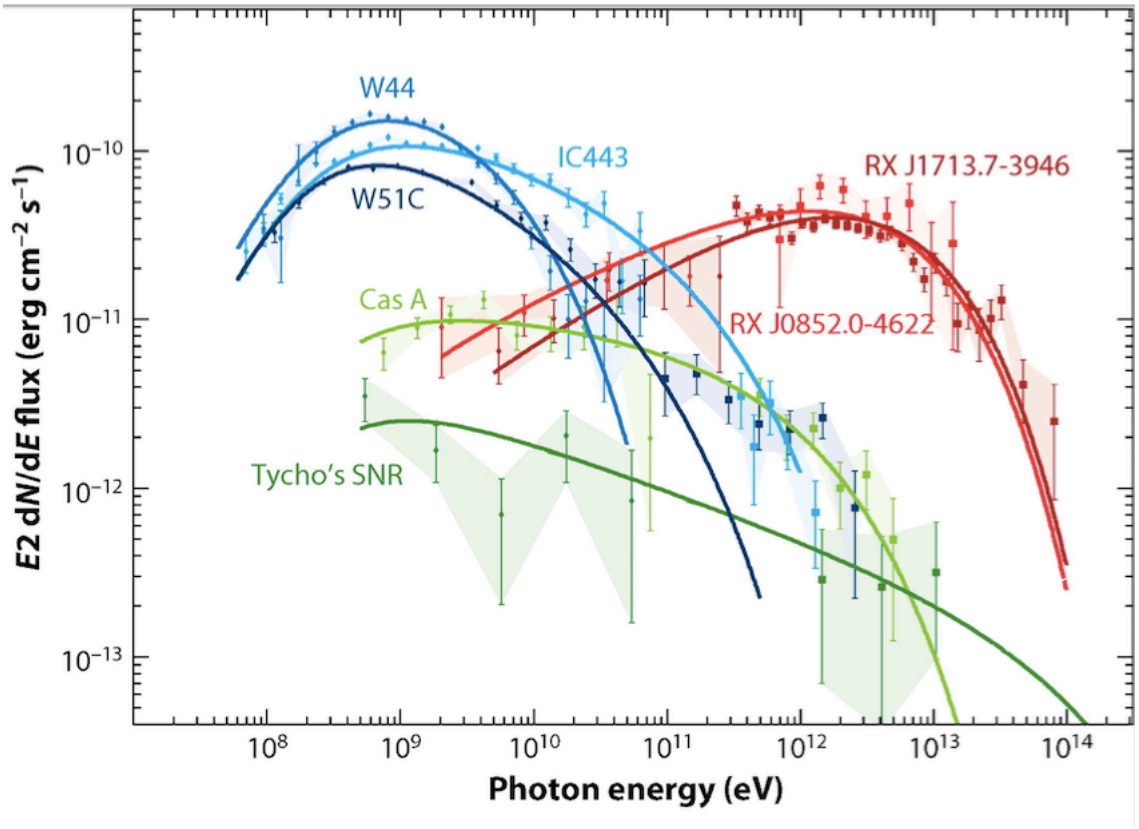

Figure 2.1: γ-ray energy spectra for several of the most prominent SNRs. Young SNRs ($< 10^3$ years) are shown in green. Shell-type SNRs of ages $\sim 2 \times 10^3$ years are shown in shades of red. The middle-aged SNRs ($\sim 2 \times 10^4$ years) are shown in blue. Also shown are hadronic fits to the data (solid lines). Figure from Funk 2015.

particles ran away and interacted with the dense material around the remnant. In this case, γ-ray should be both detected in the inner region of the remnant (where the low energy particles are still confined) and in the surrounding clouds, as for the case of W44 (Uchiyama et al. 2012; Giuliani et al. 2011). However, an alternative scenario assumes that the ambient Galactic CRs have been reaccelerated inside the shock-compressed cloud and that they are not freshly accelerated through the DSA mechanism (Uchiyama et al. 2010; Cardillo et al. 2016; Tang 2019; Tutone et al. 2021). Because of the low spatial resolution of MeV-GeV telescopes is hard to separate the γ-ray components contribution produced in the shell and in nearby clouds which would provide an important insight into the understanding of CR acceleration and escape from SNRs. Among the prominent GeV-emitting middle-aged SNRs interacting with molecular clouds, IC 443 is a rare case that is bright enough at TeV energies to be detectable. This is because in middle-aged SNRs the highest energy CRs could have already left the SNR region, leading to steep energy spectra, that are less bright at TeV energies.

2.1.2 Young SNRs

From Figure 2.1 emerges that the dominant populations of SNRs at TeV energies are young objects. Two sources, similar to each other, are the shell-type SNRs RXJ1713.7-3946 and RXJ0852.0-4622, which are characterized by hard spectra in the GeV band and, consequently, a larger flux in the TeV band together with a cut-off beyond 10 TeV. RX J1713.7-3946 represents an atypical SNR. This remnant shows weak radio emission and no thermal X-ray radiation at all, but is a powerful nonthermal X-ray and TeV γ-ray emitter, with a spatial correlation between the latter (Sano et al. 2010). Its broad-band γ-ray spectrum, observed by *Fermi* LAT (Abdo et al. 2011) and H.E.S.S. (Aharonian et al. 2007), has an unclear origin. The very low level of thermal X-ray emission (which should track the target material for hadronic interactions; see Katsuda et al. 2015) suggest leptonic emission in this object. However, it is possible that accelerated protons could interact with dense gas condensations (Zirakashvili & Aharonian 2010) embedded in the low-density shell. This scenario would favour harder protons spectra since only the highest energy CRs can penetrate into the centre of this clumpy environment, therefore a hadronic scenario cannot be ruled out completely. The leptonic model itself presents some problems, at least within a simple one-zone model. To explain both the

X-ray and γ-ray emission the leptonic model require a magnetic field between 10 μG and 15 μG in contrast to the large magnetic field required to explain the fast variability of X-ray emission on small scales (Tanaka et al. 2008). A possible solution could come from morphological studies. While inverse Compton models predict a broad γ-ray spatial distribution (due to the need of low magnetic field, which allows the multi-TeV electrons to propagate to large distances), the hadronic model predicts narrower and sharper spatial distribution, mainly due to the enhanced emission in the compressed region of the shock. Unfortunately, present γ-ray telescopes have too limited angular resolution to distinguish the distribution predicted by the two models. In the future, the CTA telescope would provide a great improvement, especially at multi-TeV energies, and would contribute to the understanding of possible multi-zone models in SNRs.

Very young SNRs also emit γ-ray radiation, both at high and very high energies. Tycho, one of the youngest and best studied SNRs, has been observed by *Fermi* (Giordano et al. 2012) and VERITAS (Archambault et al. 2017). Because of the large statistical uncertainties of both data sets the spectral shape of the γ-ray emission is not constrained, but its γ-ray spectrum is $\propto E^{-2.2}$ and multi-wavelength studies clearly point towards a hadronic origin of this emission (Morlino & Caprioli 2012; Völk et al. 2008). The flat γ-ray spectrum up to 10 TeV implies that the parent protons population could continue without a steepening or a cutoff to at least several hundred TeV. By extending the observed γ-ray spectrum, with ASTRI and CTA, it would be possible to exclude the IC origin of radiation and claim the source as a strong hadronic accelerator.

Strong hadron accelerators, i.e. sources able to accelerate protons up to $\sim 10^{15}$ eV, are usually known as PeVatrons. Since, as said in Section 2, the leptonic emission is disfavoured at higher energies by the Klein-Nishina suppression of the Compton cross-section, a detection of γ-ray photons with energies above 100 TeV is expected to indicate that their source is accelerating hadronic CRs at PeV energies. SNRs are believed to be the best candidates for PeVatron as DSA theory predicts that SNRs are capable of accelerating particles up to PeV energies. Unfortunately, no PeVatrons have been detected among the known SNRs, not only because of the low sensitivity of current Cherenkov Telescopes above few tens of TeV but also because such sources are predicted to be rare (Cardillo et al. 2015; Cristofari et al. 2020).

2.2 Contents and Aims of the Thesis

In this thesis, I aim at investigating the physical properties of SNRs, using the results from the simulation of a SNR evolution and by analyzing γ-ray data collected by the Fermi-LAT. Numerical simulations are powerful tools to get a deeper level of understanding of the dynamical events that occur during the evolution of a SNR, being a benchmark to study the correlation between the characteristics of the progenitor star, the physics of the explosion and physical and chemical properties of the evolved SNR. The γ-ray band in SNRs is crucial to study the mechanism, not fully understood yet, of particles acceleration both in the GeV energy domain for the search of 'smoking guns' of former PeVatrons, re-acceleration and diffusion of CR and both well beyond 10 TeV, where the major future ground-based γ-ray detectors (ASTRI and CTA) will remove, to a large extent, many current uncertainties and ambiguities concerning the origin of γ-rays from SNRs. To this end in Chapter 4 (see also Tutone et al. 2020) I show how matter mixing occurs at later times during the remnant expansion and interaction with the CSM, and how large-scale anisotropies typically observed in CC–SNe affect the internal structure of the gas using a 3D MHD model describing the evolution of the remnant from the onset of the SN to the development of its remnant at the age of 5000 years. In Chapter 5 (see also Tutone et al. 2021) I present the analysis of the γ-ray emission from the SNR Cygnus Loop region's. I aim at studying the origin of the multiwavelength non-thermal emission from this remnant, at clarifying the acceleration mechanism taking place in the shocks regions of the remnant. In Chapter 6 I briefly introduce the Astrofisica con Specchi a Tecnologia Replicante Italiana (ASTRI) Mini Array and I present two scientific cases that the ASTRI Mini-Array will be able to address in a long-term planning of observations of the Northern Galactic sky.

Chapter 3

γ-ray Instrumentation

The γ-ray band of the electromagnetic spectrum has no clear upper limit. This characteristic of the spectrum caused a gradual evolution of the instruments and facilities aimed at investigating the physics of HE, and upwards, phenomena. The first instruments to be used for this purpose were space-borne detectors. This is because the atmosphere of the Earth is opaque to high energy photons beyond the optical waveband, therefore their direct registration requires instruments in space. This type of instruments continue to operate nowadays up to hundreds of GeV and few TeV, such as the *Fermi* satellite (Atwood et al. 2009) and the Italian AGILE satellite. The angular resolution of these instruments below 1 GeV is quite modest (larger than 1 $^{\circ}$), but it becomes significantly better at higher energies, approaching 0.1 $^{\circ}$ above 10 GeV. However, for fluxes above 100 GeV the detection rate for a γ-ray telescope becomes very low (100 photons m^{-2} year^{-1} for the Crab Nebula) causing a limitation in the collection area for such instruments so that the space telescopes cannot provide adequate statistics for comprehensive spectral and temporal studies in the VHE domain. It is impossible for space instruments to overcome this limitation without resorting to instruments of size and weight unpractical for space mission. But a need for investigating higher energies started to rise already around the end of the 80's (Weekes et al. 1989). To study phenomena beyond 100 GeV two types of facilities are used to extract information on the incoming γ radiation or CRs. A γ-ray , above some GeV, entering the atmosphere generates an electromagnetic cascade that can be detected: either by detecting the Cherenkov radiation of charged particles in air (Cherenkov technique), or by directly detecting the

charged particles reaching the ground, the Extended Air Shower (EAS) experiments. Most secondary charged particles have a speed larger than light in air and emit therefore Cherenkov radiation, which can be detected by special telescopes. The effective detection area is comparable to that of the light pool on the ground, i.e. a few 10^4 m^2. Generally, EAS facilities, such ad the Pierre Auger Observatory (The Pierre Auger Collaboration 2015), the HAWC array (Abeysekara et al. 2013), MILAGRO[1] and Tibet AS-γ-ray [2] consist of arrays of fixed detectors on the ground. They measure directly the secondary particles produced by air showers (Longair 2011): mainly muons, electrons or even neutrinos for some type of underground facilities. These facilities consists of a huge collection areas of the order of $\sim$ 1 km^2 allowing to collect enough particles over 100 TeV, and they are relevant mostly to study UHECRs. In this thesis I will not deal with EAS type, but with facilities that operate between tens of GeV to tens of TeV exploiting the Cherenkov light produced by EASs, i.e. the air Cherenkov experiments.

In Chapter 5 I present the analysis performed on data collected by the *Fermi* satellite and in Chapter 6 I present two scientific cases of potential interest for a future Cherenkov telescope: the ASTRI Mini-Array. Details on these instruments and other current Cherenkov telescopes will be given in the following two sections.

3.1 The *Fermi* instrument

Fermi was launched by NASA on the 11th June 2008 on a Delta II Heavy launch vehicle. Its circular orbit has an inclination of $25.6°$ and was set at an initial altitude of 565 km (which now is $\sim$ 20 km lower). The *Fermi* mission has the main purpose of observing the γ-ray sky and the LAT is designed to address a number of scientific objectives including: resolving the origin of unidentified sources and of the diffuse emission, understanding CRs propagation mechanism and investigating the behavior of transient phenomena. *Fermi* is composed of two main instruments, which are presented in more detail in the following.

[1] http://physics.nyu.edu/experimentalparticle/milagro.html
[2] http://www.icrr.u-tokyo.ac.jp/em

3.1.1 The Large Area Telescope

The Large Area Telescope (LAT) is a particle detector optimized for the detection of photons in the energy range between $\sim$ 100 MeV and $\sim$ 300 GeV, but actually detecting γ-ray up to a few TeV. It has a large field of view, over 2 steradians, and it is able to measure the locations of bright sources to within 1 arcminute It is composed of three different types of detectors: a tracker-converter for the reconstruction of arrival directions; an electromagnetic hodoscopic calorimeter for energy evaluation; an anticoincidence detector to discriminate between charged and neutral incoming primary particles.

3.1.2 The Gamma-Ray Burst Monitor

The Gamma-Ray Burst Monitor (GBM) is specifically designed to study gamma ray bursts, energetic explosions that can last from ten milliseconds to several hours coming from random directions. It is composed of 12 sodium iodide and 2 detectors made of bismuth germanate that cover an energy range from about 10 keV up to several tens of MeV. The detectors are positioned on the spacecraft and oriented as to provide approximately uniform coverage of the unocculted sky. When a burst occurs, the GBM can compute its localization on board allowing the autonomous repointing of the *Fermi* observatory to place the burst within the LAT field of view.

3.2 Cherenkov Telescopes

Instruments designed to detect the Cherenkov light are generally referred to as imaging atmospheric Cherenkov telescopes (IACT). The Cherenkov light, produced during the development of the electromagnetic cascades in the atmosphere, lasts only several nanoseconds, but it is sufficient for detection using large optical reflectors equipped with fast optical receivers and arrives at ground level in a region with a radius of $\sim$ 100 m. Creating an array of Cherenkov detectors located at distances of about 100 m from each other allows the stereoscopic observations of air showers and provides effective rejection of the background, as well as good angular resolution (better than 0.1 °) and energy resolution (better than 15%). A new generation of ground-based γ-ray detectors will widen our knowledge in the VHE field, increasing the number of known γ-ray sources

and taking advantage of the pioneered work of their predecessors (H.E.S.S., MAGIC and VERITAS). Among the future instruments, the Cherenkov Telescope Array (CTA) (Cherenkov Telescope Array Consortium et al. 2019) is the largest, with more than 100 telescopes operating in two different site (Southern site placed in the Atacama desert at Paranal, Chile, Northern site placed in Roque de los Muchachos, La Palma, Canary Islands), and more advanced, covering γ-ray energies from 20 GeV to 300 TeV with the highest sensitivity among IACT. To reach such performances, CTA will be composed of three classes of telescope types that will differ for size, structure and sensibility: the Large-Sized Telescope (LST), Medium-Sized Telescope (MST) and Small-Sized Telescope (SST). The size of the telescopes reflect an energy range: at low energies the Cherenkov yield is lower, therefore it is necessary a larger size of the telescope reflector; at high energies, gamma-ray fluxes are lower, so it requires covering a larger ground area with as many telescopes of smaller size as possible.

In the context of CTA, the Italian National Institute for Astrophysics (INAF), together with international partners from South Africa and Brazil, has led the construction of one class of the SST: the Astrofisica con Specchi a Tecnologia Replicante Italiana (ASTRI) telescope (Scuderi 2019). A prototype is currently taking data at the INAF "M.C. Fracastoro" observing station in Serra La Nave (Mount Etna, Sicily). The ASTRI SST-2M prototype was inaugurated during the CTA Consortium Meeting in September 2014 and detected the first detection of VHE γ-ray emission from the Crab Nebula in 2018 (Lombardi et al. 2020). The ASTRI telescopes have a dual mirrors optical configuration based on a modified Schwarzschild - Couder design (Vassiliev et al. 2007) and a compact Cherenkov camera based on Silicon Photo-Multipliers (SiPM) detectors and an innovative readout electronics (Sottile et al. 2016; Catalano et al. 2018).

3.2.1 The ASTRI Mini-Array

An array of nine SST ASTRI-like telescopes, the ASTRI Mini-Array, implemented on the base of the prototype's camera and structural design, will be financed by INAF and built at the Observatorio del Teide[3], located in the Canary island of Tenerife at 2390 m of altitude. The area where the telescopes will be installed will cover a rectangular strip of approximately 650 meters in length and 270 meters in width (see Figure 3.1).

[3] https://www.iac.es/en/observatorios-de-canarias/teide-observatory

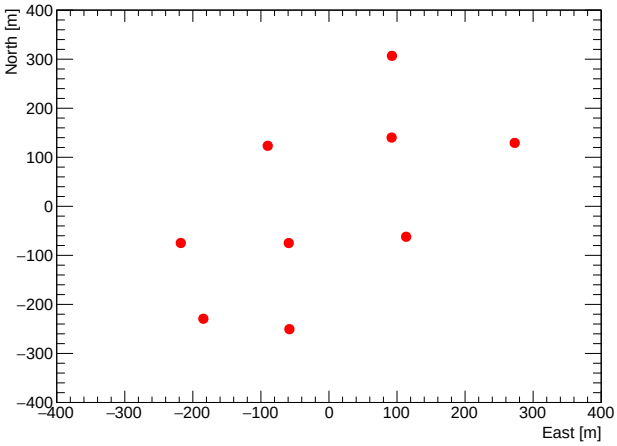

Figure 3.1: Layout of the ASTRI Mini-Array. The figure shows the final positions of the 9 ASTRI telescopes (red circles).

After the calibration phase and the validation of the expected performances, in the first four years, the array will be run as an experiment.

Here, I summarise the most important characteristics of the Instrument Response Function (IRF) (optimised for a 50 hours exposure and obtained from dedicated Monte Carlo (MC) simulations and MC reconstruction analysis Lombardi et al. 2021) regarding energy and spatial resolution and sensitivity. For an on-axis source, in the 1–200 TeV band, the energy resolution is in the range 12-15%; the angular resolution is $\sim 8'$ at 1 TeV, with a minimum value of $\sim 3'$ at 10 TeV, degrading very little up to 100 TeV. The differential sensitivity curve for 50 hours has its minimum value of 7×10^{-13} erg cm^{-2} s^{-1} between 5 and 8 TeV (see Figure 3.2). The dependence of these performances on the offset angle is contained within a 10–20 % degradation from the best nominal values up to 3.5°; the degradation reaches 40–50 % for an offset angle of $\geq$ 4.5°. Figure 3.3 shows the ASTRI Mini-Array differential sensitivity compared with those of current VHE imaging atmospheric Cherenkov telescope arrays for a 50 hours integration time. This, together with the improved angular and energy resolution, will allow the ASTRI Mini-Array to provide a significant step forward in the study of the VHE sky.

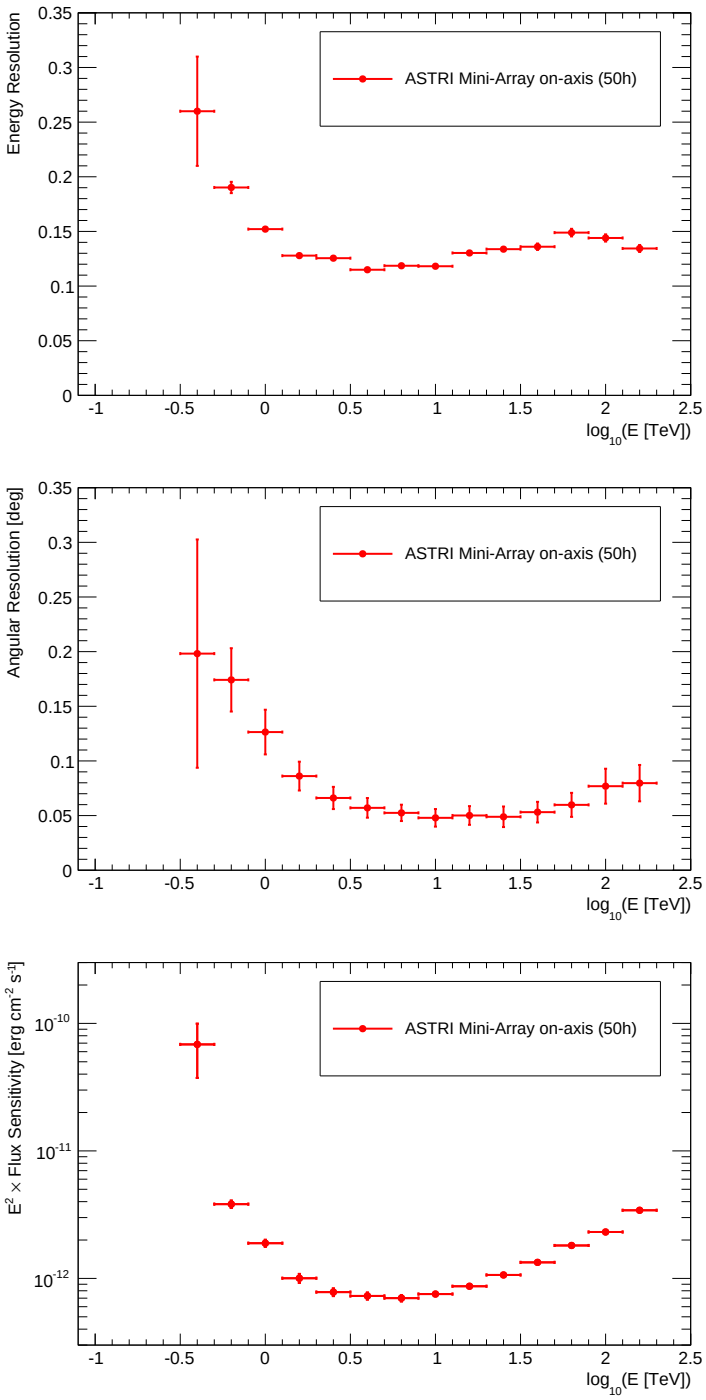

Figure 3.2: On-axis energy resolution (top), angular resolution (middle) and differential sensitivity (bottom) of the ASTRI Mini-Array for 50 hours of observations as a function of the energy between $\simeq$ 0.3 TeV and $\simeq$ 200 TeV (Lombardi et al. 2021).

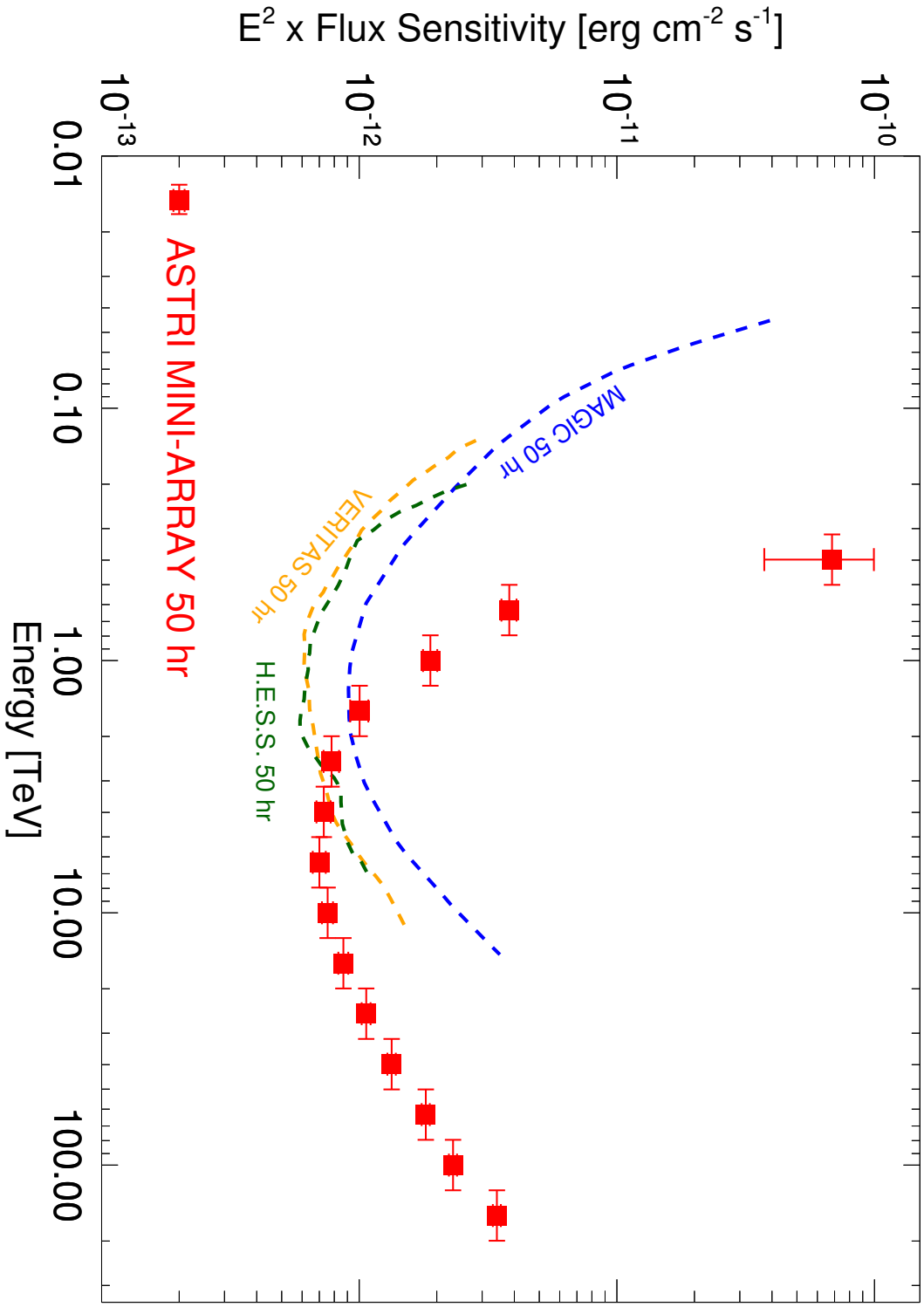

Figure 3.3: ASTRI Mini-Array differential sensitivity (Lombardi et al. 2021) compared with those of current imaging atmospheric Cherenkov telescope arrays. The differential sensitivity curves come from Aleksić et al. 2016 (MAGIC), the VERITAS official website (https://veritas.sao.arizona.edu) and Holler et al. 2015 (H.E.S.S.).

3.2.2 The MAGIC telescopes

As one of the three currently operating IACT facilities (the others being H.E.S.S. and VERITAS), the Major Atmospheric Gamma-ray Imaging Cherenkov Telescopes (MAGIC) collaboration operates two air-Cherenkov telescopes working in stereo mode from 2009 and further upgraded in 2012 (Aleksić et al. 2016; Aleksić et al. 2016). The observation site is located on the island of La Palma (Canary Islands, Spain) at an altitude of about 2200 m above sea level. MAGIC can investigate γ-ray from few tens of GeV to tens of TeV (Aleksić et al. 2015). Both telescopes have a diameter of ~ 17 m covered by 964 square all-aluminum mirrors with a side of ~ 0.5 m, resulting in a reflective area of 236 m^2. They have a 1039-pixel camera each, allowing them to detect Cherenkov light from EAS within a field of view of 3.5° .

3.2.3 The VERITAS telescopes

Very Energetic Radiation Imaging Telescope Array System (VERITAS) is a major ground-based γ-ray observatory with an array of four 12 meter air-Cherenkov telescopes located at the Fred Lawrence Whipple Observatory, in southern Arizona, United States, at an altitude 1268 m since January 2007.Each telescope use 350 identical hexagonal spherical mirrors (of area 0.322 m^2 and radius-of-curvature of approximately 24 m) giving a total reflector area of 110 m^2. VERITAS can investigate γ-ray from 85 GeV to ¿30 TeV, with an angular resolution of 0.08° at 1 TeV.

3.2.4 The HESS telescopes

High Energy Stereoscopic System (H.E.S.S.) is a system of IACT of five telescopes, four with a mirror just under 12 m in diameter, arranged 120 m apart from each other in a square, and one larger telescope with a 28 m mirror, constructed in the centre of the array, located in Göllschau, Namibia, near the Gamsberg. The first telescope went into operation in 2002, while the current configuration saw its first light on 26 July 2012. The full H.E.S.S. detector is sensitive to VHEγ-ray in the range from ~ 30 GeV to ~ 100 TeV.

Chapter 4

3D modeling from the onset of the SN to the full-fledged SNR

In this chapter, I report on the study of the matter-mixing process between different chemical layers, by investigating the dynamical and chemical evolution in a young SNR. I performed a series of simulations devoted to studying the effect of a large-scale anisotropy on remnant properties during the first 5000 years of evolution and I identified an observable signature of such anisotropy. These simulations provide a novel tool to investigate SNRs with similar properties.

4.1 Introduction

Core-Collapse (CC) Supernova (SN) play a major role in the dynamical and chemical evolution of galaxies (by injecting mass and energy) and in driving the chemical enrichment of the diffuse gas. Nevertheless, many aspects of the processes governing the SN engine and the final stages in the evolution of their progenitor stars are not fully understood. Severe limitations in these studies are the rarity of SN events in our galaxy (on average about one every 50 years; Diehl et al. 2006), the large distances of extragalactic SNe which make them unresolved point-like sources, and their unpredictability and transient nature.

Otherwise, nearby SNR, are extended sources for which the structure and chemical composition of the stellar debris ejected in the SN outburst (i.e., the ejecta) can be

studied in detail. Moreover, SNRs probe the Circumstellar Medium (CSM) surrounding the SNe, which can be shaped by the progenitor stars through their powerful stellar winds. However, with increasing age, all these pieces of information, which are useful for establishing a SN–SNR connection, are diluted by the increasing interaction of the remnant with the surrounding environment.

Hydrodynamics (HD) and Magneto Hydrodynamics (MHD) models can be powerful tools to bridge the gap between CC–SNe and their remnants. However, up until recent years, the key strategy was to describe either the SN evolution or the expansion of the remnant due to the very different time and space scales involved in these two phases of evolution and the inherent three-dimensional (3D) nature of the phenomenon. As a result, SN models described the early SN evolution, leaving out an accurate description of their subsequent interaction with the ambient environment; SNRs models described only the expansion of the remnant and its interaction with the ambient medium, leaving out a self-consistent and accurate description of the distribution of mass and energy of the ejecta soon after the SN explosion.

To date, the mixing of chemically homogeneous layers of ejecta after the SN event has been investigated in detail only in the aftermath of SN explosions (e.g., Kifonidis et al. 2006; Joggerst et al. 2009, 2010), not considering the transition from the phase of SN to that of SNR. Very recently, Ono et al. (2020) studied the matter mixing in aspherical CC-SNe through accurate 3D simulations, aiming to link the ejecta structure soon after the shock breakout at the stellar surface (i.e., when the shock produced by the explosion leaves the stellar surface) with the nature of the progenitor star.

Here, I aim to analyze how matter mixing occurs at later times during the remnant expansion and interaction with the CSM to investigate how the various chemically homogeneous layers at the time of the explosion map into the resulting abundance pattern of the SNR, and how large-scale anisotropies typically observed in CC–SNe (possibly originated by instabilities developed during the CC; e.g., Nagataki et al. 1997, 1998; Nagataki 2000; Kifonidis et al. 2006; Takiwaki et al. 2009; Gawryszczak et al. 2010; Wongwathanarat et al. 2017; Bear & Soker 2018) affect the evolution of these layers. To this end, I developed a 3D MHD model describing the evolution of the remnant from the onset of the SN to the development of its remnant at the age of 5000 years, assuming a Red Supergiant (RSG) as a progenitor. I analyzed the effects of large-scale anisotropies that may develop soon after the SN on the final remnant morphology. These

anisotropies may be responsible for the knotty and clumpy ejecta structure observed at different wavelengths in many CC SNRs (e.g., the Vela SNR, Aschenbach et al. 1995; Miceli et al. 2008; García et al. 2017; G292.0+1.8, Park et al. 2004; Puppis A, Katsuda et al. 2008a; and Cassiopeia A, Fesen et al. 2006; Milisavljevic & Fesen 2013; N132D, Law et al. 2020) which is commonly interpreted as a product of HD instabilities developed during the complex phases of the SN explosion (Gawryszczak et al. 2010). However, the role of these anisotropies in the evolution of the chemical stratification of the remnant is still unclear.

The chapter is organized as follows: in Sect. 4.2 I describe the MHD model, in Sect. 4.3 I discuss the results of the simulations, and in Sect. 4.4 I draw the conclusions.

4.2 The numerical setup

The model describes the evolution of a SNR from soon after the CC of the progenitor star to the full-fledged remnant at the age of 5000 years, following the expansion of the remnant through its pre-SN environment. As in Orlando et al. (2016), the initial distribution of ejecta is derived from a spherical symmetry 1D SN model which describes the SN evolution from the CC to the shock breakout at the stellar surface, covering about 24 hours of evolution. The output of the SN simulation provided the initial radial profile of the ejecta distribution, including their chemical composition. Consequently, I include a self-consistent description of the initial physical property profiles of the ejecta. I then mapped this output into the 3D domain and started the 3D SNR simulations.

4.2.1 The initial conditions

As initial conditions for the 3D SNR simulations I adopted one of the SN simulations presented in Ono et al. (2020). These authors performed both 1D and 3D HD simulations of SN explosions, with the aim of investigating the matter mixing during the expansion of the blast wave through the stellar interior. Their 1D simulations assume spherical symmetry, whereas the 3D simulations consider aspherical explosions triggered by an initial asymmetric injection of kinetic and thermal energy around the composition interface of the iron core and silicon-rich layer. The simulations were initialized by considering different pre-SN stellar models, including progenitor blue and

red supergiants, and were performed with the adaptive-mesh refinement HD–MHD code FLASH (Fryxell et al. 2000).

The SN model takes into account the effects of gravity (both self-gravity and gravitational effects of the central proto-neutron star), the fallback of material onto the central compact object, the explosive nucleosynthesis through a nuclear reaction network including 19 species (n, p, ^{1}H, ^{3}He, ^{4}He, ^{12}C, ^{14}N, ^{16}O, ^{20}Ne, ^{24}Mg, ^{28}Si, ^{32}S, ^{36}Ar, ^{40}Ca, ^{44}Ti, ^{48}Cr, ^{52}Fe, ^{54}Fe and ^{56}Ni), the feedback of nuclear energy generation, and the energy deposition due to radioactive decays of isotopes synthesized in the explosion (see Ono et al. 2020 for more details). For my purposes, I considered the case of a 1D SN simulation from a non-rotating, solar-metallicity progenitor RSG with a main-sequence mass of 19.8 $M_{\odot}$ which reduces to 15.9 $M_{\odot}$ at collapse (Sukhbold et al. 2016), and with an injected energy in the explosion of 2.5×10^{51} erg (see Sect. 3.1 in Ono et al. 2020).

The aim of the SNR simulations is not a detailed description of the effects of matter mixing before the shock breakout (indeed carefully modeled and analyzed through the 3D SN simulations by Ono et al. 2020). The aim of this work is to highlight the contribution to matter mixing during the expansion of the blast wave through the CSM and to investigate the stability of the 1D "onion-shell" structure of the progenitor star during the evolution of the SNR. To this end, I explored the case of a spherically symmetric SN explosion and the case of a SN characterized by large-scale anisotropy. In this latter case, once the output of the 1D SN simulation is mapped to the 3D domain, I parametrize the initial large-scale anisotropy of ejecta that may have been developed soon after the SN explosion. The aim is to investigate how the matter mixing and the final remnant morphology depend on the physical (density and velocity) and geometric (position and size) properties of the initial anisotropy. The physical properties of the initial condition, that is, the output from the CC–SN simulation, consist of an initial remnant at $t \sim 6 \times 10^4$ s (≈ 17 hours) after the CC with a radius of $\sim 1.85 \times 10^{15}$ cm, an ejecta mass of 14.4 $M_{\odot}$, and a kinetic energy of 1.35×10^{51} erg. At this epoch, hours after the breakout of the shock at the stellar surface, the ejecta expand almost homologously through the tenuous wind of the progenitor star (e.g., Gawryszczak et al. 2010; Wongwathanarat et al. 2017; Ono et al. 2020). The initial radial density profile of the ejecta presents a less dense inner region surrounded by a denser shell located in the region of radius 6.2×10^{14} cm, corresponding to about 30% of the radius of the ejecta (see Figs. 4.1 and 4.2; see also Ono et al. 2020 for a description of the evolution of the SN

and the formation of the large-scale structure in the density radial profile). This density profile arises from the SN simulation and depends on the progenitor star considered. Here considered a generic case of a RSG; a different progenitor, such as for instance a blue supergiant, could produce a much smoother density profile with structures that may significantly differ from the dense shell discussed above (see e.g., Ono et al. 2020). The velocity profile (see Fig. 4.1) increases linearly with the radius of the ejecta from zero at the origin to a maximum of 5.3×10^8 cm s^{-1} at the external shell of the initial remnant.

4.2.2 Modeling the evolution of the SNR

The numerical setup for the SNR simulations is analogous to that described in Orlando et al. (2019, 2020). As the remnant expansion is described during the free expansion and Sedov expansion phases, the radiative losses (see Orlando et al. 2005, also treated in Miceli et al. 2006; Lee et al. 2015) are neglected. I adopted a 3D Cartesian coordinate system (x, y, z) and I carried out the simulations by numerically solving the full time-dependent ideal MHD equations in conservative form:

$$\frac{\partial \rho}{\partial t} + \nabla \cdot (\rho \vec{v}) = 0, \tag{4.1}$$

$$\frac{\partial \rho \vec{v}}{\partial t} + \nabla \cdot \left[\rho \vec{v}\vec{v} - \vec{B}\vec{B} + \vec{I}P_*\right]^T = 0, \tag{4.2}$$

$$\frac{\partial \rho E}{\partial t} + \nabla \cdot [\vec{v}(\rho E + P_*) - \vec{v} \cdot \vec{B}\vec{B}] = 0, \tag{4.3}$$

$$\frac{\partial B}{\partial t} + \nabla \cdot (\vec{v}\vec{B} - \vec{B}\vec{v}) = 0, \tag{4.4}$$

where

$$P_* = P + \frac{B^2}{2}, \qquad E = \epsilon + \frac{1}{2}v^2 + \frac{1}{2}\frac{B^2}{\rho} \tag{4.5}$$

are the total pressure and the total gas energy (internal energy, ϵ, kinetic energy, and magnetic energy), respectively, $\vec{B}$ is the magnetic field, ρ is the density, $\vec{v}$ is the velocity,

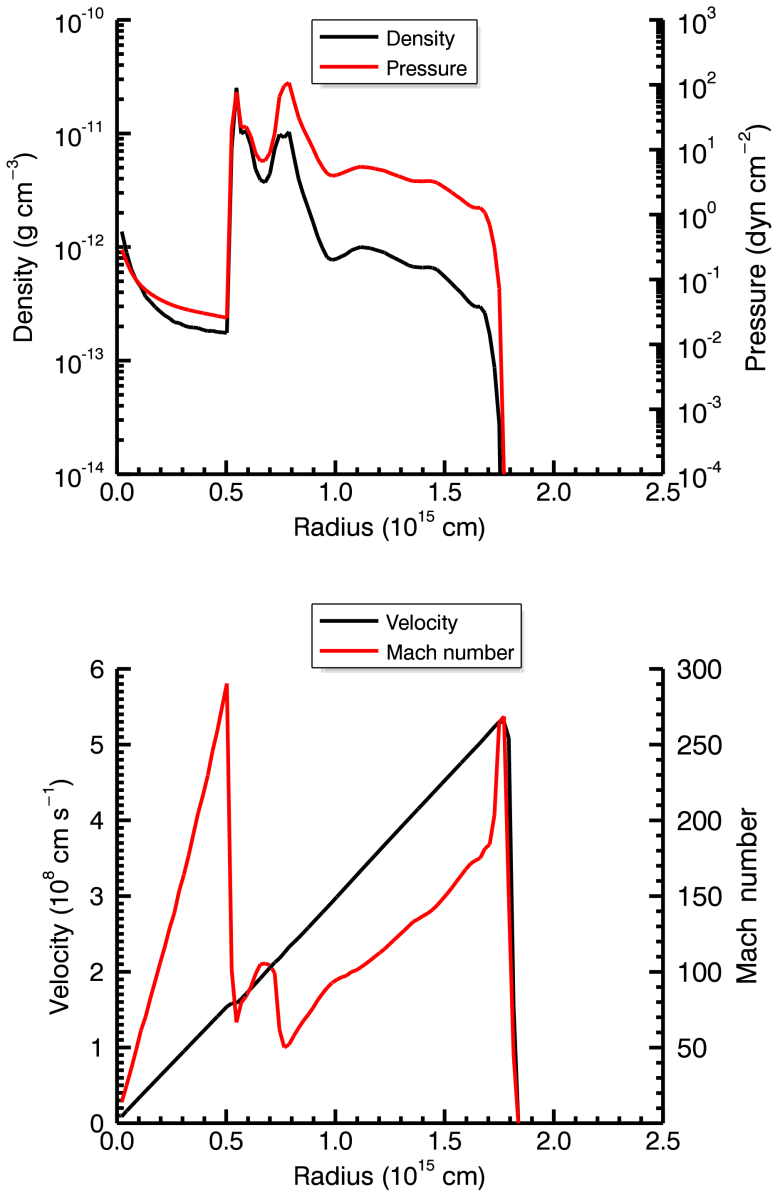

Figure 4.1: Initial conditions for the 3D simulations. *Top panel:* Radial profiles of initial ejecta density (black line) and pressure (red line). *Bottom panel*: Radial profiles of initial ejecta velocity (black line) and Mach number (red line).

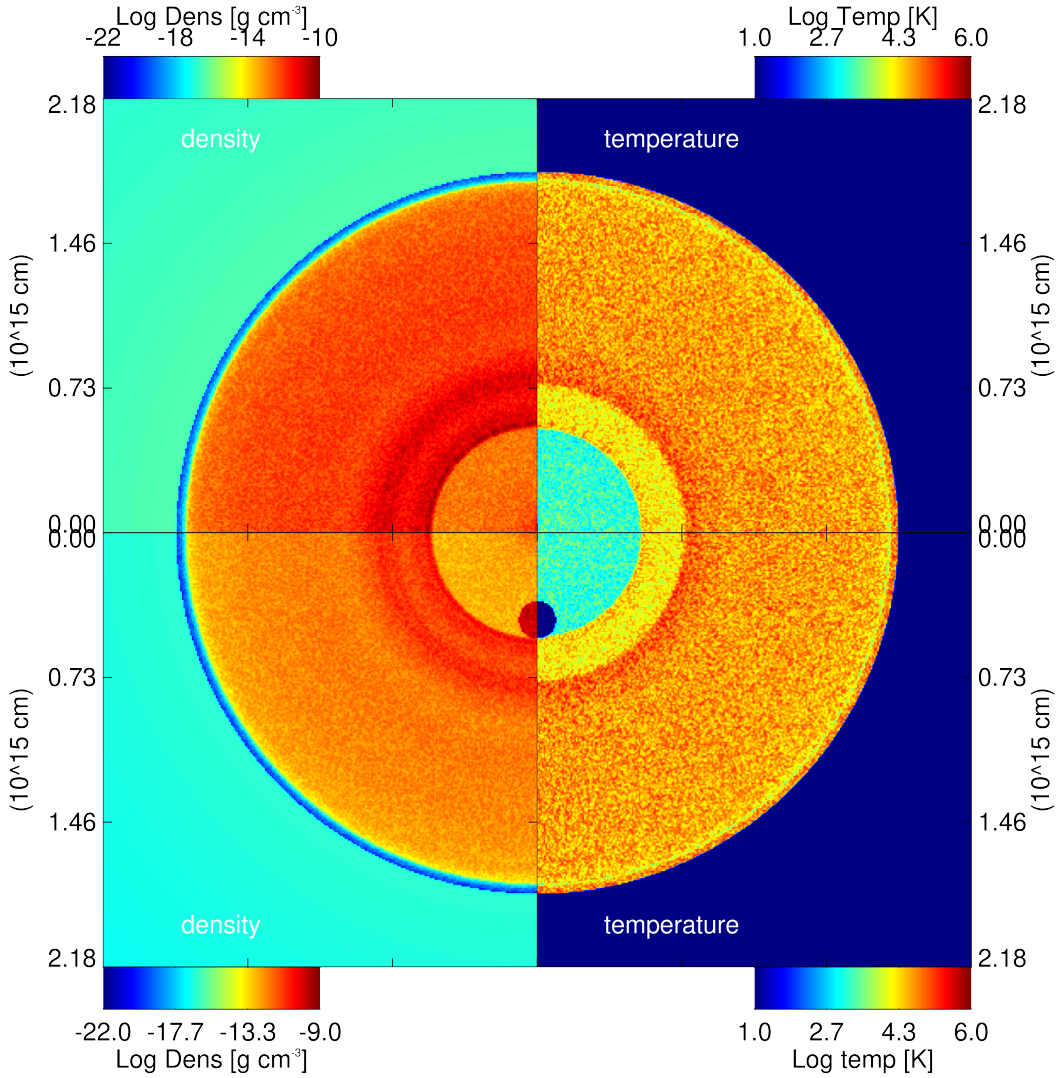

Figure 4.2: Density (left-hand quadrants) and temperature (right-hand quadrants) sections $(x, 0, z)$ showing examples of the initial conditions. The values are color coded according to the scale shown for each quadrant. Upper quadrants show the case of a spherically symmetric explosion, and lower quadrants show a case with a dense, isobaric spherical anisotropy (namely run Si-R5-D750-V5 in Table 4.1).

$\vec{I}$ is the identity matrix, and P is the pressure and t is the time. The set of equations is closed by the equation of state (EOS) for ideal gases, $P = (\gamma - 1)\rho\epsilon$, where $\gamma = 5/3$ is the adiabatic index.

The 3D simulations of the expanding SNR were performed using PLUTO (see Mignone et al. 2007), a numerical code developed for the solution of hyper-sonic flows that has been widely and successfully used in several studies. The MHD equations are solved using the MHD module available in PLUTO, which was configured to compute inter-cell fluxes with the Harten-Lax-van Leer discontinuities (HLLD) approximate Riemann solver, while third order in time is achieved using a Runge-Kutta scheme. To preserve the condition of $\nabla \cdot B = 0$, a mixed hyperbolic and parabolic divergence cleaning technique is used (Mignone et al. 2007).

The distribution of elements is traced through a set of advection equations:

$$\frac{\partial \rho X_{\rm i}}{\partial t} + \nabla \cdot (\rho X_{\rm i} v) = 0, \tag{4.6}$$

which are solved for each of the elements considered in addition to the MHD equations, where $X_{\rm i}$ is the mass fraction of the element of index i, and i runs over the 19 species listed in Section 4.2.1. Unlike the 1D SN simulation used as initial condition, the 3D SNR simulations do not include the radioactive decays of the explosive nucleosynthesis products synthesized in the SN explosion, such as ^{56}Ni or ^{44}Ti. The main effect of radioactive decay would be a slight inflation of the instability-driven structures developed in regions near the decaying elements (Gabler et al. 2017). As the decay time of these species is much lower than the evolution time analyzed here, I assumed at the beginning of my simulations that all the ^{56}Ni and ^{44}Ti are already decayed in ^{56}Fe and ^{44}Ca respectively (see Nadyozhin 1994; Ahmad et al. 2006).

The computational domain describes only one octant of the whole remnant to reduce the computational cost. At the initial condition, the explosion is located at the origin (0,0,0) of the coordinate system. To follow the wide range of space and time scales covered during the expansion of the remnant from the onset of the explosion to the first 5000 years, I adopted the same approach as Orlando et al. (2019). Initially, the domain extends between 0 and 2.19×10^{15} cm in all directions and is covered by a uniform grid with 256^3 zones. The domain is then gradually extended as the forward shock propagates outward and the physical values are remapped in the new domains.

More specifically, each time the forward shock gets close to 90% of the domain size, the domain is extended by a factor of 1.2 in all directions, maintaining a uniform grid of 256^3 grid points. As discussed by Ono et al. (2013) this approach is reliable because it does not introduce errors larger than 0.1% after 40 remappings. In such a way, the finest spatial resolution is $\sim 10^{13}$ cm at the beginning of the 3D simulations, and because of the expansion of the system the resolution is $\sim 10^{17}$ cm at the end of simulation time. The simulations therefore span from an initial domain of $(2.19 \times 10^{15}$ cm$)^3$ up to $(\sim 5.8 \times 10^{19}$ cm$)^3$. Equatorial symmetric boundary conditions [1] with respect to x=0, y=0 and z=0 planes are considered, while fixed pre-shock values conditions are assumed at all other boundaries. I checked the effects of spatial resolution on the remnant evolution in Appendix A, and verified that the main conclusions are not significantly affected by the resolution adopted (see Appendix A for further details).

The ejecta distribution is expected to be characterized by small-scale clumping of material and larger-scale anisotropies (e.g., Orlando et al. 2016). Therefore, following Orlando et al. (2012), I introduced small-scale perturbations in the initial ejecta distribution, mimicking the small-scale clumping of ejecta. These inhomogeneities were modeled as per-cell random-density perturbations derived from a power-law probability distribution. All the clumps have an initial size of $\approx 10^{13}$ cm and the density perturbation of each clump is calculated as the ratio of the mass density of the resulting clump to the local (unperturbed) average density in the region occupied by the clump; the maximum density perturbation allowed is a factor of 4. In Sect. 4.2.3 I discuss how post-explosion large-scale anisotropies in the ejecta distribution are modeled.

I describe the CSM around the progenitor star as a spherically symmetric steady wind with a gas density proportional to r^{-2} (where r is the radial distance from the center of explosion):

$$\rho_{\rm wind} = \rho_{\rm ref}\left(\frac{r_{\rm ref}}{r}\right)^2 . \tag{4.7}$$

I assumed that the wind is isobaric with pressure $P_{\rm wind} \sim 10^{-10}$ dyn cm^{-2} to prevent the wind from evolving towards the boundaries of the domain, causing "jumps" in the profile of the wind whenever the domain is extended. This assumption does not affect the

[1] Variables are symmetrized across the boundary and normal components of vector fields flip signs, with the exception of the magnetic field in which only the transverse component flip sign.

results because the forward shock propagates much faster than the stellar wind during the whole evolution.

The CSM is characterized by three parameters: the reference density, the radial distance of the reference density, and the temperature ($n_{\rm ref} = 1$ cm^{-3}, $r_{\rm ref} = 2.5$ pc, and $T_{\rm ref} = 100$ K, respectively). The values considered are within the range of typical values for a progenitor RSG, which is subject to high mass-loss rates ($10^{-5} - 10^{-4}$ M$_\odot$ yr^{-1}) and very slow winds (20 - 100 km s^{-1}) (Dwarkadas 2005; Crowther 2001). Assuming $\dot{M} = 5 \times 10^{-5}$ M$_\odot$ yr^{-1} and $v_{\rm w} = 20$ km s^{-1}, I derived the reference mass density as $\rho_{\rm ref} = \dot{M}/(4\pi v_w r_{\rm ref}^2)$ which corresponds to a particle number density $n_{\rm ref} \approx 1$ cm^{-3}. In such a tenuous environment, the radiative losses would become relevant after $t_{rad} > 10^4$ years (see Blondin et al. 1998; Orlando et al. 2005; Miceli et al. 2006; Lee et al. 2015), a timescale much greater than the simulated time ($t = 5000$ years).

The simulations include the effect of an ambient magnetic field. This field is not expected to influence the overall dynamics of the system which is characterized by high values of the plasma β (i.e., the plasma pressure dominates over the magnetic one). MHD codes are generally more diffusive than HD codes because they use approximate Riemann solvers. However, I decided to include the effects on an ambient magnetic field in the simulations because the field can play a relevant role in limiting the growth of HD instabilities that would develop at the border of ejecta clumps and anisotropies and that are responsible for their fragmentation (Fragile et al. 2005; Shin et al. 2008; Orlando et al. 2008, 2012, 2019). Following Orlando et al. (2019), the field configuration adopted is the "Parker spiral", which is the field resulting from the rotation of the progenitor star and the expanding stellar wind (Parker 1958). The Parker spiral can be described in spherical coordinates (r, θ, ϕ) as:

$$B_{\rm r} = \frac{A_1}{r^2} \tag{4.8}$$

$$B_\phi = -\frac{A_2}{r} \sin\theta. \tag{4.9}$$

The previous parameters are set to $A_1 = 3 \times 10^{28}$ G cm^2 and $A_2 = 8 \times 10^{10}$ G cm in order to produce a magnetic field of the order of 10 G at the surface of the progenitor star (e.g., Tessore et al. 2017 and references therein).

4.2.3 Post-explosion large-scale anisotropy

I considered the case of a post-explosion large-scale anisotropy located in the inner initial ejecta distribution. My aim is to study whether or not and how the remnant structure and morphology keep an imprint or 'memory' of post-explosion anisotropies and whether or not these anisotropies have an effect on the evolution and mixing of the different metal-rich layers of the progenitor star. The anisotropy included in my model does not arise from the 1D SN simulation, but is set in the initial conditions of the SNR model. Explaining the physical origin of these initial anisotropies is beyond the scope of this work; I focused on the effects of a large-scale post-explosion anisotropy on the evolution of a SNR and I investigated how the different initial parameters of the anisotropy might determine the final shape of the remnant.

The anisotropy is described, for simplicity, as an overdense sphere in pressure equilibrium with the surrounding ejecta whose center lies on the z-axis (therefore only a quarter of the sphere is modeled). I investigated possible numerical effects which may develop by assuming the overdense sphere propagating along the z-axis by exploring a case of a clump with its center located at $\sim 45^{\circ}$ in the plane $(x, 0, z$; see Appendix B for further details). I found that simulations assuming the sphere propagating either along the z-axis or at $\sim 45^{\circ}$ in the plane $(x, 0, z)$ produce very similar results on the timescale considered (5000 years) and I concluded that the numerical effects (if any) due to the propagation of the bullet along the z-axis have a negligible impact on the evolution of the anisotropy of the ejecta.

The geometrical properties of the anisotropy are parametrized by its distance from the center (D), and its radius (r). I considered two values of D, associated with different layers of the exploding star, namely: the interface between ^{56}Fe/^{28}Si-rich regions at $D = 0.24\ R_{\rm SNR}$ (where $R_{\rm SNR}$ is the initial radius of remnant) and the ^{56}Fe-rich region at $D = 0.15\ R_{\rm SNR}$. I explored two values for the clump radius, namely $r = 0.05\, R_{\rm SNR}$ and $r = 0.04\, R_{\rm SNR}$, both consistent with the characteristic size of clumps generated by Rayleigh-Taylor (RT) instability (seeded by flow structures resulting from neutrino-driven convection) in SN explosion simulations (e.g., Kifonidis et al. 2006; Gawryszczak et al. 2010). I explored anisotropies with density between 500 and 750 times that of the surrounding ejecta at distance D (density contrast $\chi_{\rm n}$), and with radial velocity between two and seven times that of the surrounding ejecta (velocity contrast

χ_v), making sure that the maximum speed of the clump does not exceed the velocity of the fastest ejecta in the outermost layers. Wongwathanarat et al. (2017) showed that fast and high-density large-scale anisotropies/plumes with high concentration of ^{56}Ni and ^{44}Ti can emerge from neutrino-driven SN explosions. Some other authors have predicted that high-velocity ejecta components might be produced in the presence of magnetic fields that are anchored to a rapidly rotating proto-neutron star (e.g., Takiwaki et al. 2009). The anisotropies parametrized in this paper assume the same chemical composition as the surrounding ejecta region, i.e., iron alone or iron and silicon when $D = 0.15$ and $D = 0.24$, respectively. A summary of the cases explored is given in Table 4.1.

Previous simulations of ejecta bullets in a SNR performed by Miceli et al. (2013) and Tsebrenko & Soker (2015) showed that clumps with initial values of $\chi_n \leq 100$ are able to reach the SNR shock front without being dispersed by the interaction with the reverse shock. At odds with those simulations which adopt power-law density profiles for the ejecta distribution and start tens of years after the SN event, my simulations include a self-consistent description of the initial ejecta density profile (derived from 1D SN simulations) which shows a high-density thick shell in the innermost regions of the ejecta (see left boxes of Fig. 4.2). As a result, I find that higher density contrasts ($\chi_n > 500$) are necessary for the clumps to overcome this overdense structure and to eventually protrude the forward shock. The maximum initial mass of the anisotropies considered is ~ 0.25 M$_\odot$ ($< 2\%$ of the initial ejecta mass) with a maximum kinetic energy of $\sim 4 \times 10^{49}$ erg ($< 3\%$ of the total initial kinetic energy of the ejecta). I note that these values are very similar to those estimated for the Si-rich jet-like feature observed in Cassiopeia A (Orlando et al. 2016) and to those inferred for the shrapnel G in the Vela SNR (García et al. 2017).

4.3 Results

4.3.1 The case of a spherically symmetric explosion

I first considered the case of a spherically symmetric SN explosion with small-scale (isotropically distributed) clumps of ejecta, without including any large-scale anisotropies (hereafter, the spherical model) to study the spherically symmetric expansion of the

Table 4.1: Parameters describing the initial conditions for the models following the evolution of a post-explosion anisotropy of ejecta.

Model	D ($R_{\rm SNR}$)	r ($R_{\rm SNR}$)	$\chi_{\rm n}$	$\chi_{\rm v}$
Si-R5-D750-V5	0.24	0.05	750	5
Si-R5-D750-V4	0.24	0.05	750	4
Si-R5-D750-V3	0.24	0.05	750	3
Si-R5-D750-V1	0.24	0.05	750	1
Si-R5-D600-V5	0.24	0.05	600	5
Si-R5-D600-V4	0.24	0.05	600	4
Si-R5-D600-V3	0.24	0.05	600	3
Si-R5-D500-V5	0.24	0.05	500	5
Si-R5-D500-V4	0.24	0.05	500	4
Si-R5-D500-V3	0.24	0.05	500	3
Fe-R5-D750-V7	0.15	0.05	750	7
Fe-R5-D750-V6	0.15	0.05	750	6
Fe-R5-D750-V5	0.15	0.05	750	5
Fe-R5-D750-V3	0.15	0.05	750	3
Fe-R5-D750-V2	0.15	0.05	750	2
Fe-R5-D600-V7	0.15	0.05	600	7
Fe-R5-D600-V6	0.15	0.05	600	6
Fe-R5-D500-V7	0.15	0.05	500	7
Fe-R5-D500-V6	0.15	0.05	500	6
Fe-R5-D500-V5	0.15	0.05	500	5
Fe-R5-D500-V3	0.15	0.05	500	3
Fe-R5-D500-V2	0.15	0.05	500	2
Fe-R4-D750-V7	0.15	0.04	750	7
Fe-R4-D750-V6	0.15	0.04	750	6
Fe-R4-D500-V7	0.15	0.04	500	7
Fe-R4-D500-V6	0.15	0.04	500	6

remnant and the evolution of its chemically homogeneous layers.

Figure 4.3 shows the 2D cross-sections through the $(x, 0, z)$ plane of density at different evolutionary stages for the spherical model (left panel). After 100 years of evolution, it is possible to see HD instabilities (RT, Kelvin-Helmholtz shear instability; e.g., Gull 1973; Chevalier 1976; Fryxell et al. 1991; Chevalier et al. 1992) developing as finger-like structures at the interface between ejecta and shocked CSM (as already shown by numerical simulations in Dwarkadas & Chevalier 1998; Wang & Chevalier 2001), thus driving the mixing between the ejecta and the ambient surrounding material. During this evolutionary phase, the over-dense internal shell in the ejecta expands and is clearly visible in the density distribution. At the age of 1000 years, the reverse shock reaches the over-dense internal shell. This allows the over-dense shell to enter in the mixing region causing the destruction of the shell itself by the HD instabilities at $t = 5000$ years. At the end of the simulation, the SNR reaches a radius of $\approx 4 \times 10^{19}$ cm (≈ 13 pc).

Among all the elements considered in the simulations, radioactive nuclei (such as ^{56}Ni and ^{44}Ti) synthesized during the explosion and their decay products are very important because they are produced in the innermost regions of the exploding star, which makes them excellent probes of the internal conditions that lead to the determination of the explosion mechanism and of the shock-wave dynamics during the earliest phases of SN outbursts. For this reason, the study of these elements is key to connecting explosion models to observations and to deducing important constraints on the underlying processes. Radioactive ^{56}Ni and ^{44}Ti transform into the stable isotopes ^{56}Fe and in ^{44}Ca, respectively, with a half-life of < 100 years (Nadyozhin 1994; Ahmad et al. 2006). As mentioned in Sect. 4.2, since I am interested in investigating the matter mixing and evolution of the remnant at epochs longer than 100 years, and recalling that my model does not include the radioactive decay of the elements (see Section 4.2.2), I assume that all the ^{56}Ni and ^{44}Ti are already decayed to ^{56}Fe and ^{44}Ca, respectively, at the beginning of my simulations.

Figure 4.4 displays the ejecta mass distribution of selected elements versus the radial velocity at different epochs during the remnant expansion. The elements appear stratified: ^{56}Fe is concentrated in the slower and innermost part of the ejecta, approximately at 30% of the radius of the initial remnant, inside the dense shell seen in the density distribution in Fig. 4.2, along with the other heavy elements (as ^{44}Ca). ^{28}Si envelopes

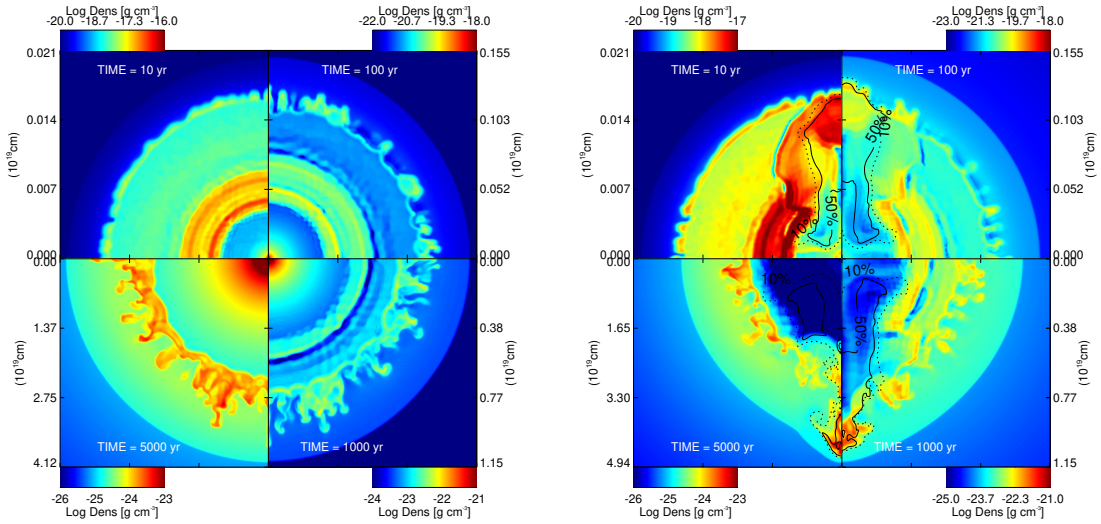

Figure 4.3: Density distributions in the $(x, 0, z)$ plane at different simulation times for a spherically symmetric explosion (left-panel) and for model Fe-R5-D750-V6 of Table 4.1 (right-panel). From top left clockwise: $t = 10$, $t = 100$, $t = 1000$ and $t = 5000$ years from the explosion. The units in the color bars are g cm^{-3} logarithmically scaled. The color-coded density scale is shown close to each quadrant. In the right panel the contours enclose the computational cells consisting of the original anisotropy material by more than 50% (solid line) and 10% (dotted line). See also online Movie 1 and 2 for an animated version.

the inner ^{56}Fe, whereas ^{16}O and ^{12}C are prominent at the bottom of the ^{4}He shell. The outer half of the radial ejecta distribution is dominated by ^{4}He and ^{1}H.

By looking at the mass distribution of the selected elements at various times, I observe how the overall composition of the ejecta changes during expansion of the remnant (see Fig. 4.4). The overall structure and composition of the unshocked ejecta do not change significantly over the timescale considered, although some small differences in the innermost layers are present due to some numerical diffusivity of the code. This indicates that the unshocked ejecta expand almost homologously until they start to interact with the reverse shock. This is shown in Fig. 4.4, where the profiles of the elements with velocity < 1500 km s^{-1} remain almost unchanged at all epochs. In the unshocked ejecta, I observe a large fraction of ^{56}Fe and ^{44}Ca, together with the low-velocity tail of the ^{28}Si distribution. Instead, the profiles of the elements at a greater distance from the center of the explosion, that is, the elements with high-velocity components, are strongly influenced by their interaction with the reverse shock and the CSM. These elements are strongly decelerated in the intershock region and consequently mixed by HD instabilities. This produces a homogenization of the different profiles in these regions: the overall shapes of the high-velocity tails of the mass distributions of shocked elements are more similar to each other and characterized by steep slopes, suggesting a significant mixing between layers of different chemical composition due to HD instabilities developing at the contact discontinuity (see also Wongwathanarat et al. 2017 for the effects of HD instabilities on the mass distribution versus the radial velocity).

Nevertheless, it is important to note that the chemical distribution generated during the immediate aftermath of the SN (i.e., the onion-skin chemical layering) is roughly preserved after 5000 years of evolution. Thus, for a spherically symmetric SN explosion, it is not possible to reproduce the inversion among the innermost chemical layers (e.g., Wang & Chevalier 2002; Wang 2011; Orlando et al. 2016), as observed for example in Cassiopeia A (e.g., Hughes et al. 2000), if the ejecta are characterized only by small-scale clumping.

4.3.2 Effect of large-scale anisotropy

As seen in Section 4.3.1, the ideal case of a spherically symmetric explosion cannot reproduce the complex morphology of an evolved SNR, which is in good agreement

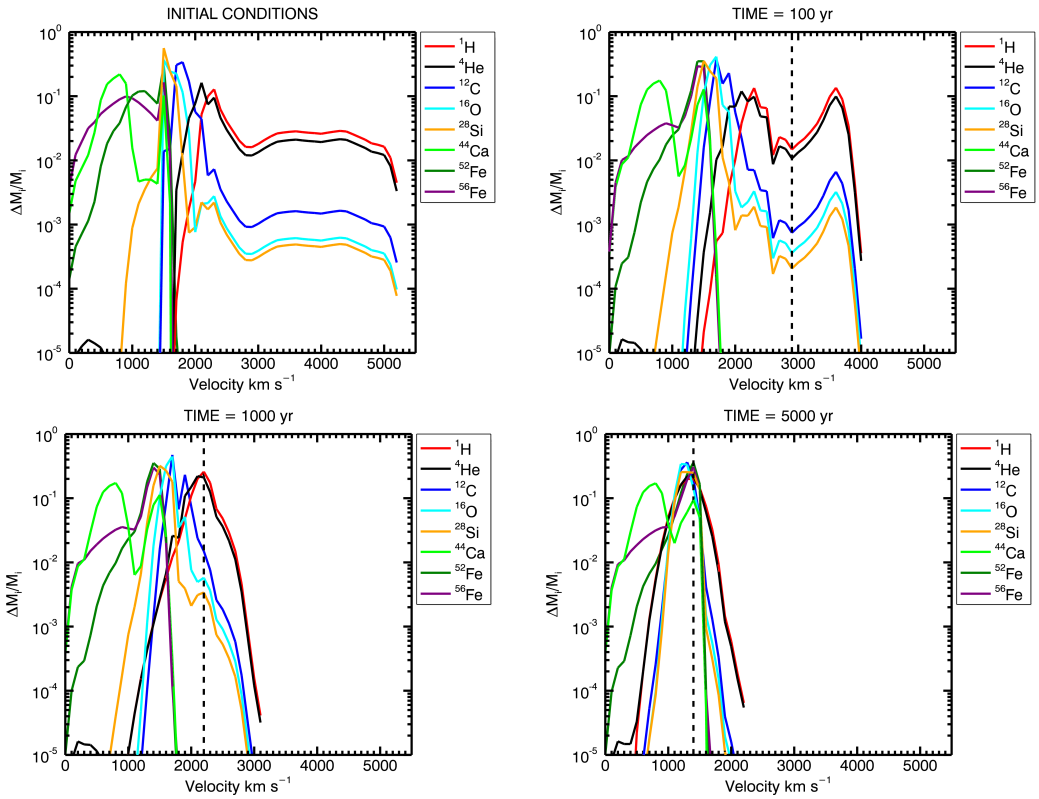

Figure 4.4: Mass distributions of selected elements as a function of radial velocity for the spherically symmetric explosion at the labeled years from the explosion. The upper left panel shows the initial conditions from Ono et al. (2020). Only the dominant fractions are considered. M_i is the total ejecta mass of element i, ΔM_i is the mass of the i-th element in the velocity range between v and $v + \delta v$. The size of the velocity bins δv is 100 km s^{-1}. The black dashed vertical line shows the approximate reverse shock position in each panel.

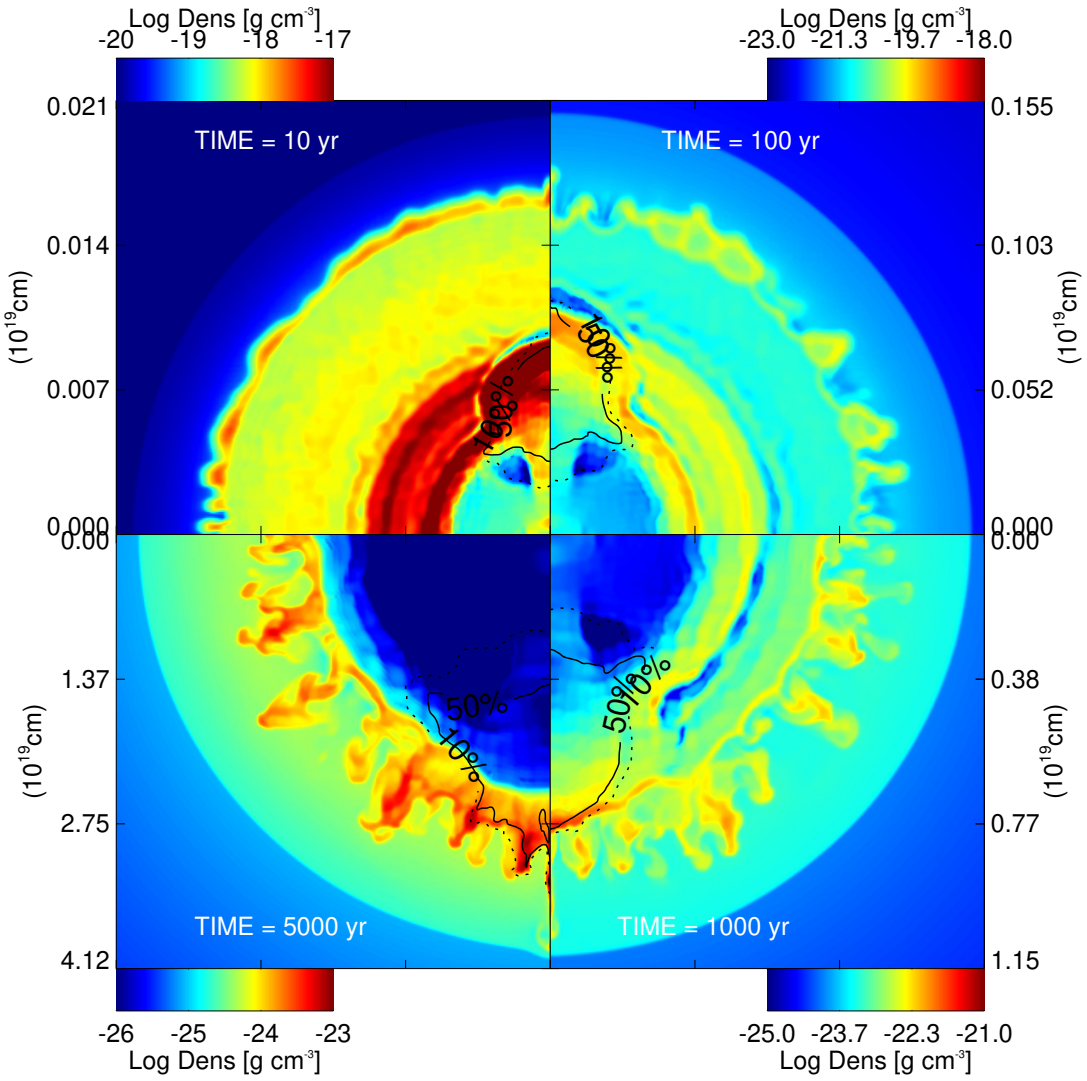

Figure 4.5: Same as the right panel of Fig. 4.3 but for model Fe-R5-D750-V3 (see Table 4.1)

with the fact that most of the CC-SNe are believed to explode asymmetrically (Maeda et al. 2008; Wongwathanarat et al. 2013; Janka et al. 2016; Janka 2017; O'Connor & Couch 2018; Burrows et al. 2019). The physical characteristics of the SN explosion generate asymmetric expansion and strong inhomogeneities that have a complex influence on the evolution of the SNR. Here I consider a possible example of a dynamical event that can cause strong mixing and overturning of the chemical layers in the ejecta. I studied the effects of a post-explosion anisotropy generated soon after the shock breakout. Multiwavelength observations show the presence of clump structures in the ejecta of CC SNRs (Aschenbach et al. 1995; Miceli et al. 2008; García et al. 2017; Park et al. 2004; Katsuda et al. 2008a; Fesen et al. 2006). I model the anisotropy as a spherical clump of radius r, with its center located on the z axis, at a distance D from the origin, as explained in Sect. 4.2.3.

As shown in Table 4.1, I explored the case of a clump located either at $D = 0.15$ or at $D = 0.24$, corresponding to the initial ^{56}Fe-rich internal layer and between the ^{56}Fe- and ^{28}Si-rich layers, respectively (see the top left panel in Fig. 4.4).

The right panel of Fig. 4.3 shows a 2D cross section through the $(x, 0, z)$ plane of density distribution of the model Fe-R5-D750-V6 at four different evolution times (but qualitatively the overall evolution is similar for all the cases explored). The top-left quadrant shows the system 10 years after the beginning of the simulation, when the clump has already overcome the dense shell initially located at about 30% of the radius of the ejecta and the topmost part of the clump has reached the reverse shock. At this stage, the clump has an elongated structure along the z-axis, from the central region of the remnant to the reverse shock. Only the head of the clump is still significantly overdense with respect to the surrounding ejecta. The top-right quadrant shows the system at 100 years. The clump has not changed its morphology, but its topmost part interacts with the intershock region. RT instabilities start to develop at the interface between ejecta and shocked CSM. After 1000 years of evolution (bottom right quadrant) the part of the clump in the intershock region is partially eroded by the HD instabilities, while the passage of the clump has left a low-density strip region in the inner part of the ejecta. This phase lasts $\approx$ 2000 years; the wake behind the ejecta clump is then filled in eventually as the pressure gradient drives lateral expansion of the ejecta to fill the void. For model Fe-R5-D750-V7 and Si-R5-D600-V4, I find that at $\sim$ 2500 years, the clump reaches a velocity of $\sim$ 3000 km s^{-1}, similarly to what was found very re-

cently for the runaway knot in N132D (3650 km s^{-1}, Law et al. 2020). The bottom-left quadrant shows the clump at 5000 years and it is possible to see the characteristic supersonic bow shock of the clump protruding beyond the SNR forward shock. At this evolutionary stage, the low-density region has been filled by the surrounding material. An exception to this trend is represented by models Fe-R5-D750-V3 (see Fig. 4.5) and Fe-R5-D500-V3. In these two cases, the clump penetrates into the high-density shell without overcoming it, remaining stuck inside it. In this case, the clump expands together with the surrounding ejecta and eventually becomes completely fragmented by the interaction with the reverse shock.

Figure 4.6 shows the spatial distribution of ^{56}Fe (red), ^{28}Si (green) and ^{16}O (blue) in the ejecta of the remnant at $t = 5000$ yr for different model setups (see Table 4.1). Figure 4.6A shows four models in which the large-scale clump is initially located at $D = 0.24$, that is, between the ^{28}Si and the ^{56}Fe shells, with $r = 0.05$. In each of these cases, the clump can produce a remarkable jet-like structure of ^{28}Si-rich ejecta. This structure protrudes beyond the SNR forward shock in all cases, except for model Si-R5-D500-V3 (Fig. 4.6A-1). I point out that the ^{28}Si-rich collimated structure has overcome the ^{16}O-rich layer of ejecta at this evolutionary stage. Moreover, I found that after ≈ 350 years, for models Si-R5-D500-V4 (Fig. 4.6A-2) and Si-R5-D600-V4 (Fig. 4.6A-4), this Si-rich jet-like structure has already overcome the ^{16}O layer, which is similar to a feature observed in the northeast and southwest regions of Cassiopeia A (e.g., DeLaney et al. 2010; Milisavljevic & Fesen 2013).

My simulations show that a velocity contrast $\chi_{\rm v} > 2$ is necessary to allow the clump to overcome the high-density shell. The length of the jet-like feature depends on the initial density contrast of the clump, as can be seen in quadrant (1) of Fig. 4.6A ($\chi_{\rm n} = 500$, $\chi_{\rm v} = 3$), where the position of the bow-shock of the clump has its lowest value (4.12×10^{19} cm; ≈ 13 pc) among the cases considered here. The shape of the jet-like structures appears somehow "curly", with the exception of Si-R5-D600-V3 (quadrant 3 of Fig. 4.6A), which has a more regular shape and is more collimated along the z-axis. The clump has been strongly eroded at this time.

The final distribution of ^{56}Fe, ^{28}Si, and ^{16}O in the remnant in the case of $D = 0.15$ (clump entirely made of ^{56}Fe) and $r = 0.05$ is shown in Figs. 4.6B, C. In both cases, the clump produces a ^{56}Fe-rich region along the z-axis, extending from the center of the remnant to the intershock region where it mixes with the ^{16}O layer. I find that the clump

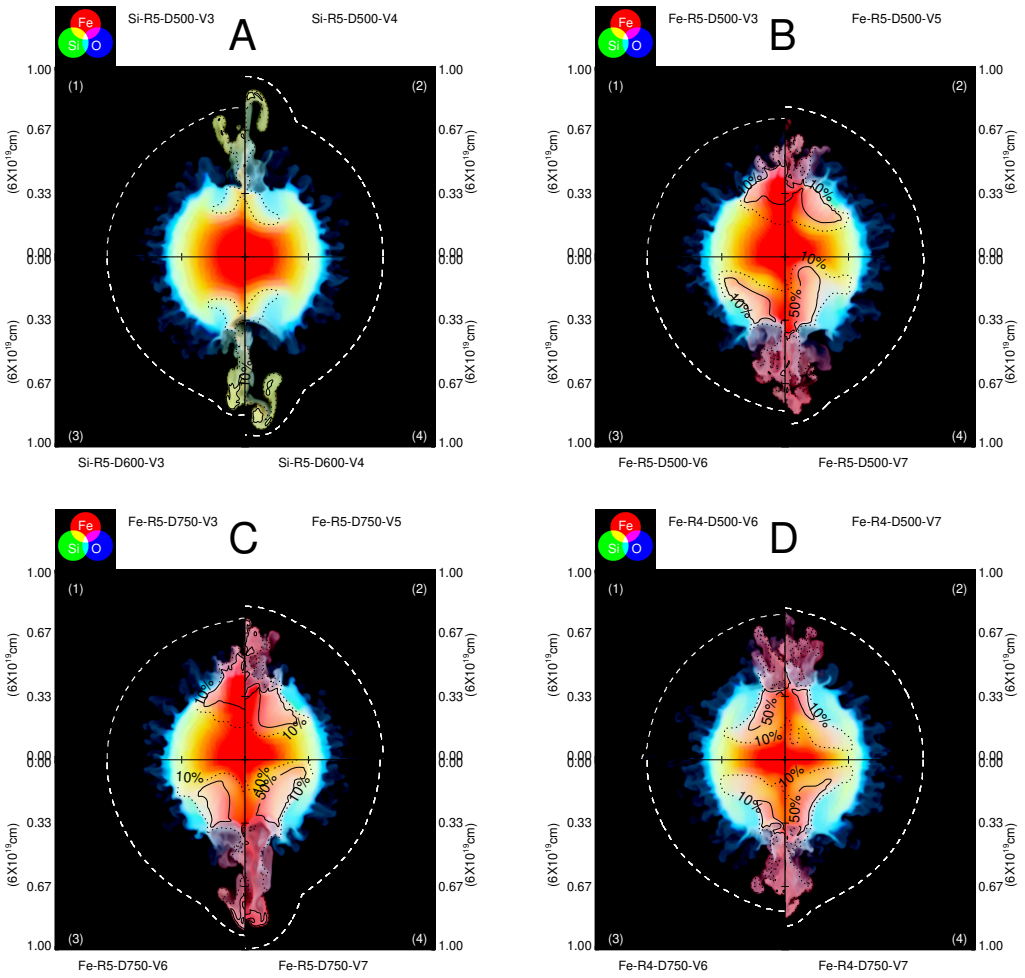

Figure 4.6: Color-coded images of the logarithm of the ejecta mass fraction (¿ 10^{-4}) distributions at the end of the simulation ($t \approx 5000$ years) for different models (the model as presented in Table 4.1 is reported near each quadrant) in the $(x, 0, z)$ plane of ^{56}Fe (red), ^{28}Si (green), and ^{16}O (blue). Black contours enclose the computational cells consisting of the original clump material by more than 50% (solid line) and 10% (dotted line). The white dashed line represents the projected position of the forward shock; see also online Movie 3, 4, 5, and 6 for an animated version.

can protrude the forward shock only if its velocity contrast is $\chi_v \geq 6$, which is a factor of two higher than that obtained for $D = 0.24$. This is because, for $D = 0.15$, the clump is located in an inner and slower region (due to the linearly increasing velocity profile of the ejecta, described in Section 4.2), and therefore a higher velocity contrast is needed with respect to the case with $D = 0.24$. Moreover, for $D = 0.24$, the clump is at the inner border of the high-density shell, and so the interaction with the shell occurs at the early stages of evolution when the clump-to-shell mean density ratio (in the following η) is $\eta \geq 14$. On the other hand, for $D = 0.15$, the clump evolves in a lower pressure region, and therefore the clump undergoes a significant expansion before interacting with the dense shell and $\eta \leq 0.25$ at the interaction. This effect causes the clump to struggle to overcome the dense shell, leading to a wider jet-like structure with respect to cases with $D = 0.24$. I also find that the initial clump size (r) does not affect the mixing of ^{56}Fe in the outer layers (see Fig. 4.6D) within the range of values explored.

In the cases explored, I observed that the clump pushes the heavy elements (especially ^{56}Fe and ^{28}Si) into the outer and high-speed regions of the ejecta, as has been observed in other core-collapse SNe such as SN1987A (Haas et al. 1990; Utrobin et al. 1995), Cassiopeia A (Grefenstette et al. 2014, 2017; Siegert et al. 2015), Vela (García et al. 2017), and, very recently, N132D (Law et al. 2020). According to the exploration of the parameter space I have performed, the average chemical stratification of the ejecta is roughly preserved in regions not affected by the large-scale anisotropy (e.g., x-axis in Fig. 4.6). In these regions, the evolution of the ejecta is similar to that described in section 4.3.1 and the forward shock reaches approximately the same distances in all the cases explored (the differences shown in quadrants (2) and (4) of Fig. 4.6B and C are due to slightly different simulation times, of the order $\approx$ 10 years).

Shock-heated plasma emits X-ray thermal emission, especially through line emission, giving us a valuable tool to measure the elemental composition and spatial distribution inside the remnant. From the simulations, I derived the mass of shocked ^{56}Fe and ^{28}Si normalized to the value of the total mass of the respective element for the different models as a function of time (see Figs. 4.7- 4.8). For both $D = 0.15$ and $D = 0.24$, the final amount of shocked ^{56}Fe is at least two times larger than that obtained for the case of a spherically symmetric explosion.

For $D = 0.15$ (see Fig. 4.7), during the first 300 years, the amount of shocked ^{56}Fe depends both on the size and on the initial density contrast of the clump, increasing with

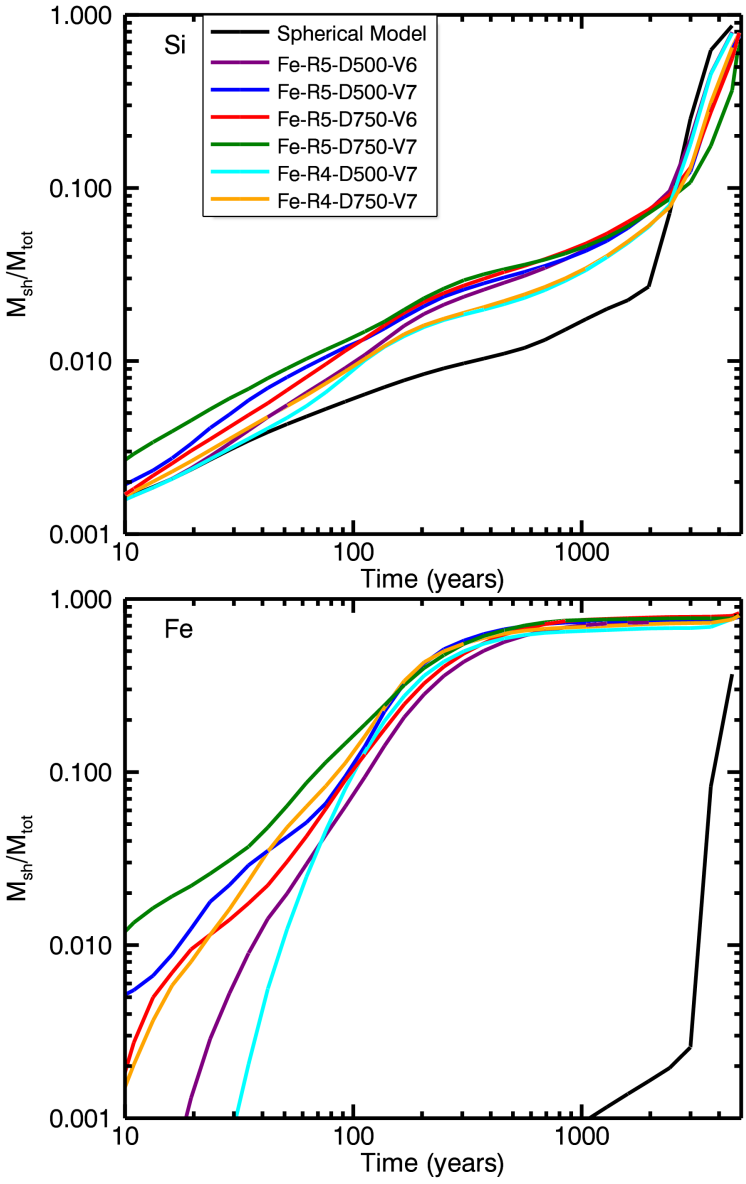

Figure 4.7: Mass of shocked ^{28}Si (upper panel) and ^{56}Fe (lower panel) vs. time for models assuming a clump initially located at $D = 0.15$ and characterized by different parameters (see Table 4.1). The shocked mass is normalized to the total mass of the relative element.

size and contrast. However, after 3000 yr, the reverse shock interacts with the ^{56}Fe shell even without any initial clump, and therefore the amount of shocked ^{56}Fe observed at the end of the simulations is not entirely due to the initial clump. As for the shocked ^{28}Si, I find that the final amount of shocked mass does not show any strong dependence on the initial clump parameters or on its initial dimension or position. The main cause of this is the interaction of the reverse shock with the Si-rich shell, which shocks a relevant part of the ^{28}Si-rich material regardless of the presence of the initial clump, thus making the contribution of the clump negligible. For $D = 0.24$ (see Fig. 4.8) on the other hand, the amount of shocked ^{56}Fe after 5000 yr is not strongly affected by the initial clump parameters. This is expected because the jet-like structure is mostly made of ^{28}Si for models with $D = 0.24$, as shown in Fig. 4.6. On the other hand, the velocity contrast $\chi_{\rm v}$ plays an important role in determining the beginning of the interaction between the reverse shock and the ^{56}Fe-rich ejecta. I observed that, for $\chi_{\rm v} = 4$, the reverse shock heats the ^{56}Fe-rich material ~ 90 yr earlier than the case with $\chi_{\rm v} = 3$ (see upper panel of Fig. 4.8). However, as seen for the ^{56}Fe, I find that the initial velocity contrast $\chi_{\rm v}$ affects the timing of the interaction between the reverse shock and the ^{28}Si-rich ejecta, but only for $D = 0.24$.

To deepen our understanding of the role played by the clump, I also computed the amount of shocked ^{28}Si (upper panel of Fig. 4.9) and ^{56}Fe (lower panel of Fig. 4.9) as a function of time in three different regions of the ejecta, namely: (i) cells within 45° of the z-axis, that is, those enclosing the ejecta clump and mostly affected by its evolution; (ii) cells within 15° of the equatorial plane, which is those least affected by the clump; and (iii) all the other cells. The shocked mass is normalized to the total mass of the respective element in the corresponding region. I compared the spherically symmetric explosion (green lines) and model Fe-R5-D750-V7 (red lines, see Table 4.1). For model Fe-R5-D750-V7, in the region within 45° of the z-axis the mass of the ^{28}Si (upper panel) has been shocked by a larger fraction compared to the other regions, but only up to $t = 4000$ yr. At odds with the ^{56}Fe (lower panel), after $t = 4000$ yr the reverse shock reaches the ^{28}Si layer in the regions away from the jet-like structure making these regions the main contributors to the shocked mass of ^{28}Si. Looking at the evolution of the shocked mass of ^{56}Fe (lower panel) for model Fe-R5-D750-V7, the effect of the clump stands out in cells within 45° of the z-axis, while the other regions follow the same evolution as the spherically symmetric explosion. However, the presence of the

clump influences the regions within $45°$ of the equatorial plane shocking 40% more mass of the region compared to the spherically symmetric explosion.

4.3.3 Synthesis of X-ray emission

In this chapter I showed that the presence of an anisotropy can significantly influence the shape of the remnant leading to the formation of large-scale jet-like structures and protrusions of the remnant outline. The matter-mixing strongly depends on the physical and chemical characteristics of the initial anisotropy and it is now interesting to have a probe of such mixing by looking at the X-ray spectra. When the shock wave interacts with the matter, the latter is heated up to temperatures of several million degrees, leading to X-ray emission. Thus, X-ray spectral analysis is a powerful tool to distinguish between the different spectral signatures of the regions affected by an ejecta bullet and the rest of the evolving remnant between the forward and the reverse shock.

By adopting the approach described in Greco et al. 2020 (see also Miceli et al. 2019), synthetic X-ray spectra have been extracted from the simulations in a format virtually identical to that of *Chandra* ACIS-S observations. The synthesis includes the deviations from equilibrium of ionization and from temperature-equilibration between electrons and protons, and takes into account the chemical composition of ejecta and ISM resulting from the simulations in each computational cell (see e.g., Miceli et al. 2019; Orlando et al. 2019 for more details). For the spectral synthesis, it has been assumed a distance of 1 kpc and a column density $N_H = 2 \cdot 10^{21}$ cm^{-2} with an exposure time of 100 ks. As an example, run Fe-R5-D750-V7 (see Table 4.1) it has been considered, where a clear jet-like feature is evident at an age of $t = 5000$ yr. I selected three regions, identified by the red, black, and green boxes in the upper panel of Fig. 4.10, corresponding to the ejecta bullet protruding the remnant outline (in the following the clump), the wake (namely the low-density strip-region behind the clump, already mentioned in Sect. 4.3.2), and an area of the shell not affected by the anisotropy, respectively. For a distance from the observer of 1 kpc, each of these regions corresponds to a box with angular side $l = 2'$. Synthetic spectra extracted from the three regions are shown in the lower panel of Fig. 4.10.

The main spectral difference between the spectrum extracted from the region enclosing the clump and the other spectra is the bright "false-continuum" emission which

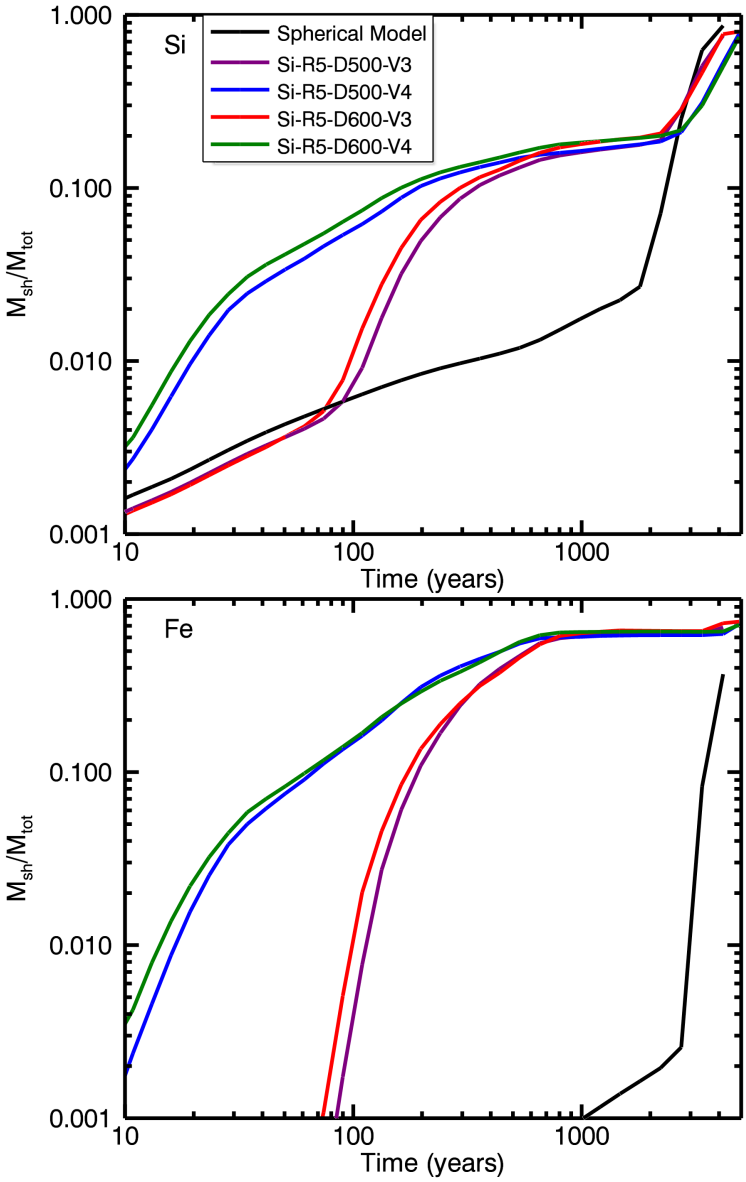

Figure 4.8: Same as Fig. 4.7 but for models with a clump initially located at $D = 0.24$.

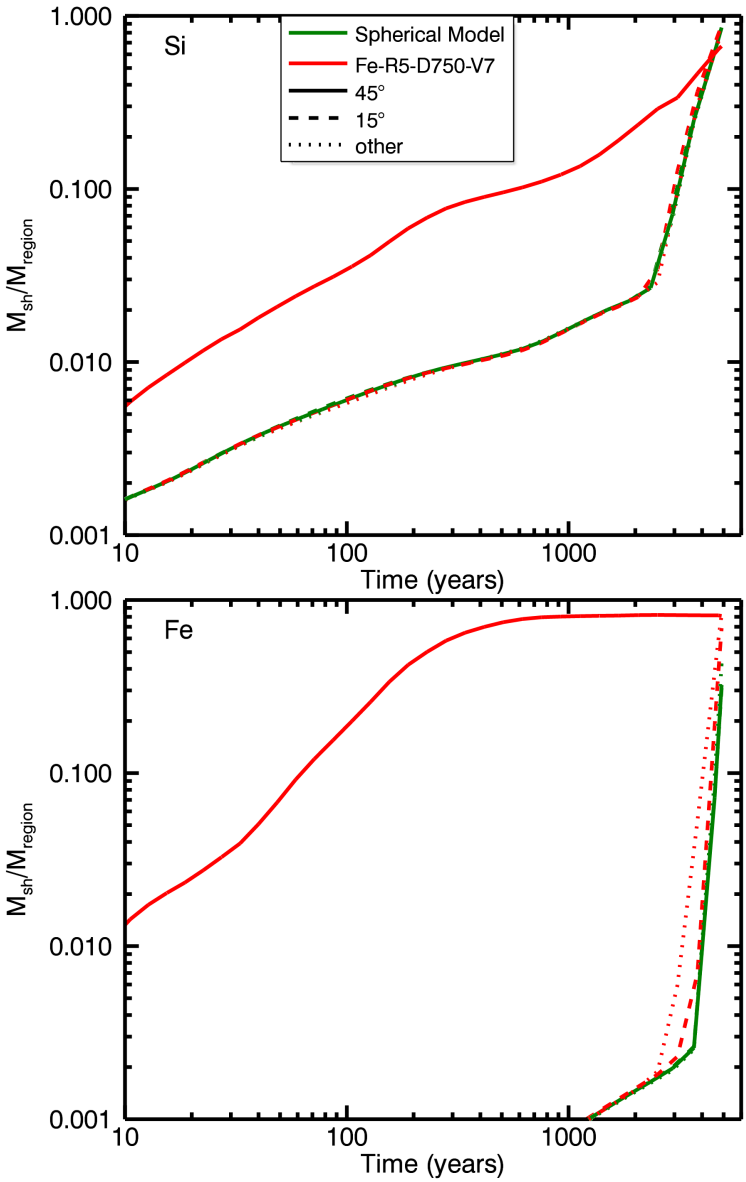

Figure 4.9: Mass of shocked ^{28}Si (upper panel) and ^{56}Fe (lower panel) vs. time for the spherically symmetric explosion (green lines) and for model Fe-R5-D750-V7 (red lines, see Table 4.1). Solid and dashed lines show the shocked mass from cells within 45° of the z-axis and from 15° of the equatorial plane respectively, while the dotted lines show the mass from the others cells. The shocked mass is normalized to the total mass of the relative element in the region considered.

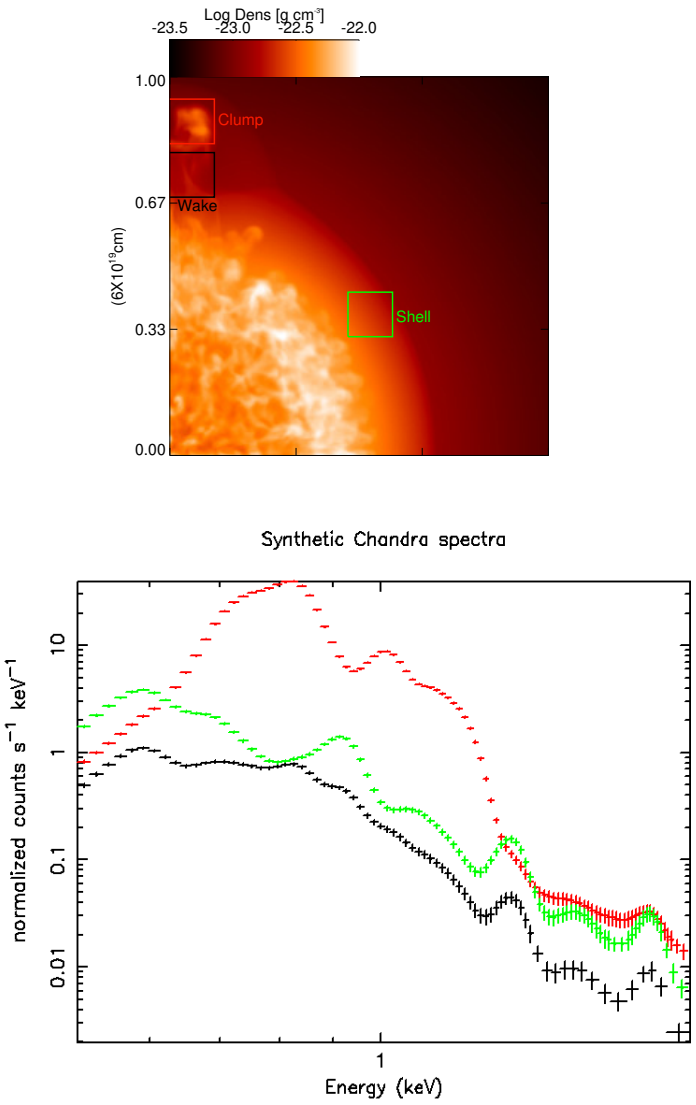

Figure 4.10: Upper panel: Density distribution map integrated along the line of sight (in this case the y-axis) of the run Fe-R5-D750-V7, showing the regions chosen for the spectral synthesis: red for the anisotropy protruding the remnant outline (the clump), black for the wake of the anisotropy, and green for a region of the shell not affected by the anisotropy (the shell). Lower panel: X-ray *Chandra* ACIS-S synthetic spectra in the 0.5-2 keV energy band for the clump (red), the wake (black), and the shell (green).

is due to the blending of Fe XIV-XXIV emission lines at energies around 1 keV. This result shows that the clump spectrum is dominated by the emission of Fe-rich ejecta. Emission lines of other elements such as Mg ($\sim$ 1.3 keV) and Si ($\sim$ 1.8 keV) are fainter in the clump spectrum, because the protrusion of the Fe-rich clump drags away lighter elements. Enhanced Ne (at $\sim$ 0.92 keV), Mg, and Si emission lines are visible in the spectrum of the shell region (green spectrum in Fig. 4.10). The wake spectrum (black spectrum in Fig. 4.10) shows bright Mg and Si emission lines, very low Fe emission (even lower than that in the shell region), and an overall lower emission measure. The emission is fainter because the density is low, as one can see in the integrated density distribution map displayed in the upper panel of Fig. 4.10. The analysis shows that the effects of matter mixing in the ejecta produced by the evolution of a post-explosion anisotropy lead to spectral features in the X-ray band which are detectable through a spatially resolved analysis of X-ray spectra of SNRs.

4.4 Conclusions

In this Chapter, I described a 3D MHD model describing the evolution of a SNR starting soon after the SN explosion and following the interaction of the SN ejecta with the CSM for 5000 years. The initial ejecta structure was modeled by including small-scale clumping of material and larger-scale anisotropy. The simulations are multi-species to trace the life cycle of elements during the whole evolution, from the nuclear reaction network of the SN to the enrichment of the CSM through mixing of chemically homogeneous layers of ejecta.

My simulations allowed me to study the effect of large-scale anisotropy on the evolution and matter-mixing of the ejecta of a SNR and provided a valuable tool to reproduce their observable properties. By synthesizing X-ray spectra from the model I find that it is possible to obtain more detailed diagnostics of ejecta inhomogeneities in CC-SNe by carefully comparing X-ray observations of SNRs with numerical simulations. Thus, these findings can be a useful guide in the interpretation of observations, such as for example the Si-rich shrapnel protruding beyond the front of the primary blast shock wave in the Vela SNR (García et al. 2017) or the fast runaway knot with a significantly high Si abundance recently detected in N132D (Law et al. 2020).

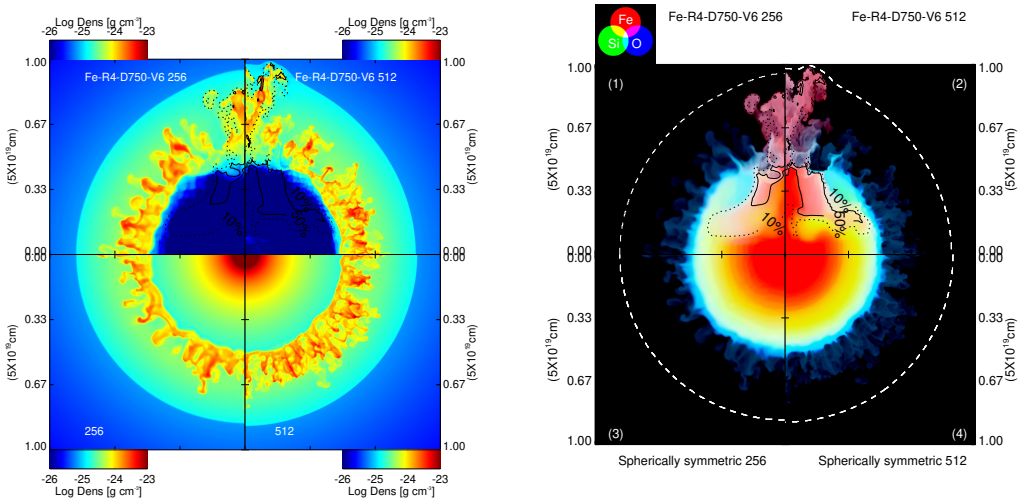

Figure 4.11: Left panel: Density distributions in the $(x, 0, z)$ plane at the end of simulation time for a SN explosion with a large-scale anisotropy (upper quadrants) (runs Fe-R4-D750-V6 and Fe-R4-D750-V6-512pt in Table 4.1) and for a spherically symmetric explosion (lower quadrants), at low resolution (256^3 grid points; left quadrants) and high-resolution (512^3 grid points; right quadrants). Right panel: Same but for color-coded images of the logarithm of the mass fraction distributions of Fe (red), Si (green), O (blue). In the upper quadrants of each panel, the black contours enclose the computational cells consisting of the original anisotropy material by more than 10% (dotted line) and 50% (solid line). The white dashed line represents the approximate position of the forward shock.

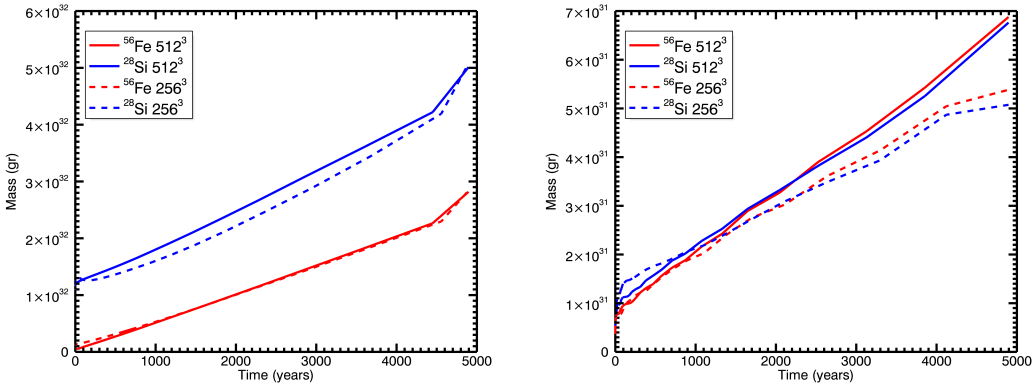

Figure 4.12: Left panel: Amount of ^{56}Fe and ^{28}Si mass vs. time in cells with a mass fraction between 10% and 50% for a spherically symmetric explosion at different resolution. Right panel: Amount of ^{56}Fe and ^{28}Si mass vs. time in cells with a mass fraction between 10% and 50% and with anisotropy material between 10% and 90% for models Fe-R4-D750-V6 (256^3 grid points) and Fe-R4-D750-V6-512pt (512^3 grid points) (see Table 4.1).

Appendix A: Effect of spatial resolution

To ensure that the resolution used to perform the simulations (256^3 grid zones) was sufficient to catch the basic properties of the system evolution, I repeated simulation Fe-R4-D750-V6 but using a uniform grid of 512^3 grid zones (hereafter simulation Fe-R4-D750-V6-512pt) and I did the same for the spherically symmetric explosion simulation. The left panel of Fig. 4.11 shows density distributions in the $(x, 0, z)$ plane at the end of simulation time for both models at different resolutions. The right panel of Fig. 4.11 shows the same as left but for color coded images of the mass fraction distributions of ^{56}Fe, ^{28}Si, and ^{16}O. As expected, the spatial resolution mainly affects the structure of the RT instability: the RT fingers appear more extended and branched in the case of higher spatial resolution (see right quadrants in the panels of Fig. 4.11). As a consequence, the spatial resolution changes the clump structure during its evolution. I also computed the distance of the center of mass of Fe-rich ejecta from the origin of the explosion for models Fe-R4-D750-V6 and Fe-R4-D750-V6-512pt, obtaining a value of $2.9 \cdot 10^{19}$ cm and $3.2 \cdot 10^{19}$ cm respectively, thus showing a slight discrepancy of the order of 10% in the distribution of ^{56}Fe in the two cases. I checked that simulations Fe-R4-D750-V6 and Fe-R4-D750-V6-512pt yield similar results in terms of the amount of shocked

material. I was mainly interested in the mixing between different chemical layers, I therefore computed the amount of ^{56}Fe and ^{28}Si within the cells where the mixing is more relevant for both spherical (left panel of Fig. 4.12) and nonspherical (right panel of Fig. 4.12) models. The profiles shown in Fig. 4.12 are in good agreement between the two models. This proves that, even if the small-scale density structures developing during the propagation of the ejecta bullet depend on the spatial resolution, a resolution of 256^3 uniform grid zones is able to capture the basic properties of the system evolution and of the matter-mixing among different chemical layers.

Appendix B: Boundary effects

In the numerical setup, the large-scale anisotropy, or clump, has been described as a sphere with its center located on the z-axis of the domain (see Sec. 4.2.3). In Section 4.3.2 I show that the presence of this clump can cause a jet-like structure in the SNR that generates a strong mixing between different chemical layers. To ensure that the arise of this structure is not due to numerical artifacts caused by the proximity of the axis to the clump, I repeated simulation Fe-R4-D750-V6 placing the center of the clump at $\approx 45^\circ$ in the (x,0,z) plane (hereafter run Fe-R4-D750-V6-ROT). In Figure 4.13 I compare both models after $t \approx 100$ years of evolution and at the end of the simulation, namely $t \approx 5000$ years after the explosion. The evolution and final density distribution does not change significantly rotating the initial position of the clump out from the z-axis. More specifically, I note that the evolution of the ejecta bullet is indistinguishable in the two cases during the first phase of the simulations (the first 30 years), namely before the wake of the bullet reaches the (reflective) boundaries in run Fe-R4-D750-V6-ROT. In this latter case, the interaction of the wake with the boundaries produces reflection of material which propagates back into the domain. After $\sim$ 100 yr (see upper panel in Fig. 4.13), when the clump overcomes the high-density shell of ejecta and starts to interact with the inter-shock region, I observe a lesser presence of HD instabilities in the model Fe-R4-D750-V6-ROT (left panel) and also some artifacts due to the reflection of material on the boundary during the expansion. For this reason, the mixing of anisotropy material in the two models is slightly different after $\sim$ 100 yr of evolution (see Fig. 4.14). The perturbation of the inner portion of the remnant by the material reflected at the boundaries in run Fe-R4-D750-V6-ROT is the reason why I

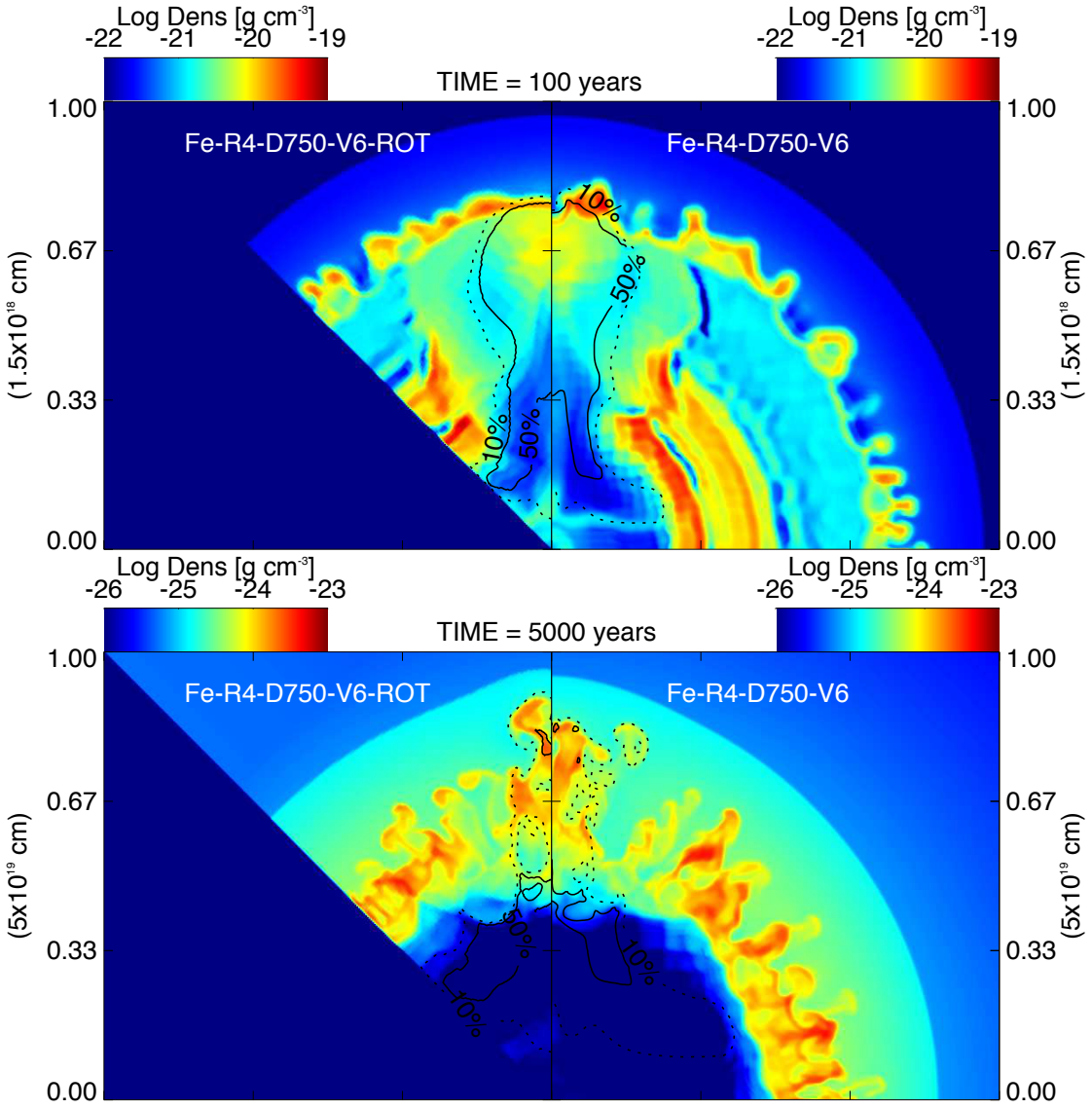

Figure 4.13: Density distribution maps in the (x,0,z) plane at $t \approx 100$ (upper panels) and $t \approx 5000$ years from the explosion (lower panels). Right: Model Fe-R4-D750-V6 (see Table 4.1). Left: Same model with the initial position of the clump located at 45° in the (x,0,z) plane, namely Fe-R4-D750-V6-ROT. On the left panels the (x,0,z) plane from the simulation is rotated to the z-axis for comparison, and thus the lower blue triangle is not part of the computational domain. The contours enclose the computational cells consisting of the original anisotropy material by more than 50% (continuous line) and 10% (dotted line).

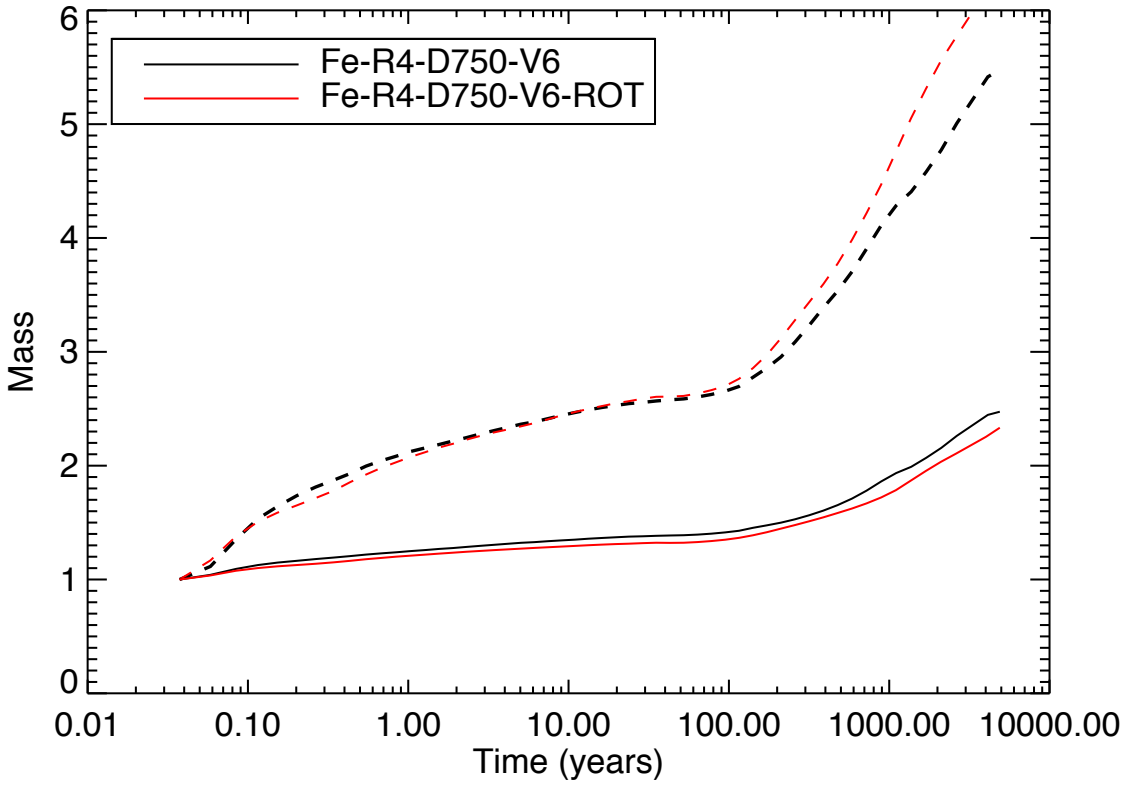

Figure 4.14: Mass vs. time (in logarithmic scale) for the two models compared in Fig. 4.13. Total mass in cells with anisotropy material by more than 10% (continuous line) and in the range 10–90% (dotted line). In every case the mass is normalized to the value of the mass in the first step of the simulation.

preferred to consider the bullet propagating along the z axis rather than at 45° angle from all axes. Nevertheless, even with the perturbations in run Fe-R4-D750-V6-ROT, the evolution of the ejecta bullet in both simulations is very similar, with no significant effects on the final remnant structure (see Sec. 4.3.2). In light of this, I can confirm that the jet-like structures observed in the simulations discussed in the paper do not arise from numerical artifacts.

Chapter 5

Multiple accelerated particle populations in the Cygnus Loop with *Fermi*-LAT

In the previous chapter, I showed how the evolution of the physical and morphological properties of a SNR can be strongly affected by the presence of a small anisotropy. As discussed in Section 1.4, the interaction between the SNR and its environment plays a crucial role in the study of the SNRs. In this chapter, I report on the analysis conducted on a SNR whose interaction with the ISM affected the remnant's shock speed and consequently on the particle acceleration mechanism: the Cygnus Loop. I performed the analysis of the γ-ray emission detected by the Large Area Telescope (LAT) onboard the *Fermi Gamma-ray Space Telescope* over 11 years in the Cygnus Loop region. By performing a detailed morphological analysis, I was able to disentangle the contribution of different accelerated particle populations to the entire non-thermal emission of the Cygnus Loop. Part of this work has been performed at the Commissariat à l'énergie atomique et aux énergies alternatives (CEA) institute of Saclay.

5.1 Introduction

It is widely accepted that SNRs accelerate Cosmic Rays (CR) through their fast shock waves that propagate into the Interstellar Medium (ISM). In particular, SNRs are

characterized by the Diffusive Shock Acceleration (DSA) process (Malkov & Drury 2001; Bell 1978a,b; Blandford & Ostriker 1978) that results in non-thermal emission observed from radio to γ-ray . Strong γ-ray emission has been observed by the *Fermi* Large Area Telescope (LAT) and the AGILE satellite in SNRs interacting with interstellar material. These SNRs are typically evolved and extended middle-aged ($>$ 10 kyr) remnants interacting with molecular clouds, with a characteristic high-energy break around 1-20 GeV (Giuliani et al. 2011; Ackermann et al. 2013). The spectrum of these sources can be explained by π^0 decay emission of accelerated CR protons in the shocks of SNRs or, alternatively, by the re-acceleration of ambient Galactic CR inside the shock-compressed clouds (Uchiyama et al. 2010) (see also Section 2). The study of middle-aged SNRs is therefore crucial for understanding the CR acceleration at modest shock speeds (at which the bulk of GeV CR are accelerated) and the importance of the re-acceleration mechanism.

A prototypical middle-aged SNR is the Cygnus Loop. It is about 21 kyr old at a distance of 735 pc that was derived from Gaia parallax measurements of several stars (Fesen et al. 2018). It is slightly aspherical, with minor and major axes of 37 and 47 pc, E-W and N-S, respectively. Its large size ($\sim 3^\circ$) and angular offset from the Galactic plane ($b \sim -8.5^\circ$) ensured that this remnant has been widely studied from radio (Loru et al. 2021; Sun et al. 2006; Uyanıker et al. 2004), infrared (Koo et al. 2016; Sankrit et al. 2014), optical (Fesen et al. 2018; Katsuda et al. 2016), UV (Kim et al. 2014; Blair et al. 2002), X-ray (Oakley et al. 2013; Katsuda et al. 2011) and γ-ray (Acero et al. 2016; Katagiri et al. 2011). The SNR has an approximate shell morphology, with a prominent limb in the north-east region, a blow-out in the south and several filaments in the north-central region. Several studies (Uchida et al. 2009; Levenson et al. 1998) and hydrodynamical simulations (Fang et al. 2017) have shown that the Cygnus Loop's properties and morphology are consistent with a scenario of a Supernova (SN) explosion taking place in a wind-blown cavity created by the progenitor star. However, very recently, Fesen et al. (2018) have proposed that the Cygnus Loop evolved in a low-density region with discrete interstellar clouds in its vicinity: a dense molecular cloud to its west and north-west and smaller clouds in the east and north-east regions.

A previous analysis of the Cygnus Loop region in the γ-ray band was performed by Katagiri et al. (2011), who modeled it with a ring with inner/outer radii of $0.7^\circ \pm 0.1^\circ$

and $1.6° \pm 0.1°$. They described its emission with a Log Parabola (LP) spectrum:

$$\frac{dN}{dE} = N_0 \left(\frac{E}{E_b}\right)^{-(\alpha+\beta\log(E/E_b))} \tag{5.1}$$

In this chapter I analyze ~ 11 years of *Fermi*-LAT data. This represents an improvement of a factor 5 with respect to the previous study by Katagiri et al. (2011), providing unprecedented sensitivity to study both spatial and spectral features of the γ-ray emission from the Cygnus Loop.

In Section 5.2, I briefly describe the observations and data reduction. The morphological and spectral analysis is reported in Section 5.3. The origin of the γ-ray emission is discussed in Section 5.4.

5.2 Observations and data reduction

The primary goal is to model the γ-ray emission from the Cygnus Loop. To this end, I correlate the γ-ray data with templates from other wavelengths, as a tool to separate the different physical processes at work in this environment.

5.2.1 Gamma-ray band

The LAT is the main instrument on board the *Fermi* satellite. It is a pair-conversion instrument sensitive to γ-ray in the energy range from 30 MeV to more than 1 TeV (Atwood et al. 2009). For this analysis, I used more than 11 years of *Fermi*-LAT data (form August 4, 2008, to October 28, 2019). The Region of Interestf (ROI) is $10° \times 10°$ aligned with Galactic coordinates, with the central position shifted from the center of the Cygnus Loop (R.A.=20h50m51, Dec=30° 34′ 06″ , equinox J2000.0), by $\sim 2°$ off the Galactic Plane (so that it is at $b \sim -10.5°$). This is done in order to be less affected by the diffuse emission from the Galactic plane. To analyze the γ-ray data, I used version 1.2.1 of the `Fermitools` and version 0.18 of the `Fermipy` package, publicly available from the Fermi Science Support Center (FSSC)[1].

[1]The Science Tools package and supporting documents are distributed by the Fermi Science Support Center and can be accessed at http://fermi.gsfc.nasa.gov/ssc/data/analysis/software/

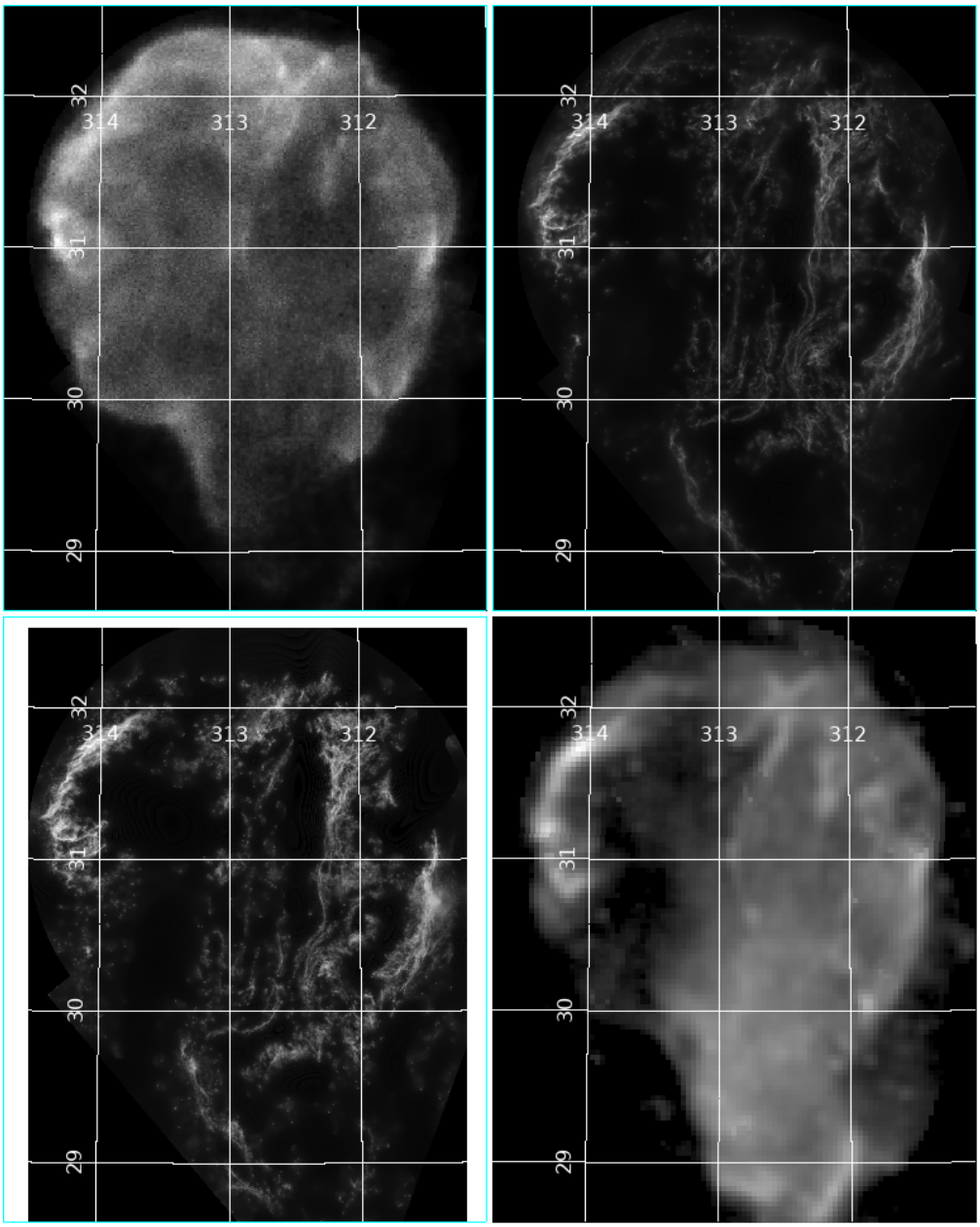

Figure 5.1: Templates used to fit the γ-ray data, in celestial coordinates. Top left, X-rays (ROSAT, 5.2.2); top right, UV (GALEX NUV, 5.2.3); bottom left, optical (DSS2 red, 5.2.4); bottom right, radio (11 cm, Effelsberg, 5.2.5). All maps are aligned and shown in square root scaling from 0 to the maximum.

I selected γ-ray in the $0.1 - 100$ GeV energy range. Because my analysis relies on morphology I selected events with good Point Spread Function (PSF), *i.e.* good angular resolution: below 316 MeV I selected data with `Event Type` PSF2 and PSF3; between 316 MeV and 1 GeV I added PSF1 events; above 1 GeV I used all events including the PSF0 `Event Type`. The bright γ-ray emission from the Earth's atmosphere was eliminated by selecting events within $90°$ from the local zenith below 316 MeV and within $105°$ of the zenith above 316 MeV. I also applied a Good Time Interval (GTI) selection on the data using quality flag `DATA_QUAL > 1` and the instrument in science configuration (`LAT_CONFIG == 1`). I used the `CLEAN` event class selection, and version `P8R3_CLEAN_V2` of the instrument response function.

To describe the γ-ray emission around the Cygnus Loop, I performed a binned likelihood analysis with pixel size set to $0.05°$, ten energy bins per decade, and keeping each `Event Type` selection separate. I included in the model all the background sources from the 4FGL catalog (Abdollahi et al. 2020a) within $13°$. I used the `gll_iem_v07.fits` model to describe the Galactic diffuse emission and the tabulated model `iso_P8R3_CLEAN` to describe the isotropic emission, using the appropriate template for each `Event Type` selection. I applied energy dispersion on all model components with the only exception of the isotropic emission.

5.2.2 X-ray band

The X-ray emission is a good tracer of the shocked gas at densities < 1 cm^{-3} and temperatures of a few 10^6 K occupying most of the SNR interior. Because the Cygnus Loop is very large (hard to mosaic with the current generation of X-ray instruments) and its emission is very soft (peaking below the C edge at 284 eV) the image from the *ROSAT* survey (Aschenbach & Leahy 1999) remains the best reference. I obtained the full band image ($0.1-2.4$ keV) from SkyView[2]. I removed by eye circles of $0.1°$ radius around 10 obvious point sources in the image (only one inside the SNR, at α, δ = 312.56,+29.37 in the south breakout). I subtracted the large-scale background estimated from Sextractor (Bertin & Arnouts 1996), at a scale (defined by the BACK_SIZE parameter) set to $1.5°$. Then I applied adaptive smoothing using the XMM SAS task *asmooth* so that the signal to noise in each pixel is at least 5 σ (the inner areas have only a few counts per

[2] https://skyview.gsfc.nasa.gov

pixel). The point sources that I removed were filled by this procedure because I entered the mask as an exposure map. None of those steps is critical to the resulting γ-ray fit. Finally I set to 0 signal outside a circle of 1.5° radius, with rectangular extensions covering the south outbreak. The 68% angular resolution of the resulting image shown on Figure 5.1 (top left) is approximately 0.03° (estimated from the point sources), much better than the γ-ray one.

In the soft X-ray band, interstellar absorption along the line of sight can significantly reduce the observed X-ray flux. This can affect the morphology of the observed emission if absorption varies strongly across the large angular extent of this source. In order to estimate these variations across the SNR region, I used data from the atomic hydrogen survey HI4PI (HI4PI Collaboration et al. 2016). To focus on the foreground gas, I have integrated the velocities from 0 to 10 km s^{-1} in order to match the absorption value measured in X-rays in the interior of the remnant ($N_H \sim 3 \times 10^{20}$ cm^{-2}, Uchida et al. 2009). In this velocity integrated N_H map, I observe a gradient of material towards the Galactic plane from 3×10^{20} cm^{-2} to 6×10^{20} cm^{-2} from the eastern to the western bright edges of the SNR.

Assuming an average plasma temperature of 0.3 keV (Katsuda et al. 2008b; Uchida et al. 2009), the *ROSAT*/PSPC effective area and using the count rate simulator WebPIMMS [3], the count rate in the $0.1 - 2.4$ keV band varies by about 20% for the aforementioned N_H values. This effect is negligible for the γ-ray study and I do not attempt to correct for absorption effects in the X-ray map.

5.2.3 Ultraviolet band

The UV emission is a good tracer of the radiative shocks developing in interstellar clouds at several particles cm^{-3} (about 10 times denser than the gas that is observed in X-rays). In order to cover the full Cygnus Loop, I started from the *GALEX* mosaic[4] kindly provided in FITS form by M. Seibert. This image was built at $3''$ resolution from the near UV images ($1771 - 2831 \mathring{A}$). The main lines from radiative shocks in this band are [C III] $\lambda 1909$, [C II] $\lambda 2326$ and [O II] $\lambda 2471$ $\mathring{A}$.

The main difficulty with the UV mosaic is that it is dominated by point sources (and

[3] https://heasarc.gsfc.nasa.gov/cgi-bin/Tools/w3pimms/w3pimms.pl
[4] http://www.galex.caltech.edu/media/glx2012-01r_img01.html

secondary reflections, so called "smoke rings", next to the bright ones). Therefore it cannot be used directly as a template. I applied Sextractor in two passes: a first pass with large BACK_SIZE=128 ($6'$) to detect bright sources everywhere, and a second pass (meant to detect faint sources while avoiding to remove pieces of filaments) with smaller BACK_SIZE=32 ($1.5'$) followed by a selection (based on source angular size, flags and flux/background ratio) requiring a detection compatible with a point source morphology. I generated circular regions excluding the entire regions where sources increase the background visually (radius proportional to flux to the power of 0.3), adapted a few by eye, added 80 regions around the secondary reflections, resulting in about $10,000$ excluded regions in total.

After this I rebinned the masked image and the mask into $30''$ pixels (I do not need better angular resolution to fit the γ-ray). I smoothed the image locally around the zero values in the rebinned mask (where bright stars were) and divided the smoothed image by the smoothed mask to recover a flat exposure. The last stage (large-scale background subtraction, adaptive smoothing and clipping) was the same as in 5.2.2, except BACK_SIZE was set to $32'$ because there are no large scale features in the UV image. The resulting image is shown on Figure 5.1 (top right).

5.2.4 Optical band

The optical band also traces radiative shocks. Optical line intensities are sensitive to different shock speeds and ages with respect to the ones in the UV band. Again because of the angular size of the Cygnus Loop a sky survey is better, so I used the Digital Sky Survey 2 (DSS2) images in the red band, which covers 6000 to 7000 $\mathring{A}$, including [O I] $\lambda 6300$, Hα $\lambda 6536$, [N II] $\lambda 6584$ and [S II] $\lambda 6717 - 6730$ $\mathring{A}$. I obtained the data from the STScI server[5], forcing plate XP463 in order to preserve a uniform background (no automatic jump to plate XP464). I extracted 3×4 $60 \times 60'$ images at $1''$ resolution separated by $55'$, allowing to cover the full SNR with $2.5'$ overlap between images.

The principle of source detection and exclusion was the same as in the UV, with the additional difficulty that the bright stars saturate the plates and look broader than the faint stars. I therefore used three different Sextractor settings, going deeper while using smaller BACK_SIZE and DETECT_MINAREA. The last call (for the faint sources)

[5] http://archive.stsci.edu/dss

also required that the detections look like point sources. There were on average $5,000$ excluded regions in each image. The radius of the circles was set to twice the source FWHM reported by Sextractor for the bright sources, and 1.5 FWHM for the median and faint sources. I rebinned the images to $3''$ (aligned with the UV image as much as possible) to avoid needlessly large files, built the mosaic of 3×4 original images to cover the entire Cygnus Loop then rebinned to the final $30''$ pixels. The last stages (point-source filling, large-scale background subtraction, adaptive smoothing and clipping) was the same as in 5.2.3. The resulting image is shown on Figure 5.1 (bottom left). From the γ-ray point of view, the optical image is very similar to the UV. However the brightest filaments get close to the saturation level in the DSS2 images.

5.2.5 Radio band

The radio band (synchrotron emission) traces a combination of low-energy electrons and magnetic field. In order to ensure that the large-scale signal was preserved, I used the single-dish images reported in Uyanıker et al. (2004) from the *Effelsberg* 100 m telescope at 21 and 11 cm, and Sun et al. (2006) from the *Urumqi* 25 m telescope at 6 cm. The respective half-power beam widths were $9.4'$, $4.3'$ and $9.5'$, so they are better than the γ-ray resolution, but not good enough to extract point sources self-consistently as in the other wavebands. Instead I used the NVSS catalogue (Condon et al. 1998) obtained at higher resolution with the *VLA* to select forty point sources brighter than 100 mJy and with intrinsic size less than $100''$ in the field of view. I excluded circles of radius 0.1° at 11 cm (0.15° at 6 and 21 cm), scaled by $F_{\rm Jy}^{0.3}$ as I did in the UV ($F_{\rm Jy}$ is the source flux in Jy). I refilled them by smoothing as in 5.2.3. Similarly to the X-rays, the Cygnus Loop is bright enough in the radio that none of those steps is critical to the resulting γ-ray fit. The map with the best angular resolution (at 11 cm) is shown on Figure 5.1 (bottom right).

5.3 Analysis

There are three sources in the 4FGL catalog around the Cygnus Loop position: the extended ring (4FGL J2051.0+3049e) introduced by Katagiri et al. (2011), a point source in the eastern part of the ring (4FGL J2056.4+3142) and a point source in the

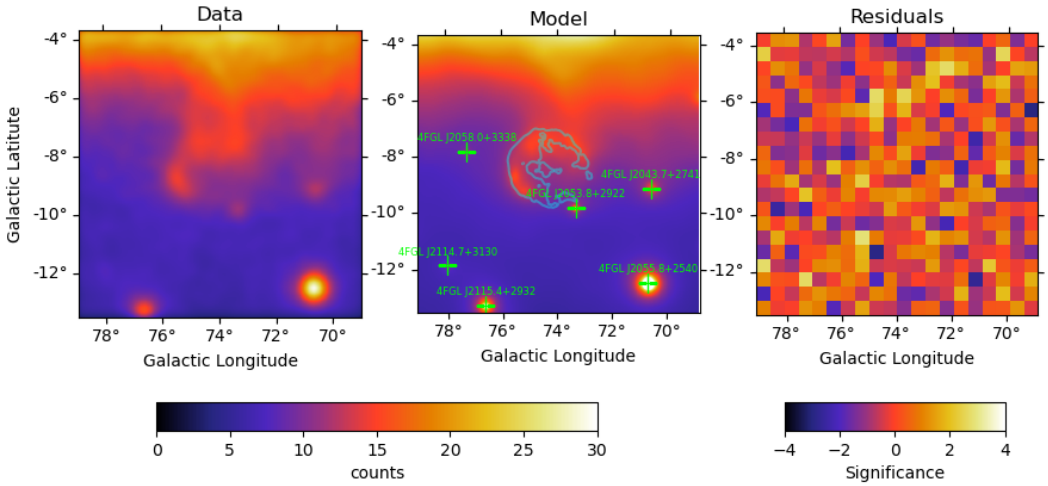

Figure 5.2: *Left:* Count map in a $10^\circ \times 10^\circ$ (pixel size of 0.05°) region around the Cygnus Loop (smoothed with a Gaussian kernel of 0.2°) from 0.1 to 100 GeV. *Center:* Count map expected from the X-ray+UV model (same spatial binning as the left map). Green crosses indicate the positions of γ-ray sources listed in the 4FGL catalogue. The cyan line is the contour (10% of the maximum) of the *ROSAT* X-ray template of the Cygnus Loop (see 5.2.2). *Right:* Residual count map from the X-ray+UV template model (pixel size of 0.5°).

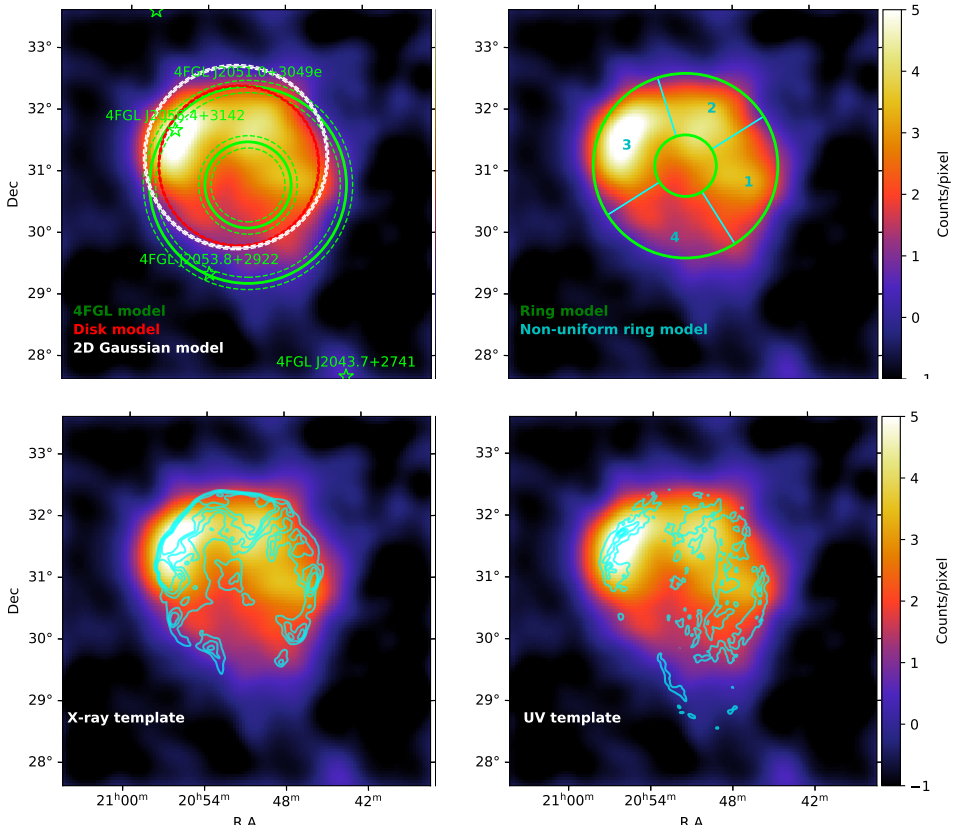

Figure 5.3: Residual count map in a $6° \times 6°$ (pixel size of $0.05°$) region around the Cygnus Loop (smoothed with a Gaussian kernel of $0.2°$) obtained from 0.1 to 100 GeV without the Cygnus Loop included in the model (*null-hypothesis*), with different templates overlaid. *Top Left:* Best-fit disk and Gaussian models represented in red and white, respectively. The 4FGL sources are shown in green. The ring model (4FGL J2051.0+3049e) introduced by Katagiri et al. (2011) is shown in green. *Top right:* Best-fit ring model (green). The blue lines define the 4 sections used for the morphology analysis. *Bottom left:* Contours of the *ROSAT* X-ray (cyan, see 5.2.2) template. The templates were smoothed with a Gaussian Kernel of $\sigma = 0.2°$ to make the contours more regular. Contours for the X-ray template are at $30\%, 20\%, 10\%$ and 1% of the maximum. *Bottom right:* Contours for the *GALEX* UV (cyan, see 5.2.3) template are at $40\%, 25\%, 15\%$ and 2% of the maximum.

southern part of the ring (4FGL J2053.8+2922), all described by LP spectra (see left and middle panel in Figure 5.2). While the former two sources are associated with the Cygnus Loop, the latter is associated to an Active Galactic Nuclei (AGN) (RX J2053.8+2923, Brinkmann et al. 1997) in the 4FGL catalog, with no spectral variations in the time period analyzed. I performed the morphological analysis from 0.1 GeV to 100 GeV, with the free parameters in the model being the normalization of the sources located closer than 6° from the ROI center, of the Galactic and isotropic diffuse emissions and the spectral parameters of the Cygnus Loop and 4FGL J2053.8+2922. The nearest bright sources are PSR J2028+3332 and PSR J2055+2539, stable sources further than 5° from the ROI center.

5.3.1 Geometrical models

To perform the morphological analysis, I consider the model with no emission from the Cygnus Loop (I removed sources 4FGL J2051.0+3049e and 4FGL J2056.4+3142) as my *null-hypothesis*, which has a maximum likelihood $\mathcal{L}_0$. Figure 5.3 shows the excess map of a $6^\circ \times 6^\circ$ region, with a pixel size of 0.05° and centred on the Cygnus Loop position, obtained using my *null-hypothesis* as a model. Then, I test alternative models by adding spatial templates and/or by varying the parameters of the models, and I compute the corresponding maximum likelihood $\mathcal{L}_{mod}$. The fit improvement is quantified by the test statistic (Mattox et al. 1996)

$$TS = 2 \times (\log \mathcal{L}_{mod} - \log \mathcal{L}_0) \tag{5.2}$$

which, in the absence of a real source, follows a χ^2 distribution with k degrees of freedom corresponding to the additional free parameters between the models and the *null-hypothesis*.

I tested several spatial models to describe the emission from the Cygnus Loop, assuming a LP spectrum with all parameters free. First, I started with three geometrical models: a uniform disk, a 2D symmetric Gaussian and a uniform ring. I report the best-fit positions and extensions obtained, with the associated TS values for these models, in Table 5.1. The Akaike information criterion (AIC; Akaike 1974) is adopted to compare the different geometrical models, where the AIC values are computed as

Table 5.1: Best-Fit Spatial Properties and Test Statistic (TS) of Cygnus Loop for different Morphological Models compared with the *null-hypothesis* of no γ-ray emission associated with the Cygnus Loop ($0.1 - -100$ GeV). Spectral Model: LP.

Model	$\mathrm{RA}_{J2000}(^\circ)$	$\mathrm{DEC}_{J2000}(^\circ)$	$r - \sigma(^\circ)$	Test Statistic [a]	Additional DoF
Null hypothesis [b]				0	0
Uniform Disk	312.905 ± 0.016	31.130 ± 0.018	$1.300^{+0.011}_{-0.014}$	6120	6
Gaussian 2D	312.959 ± 0.022	31.269 ± 0.021	$1.483^{+0.021}_{-0.021}$	5874	6
Ring	312.905	31.130	$r_{max} = 1.50^{+0.01}_{-0.02}$, $r_{min} = 0.50^{+0.04}_{-0.07}$	6172	7
Non-uniform ring [c]	312.905	31.130	$r_{max} = 1.50$, $r_{min} = 0.50$	6442	16
X-ray ($0.1 - 2$ keV) [d]				6446	3
Optical ($1.7 - 2$ eV) [e]				6584	3
UV ($4 - 9$ eV) [f]				6650	3
Radio 21cm (1427 MHz) [g]				4986	3
Radio 11cm (2725 MHz) [g]				4878	3
Radio 6cm (4996 MHz) [h]				4750	3
X-ray + UV				6870	6

[a] $-2\log(\mathcal{L}_0/\mathcal{L})$, where $\mathcal{L}$ and $\mathcal{L}_0$ are the maximum likelihoods for the model with/without the source component, respectively.

[b] Background only (no model for the Cygnus Loop).

[c] A ring (same radius as Ring model) divided into four regions as shown in Figure 5.3 and allowing an independent normalization and spectral index for the four portions of the ring.

[d] The X-ray template is obtained by *ROSAT* (see 5.2.2).

[e] The Optical template is obtained by *DSS2* (see 5.2.4).

[f] The UV template is obtained by *GALEX* (see 5.2.3).

[g] Template by the *Effelsberg 100 m Radio Telescope* (see 5.2.5).

[h] Template by the *Urumqi 25 m Telescope* (see 5.2.5).

$AIC = 2k - 2\log\mathcal{L}$ (k is the number of estimated free parameters in the model). The result in Table 5.1 shows an obvious improvement for using the disk model rather than the Gaussian model ($\Delta AIC = AIC_{Gauss} - AIC_{Disk} = 246$). To explore the uniform ring template, I defined a 2D ring with morphology defined by a FITS template. I kept the ring centered at the best-fit position of the disk model and I varied inner and outer radii and evaluated the maximum likelihood values. I explored values of inner radius in the range of $r_{min} = 0.2^\circ - 0.6^\circ$ and of the outer radius $r_{max} = 1.5^\circ - 1.7^\circ$. In Table 5.1 I report the best model. The ΔAIC value for the ring with respect to the disk shape is 50, so the ring is clearly favored.

Figure 5.3 shows that the emission along the remnant is not very uniform, therefore I also looked for a possible spectral variation in the γ-ray emission along the Cygnus Loop. To this end, I divided the best-fit ring into four sections as shown in the top left panel in Figure 5.3. I independently fit the four sections leaving as free parameters the normalizations, α and β parameters. This leads to a higher TS value than the uniform ring, as the non-uniform ring can handle the differences along the remnant better. The results, shown in Table 5.2, indicate that there are no significant differences in the spectral indices along the Cygnus Loop. The γ-ray emission is fainter in the southern region (region 4) and brighter in the North-East (region 3).

5.3.2 Correlation with other wavelengths

I further investigated the Cygnus Loop morphology by evaluating the correlation with emission at other wavelengths: X-rays, UV (see bottom panels in Figure 5.3) and radio continuum. I used the images at these wavelengths as spatial templates to fit the γ-ray emission, assuming a LP spectrum. The TS values for the X-ray, optical and UV templates show a large improvement compared to all the other models. The UV template is best, but even the X-ray template is favored compared to the non-uniform ring (ΔAIC = 38) because it has many fewer degrees of freedom. The optical template is somewhat worse than the UV, but this is probably due to the saturation of the DSS2 images (5.2.4). On the contrary, the radio templates have lower TS values because of their bright emission in the southern region of the remnant, where the γ-ray emission is fainter. This difference between the radio emission and the other wavebands had been explained by the existence of a separate SNR interacting with the Cygnus

Table 5.2: TS and best-fit spectral indices for the four sections of the ring as shown in Figure 5.3 using a LP model. The normalization is computed at 837 MeV, following Katagiri et al. (2011)

Region	TS	α	β	Normalization (10^{-12} MeV^{-1} cm^{-2} s^{-1})
1	916	2.10 ± 0.04	0.13 ± 0.02	5.74 ± 0.26
2	586	2.01 ± 0.05	0.20 ± 0.01	4.23 ± 0.22
3	2194	2.07 ± 0.03	0.17 ± 0.06	8.50 ± 0.22
4	206	1.91 ± 0.08	0.15 ± 0.03	2.21 ± 0.22

Loop (Uyanıker et al. 2002), although recent multi-wavelength analysis (Fesen et al. 2018) makes this interpretation controversial.

The X-ray pattern follows the rims of the remnant and its correlation with the γ-ray emission seems to suggest that the high-energy particles may be located in the forward shock region. The UV template instead traces the radiative shocks in the remnant and its filamentary structures are correlated with the central and west regions of the remnant. The residual map after fitting the X-ray (UV) template shows significant emission correlated with the UV (X-ray) template. I, therefore, tested a two-component model, including both the X-ray and UV maps, whose best-fit parameters are listed in Table 5.1. The sharp increase in the TS parameter (by ~ 200; see Table 5.1), together with the residuals within 4σ (see right panel of Figure 5.2) indicates that the X-ray+UV templates fit the γ-ray morphology adequately. The residuals are normally distributed around a mean value of 0.05σ with a standard deviation of 1.106σ, implying a systematic contribution of 0.47σ, less than the statistical one.

5.3.3 Spectral Analysis

Using the UV template as morphological model for the remnant I investigated the spectral shape of the Cygnus Loop as a whole. I compared the likelihood values of the spectral fit for a power law with other spectral functions over the entire energy range considered. TS values and best-fit parameters are reported in Table 5.3. A curved spectrum is clearly preferred over a power-law spectrum. The exponentially cut-off power law is not a good model (the spectrum does not fall off exponentially toward high energies). A simple symmetric log-normal (LP) model fits the data quite well. The

Table 5.3: Test Statistic and parameters for various Spectral Models ($0.1 - -100$ GeV). Using as Spatial Model the UV map. The reference energy E_0 is set to 1 GeV for all the models.

Model	TS [a]	Spectral Model	Spectral Parameters	Energy flux ($0.1 - 100$ GeV) (10^{-5} MeV cm^{-2} s^{-1})
Power Law (PL)	0	E^{-p}	$p = 2.14 \pm 0.01$	7.15 ± 0.12
Exp. cut-off PL	324	$\left(\frac{E}{E_0}\right)^{-\gamma} \exp -\left(\frac{E}{E_{cut}}\right)$	$\gamma = 1.77 \pm 0.03$ $E_{cut} = 4.1 \pm 0.4$ GeV	5.31 ± 0.10
LogParabola	418	$\left(\frac{E}{E_0}\right)^{-\alpha-\beta\log(E/E_0)}$	$\alpha = 2.134 \pm 0.016$ $\beta = 0.212 \pm 0.013$	5.44 ± 0.10
PLSuperExpCutoff4	428	$\left(\frac{E}{E_0}\right)^{-\gamma_0+d/b} \exp\left[\frac{d}{b^2}\left(1-\left(\frac{E}{E_0}\right)^{b}\right)\right]$	$\gamma_0 = 2.140 \pm 0.024$ $d = 0.350 \pm 0.023$ $b = -0.40 \pm 0.12$	5.62 ± 0.12
Smoothly broken PL	430	$\left(\frac{E}{E_0}\right)^{-p_1}\left[1+\left(\frac{E}{E_b}\right)^{\frac{p_2-p_1}{b}}\right]^{-b}$	$p_1 = 2.68 \pm 0.07$ $p_2 = 1.12 \pm 0.12$ $E_b = 620 \pm 130$ MeV $b = 0.99 \pm 0.04$	5.82 ± 0.11

[a] $-2\ln(\mathcal{L}_0/\mathcal{L})$, where $\mathcal{L}$ and $\mathcal{L}_0$ are the maximum likelihood values for the model under consideration and the power-law model, respectively.

Table 5.4: Best-fit spectral parameters for the X-ray+UV model using a LogParabola model.

Region	α	β	Energy flux (0.1 - 100 GeV) (10^{-5} MeV cm^{-2} s^{-1})
X-ray	2.17 ± 0.07	0.37 ± 0.04	2.07 ± 0.16
UV	1.97 ± 0.04	0.14 ± 0.02	3.48 ± 0.19

PLSuperExpCutoff4 model in the Fermi Tools has superexponential index $b < 0$ (*i.e.*, with a subexponential fall-off toward low energies and power-law decrease toward high energies). It increases TS by 10, corresponding to a little more than 3σ improvement with respect to LP (which corresponds to $b = 0$, with $d = 2\beta$; see parameter definitions in Table 5.3). The smoothly broken power-law model (with one more parameter) does not improve the fit. Considering the three possible spectral models, the integrated energy flux of the Cygnus Loop, using the UV template, in the energy band of $0.1 - -100$ GeV is $5.6 \pm 0.2 \times 10^{-5}$ MeV cm^{-2} s^{-1}.

I extracted the Spectral Energy Distribution (SED) in twelve logarithmically spaced energy bands from 0.1 to 100 GeV. In each bin, the photon index of the source was fixed to 2 and I imposed a TS threshold of 4 below which I calculate an upper limit. The upper panel of Figure 5.4 shows the resulting SED.

I then performed a spectral analysis using the best morphological template: the X-ray+UV template. Statistics are not enough to constrain models with more than two shape parameters such as PLSuperExpCutoff4, but I explored different combinations of power law and LogParabola functions for each one of the two components (the X-ray and UV template). Using a LP spectral function for both the X-ray and UV templates I obtained the highest TS value. It is increased by 61, compared to fixing the shape parameters to the best PLSuperExpCutoff4 of Table 5.3 and fitting only normalizations. This implies that the spectral shapes of the X-ray and the UV components differ significantly. The results are summarized in Table 5.4. I then extracted the SED of both components as explained previously. The lower panel of Figure 5.4 shows the resulting SEDs.

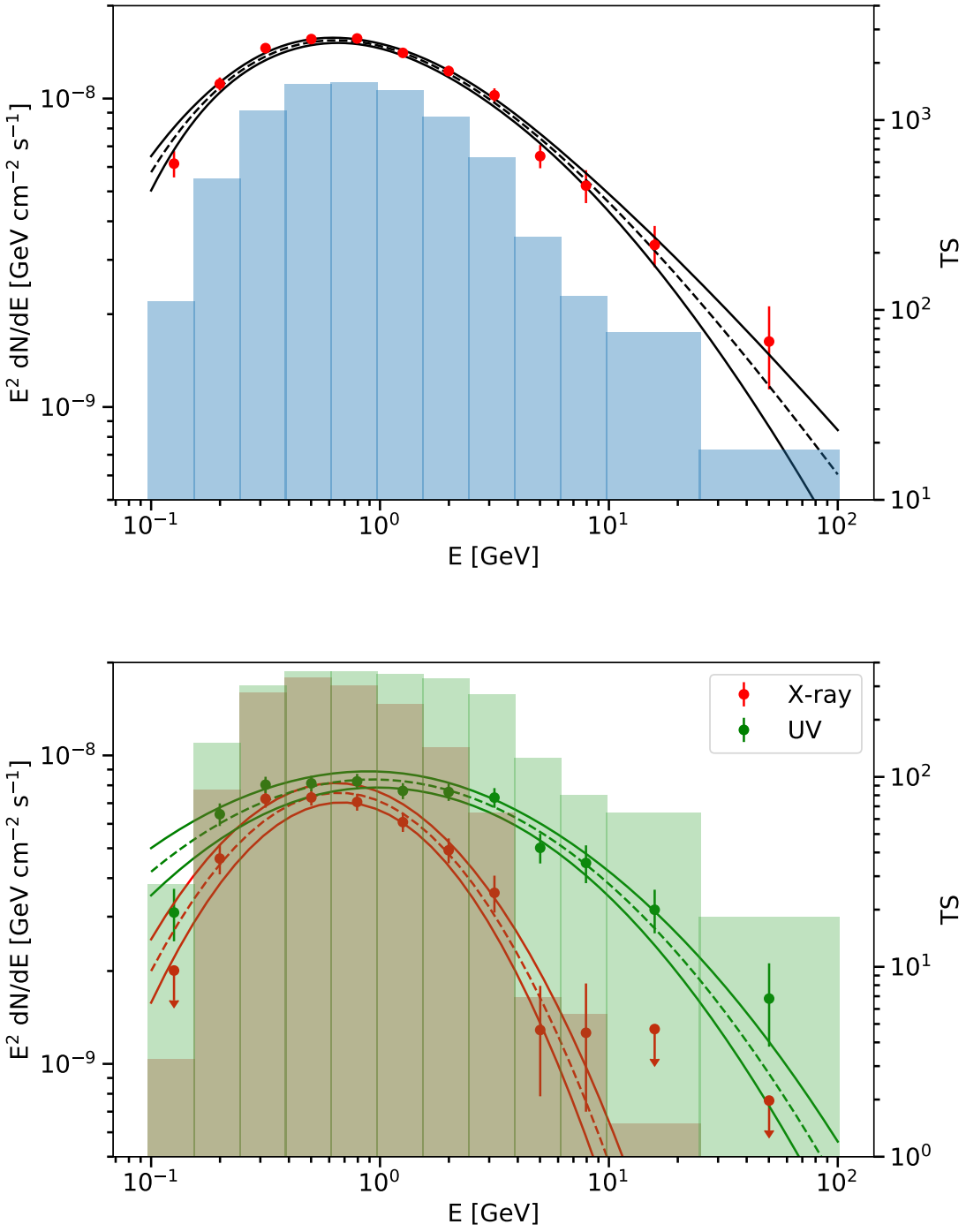

Figure 5.4: Spectral energy distribution of the γ-ray emission measured with the LAT for the Cygnus Loop. The filled histograms show the TS values in each energy bin. Vertical bars show 1σ statistical errors. Where the detection is not significant (TS < 4), I show upper limits at the 95% confidence level. *Upper panel:* SED extracted using the UV template. The PLSuperExpCutoff4 best-fit spectrum for the global γ-ray data (Table 5.3) is plotted as the black dashed line, and its upper and lower 1σ bounds as the black solid lines. *Lower panel:* Red (green) points are LAT flux points using the X-ray (UV) maps as spatial templates together. The lines are the best-fit LogParabola models (Table 5.4).

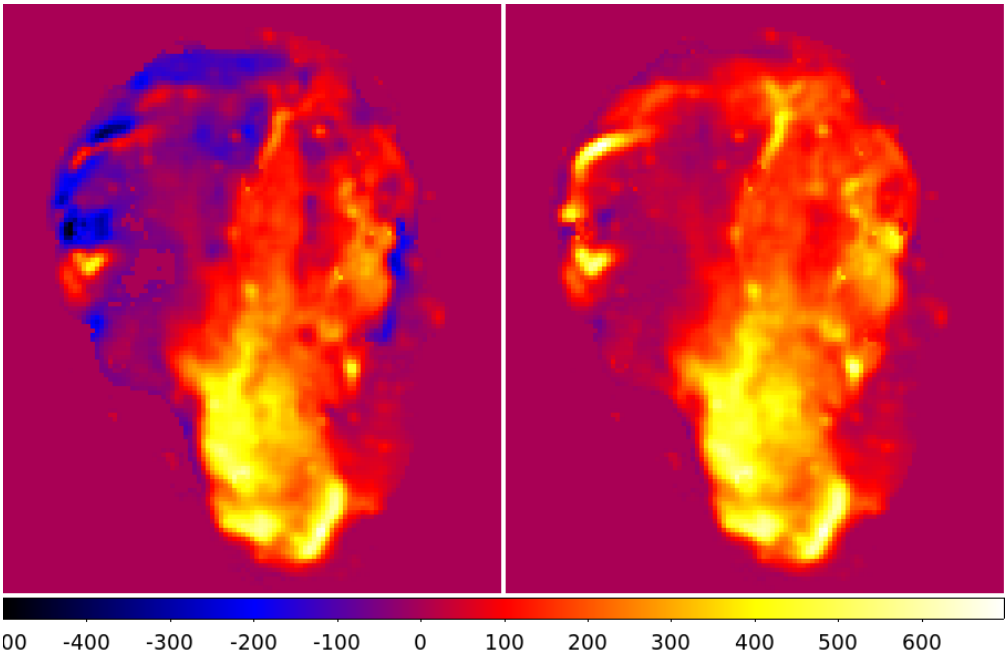

Figure 5.5: Residuals after fitting the 11 cm Effelsberg map with a combination of the UV and X-ray templates. Left, standard χ^2 fit resulting in deep negative residuals. Right, fit increasing the errors by a factor 10 for positive residuals, with no negative residuals but larger positive residuals.

Radio data extraction

A major difficulty when fitting the non-thermal emission of the Cygnus Loop is that the radio maps do not look like the γ-ray , X-ray or UV/optical maps (Figure 5.1). Radio maps are the only ones to show strong emission toward the South West, and indeed the radio template is by far the worst fit to the γ-ray data (Table 5.1). What I am interested in is the part of the radio emission that follows the other wavebands. More precisely, since I have shown (Table 5.1) that the γ-ray data is well fit by a combination of the UV and X-ray templates, I want to decompose the radio emission in the same way.

The first step is to convolve the UV and X-ray templates to the radio PSF (different in each band). Since the X-ray angular resolution σ_X is not negligible with respect to the radio angular resolution σ_R, this was achieved by a convolution with a Gaussian of $\sigma^2 = \sigma_R^2 - \sigma_X^2$. I primarily worked on the 11 cm map, which has the best angular resolution and signal to noise among the three radio maps. Fitting those convolved templates to the radio maps using a standard χ^2 fit results in deep negative residuals

in the north-east and west (Figure 5.5 left) because the fit tries to push the UV and X-ray templates as high as it can to account for the radio structure. I look instead for a decomposition that would leave only positive residuals, corresponding to the part of the radio emission that is uncorrelated with the UV and the X-rays emitting regions. In order to achieve that in a simple way I increased the errors in the χ^2 formula by a factor R wherever the residuals are positive. Figure 5.5 (right) shows that for $R = 10$ there are no negative residuals left. The fraction of the total radio flux in the residuals is 40% for $R = 1$, rising to 78% for $R = 10$. The most likely reason for this is that a large fraction of the radio emission arises in even more tenuous gas than the X-rays, mostly in the South West. Those fractions are very similar at 21 cm and 6 cm.

I consider that the radio emission correlated with the UV or X-rays must lie between the extreme $R = 1$ and 10 (a visually reasonable solution is obtained for $R = 5$) and I use those as an error interval. For each value of R I obtain the part of the radio emission correlated with the UV and that correlated with the X-rays. At 11 cm, the fraction of the radio associated to the UV is between 19% ($R = 10$) and 34% ($R = 1$), and that associated to the X-rays is between 3% and 26%. At all wavelengths the correlation with the UV is better than with the X-rays.

5.4 Modeling the Multiwavelength emission from the Cygnus Loop

To explain the observed γ-ray spectrum of the Cygnus Loop I conducted a multi-wavelength modeling of the remnant spectrum. The analysis includes radio data from 22 up to 3×10^4 MHz (Loru et al. 2021; Uyanıker et al. 2004 and citations therein) reduced by a constant factor reflecting the fraction of radio emission at 11 cm associated with the UV and/or X-ray emission, as explained in Section 5.3.3, together with the LAT GeV spectrum from this work. I have modelled the radiative processes using the `naima` package (Zabalza 2015). In the analysis, I assumed a distance to the SNR of 735 pc (Fesen et al. 2018) and, assuming a Sedov phase, a kinetic explosion energy of $E_{\rm SN} = 0.7 \times 10^{51}$ erg and an age of $t_{\rm age} \sim 21$ kyr.

I considered the contribution to the γ-ray spectrum from π^0-decay produced by the interactions of protons with ambient hydrogen, together with contribution from

Bremsstrahlung radiation and Inverse Compton (IC) scattering by accelerated electrons, which also contribute to the radio through synchrotron emission. To take into account the presence of He in the spectrum of accelerated particles, which has a spectral shape similar to protons, I have multiplied the emissivity from π^0-decay by a constant factor of 1.3. The ISM composition of the target gas is accounted for in `naima`. Following Katagiri et al. (2011), seed photons for inverse Compton scattering of electrons include the CMB, two infrared ($T_{\rm IR} = 34, 470$ K, $U_{\rm IR} = 0.34, 0.063$ eV cm^{-3}, respectively), and two optical components ($T_{\rm opt} = 3.6 \times 10^3$, 9.9×10^3 K, $U_{\rm opt} = 0.45, 0.16$ eV cm^{-3}, respectively) in the vicinity of the Cygnus Loop. Emission from the secondary electrons are neglected because of the low density environment around the remnant.

5.4.1 Ambient parameters

The Cygnus Loop blast wave has encountered discrete clouds to the east and northeast and a large molecular cloud to its west approximately $t_{\rm c} \sim 1200$ yr ago (Raymond et al. 2020). The range of shock speeds can vary widely in these regions due to the interaction of the remnant with the environment. In my analysis I consider a cloud shock velocity $v_{\rm s} = 244$ km s^{-1} (Fesen et al. 2018) and an upstream cloud density $n_{0,\rm cl} = 1.5$ cm^{-3} (Long et al. 1992) where smooth nonradiative Balmer-dominated filaments are present. I assume a cloud shock velocity $v_{\rm s} = 130$ km s^{-1} and an upstream cloud density $n_{0,\rm cl} = 6$ cm^{-3} (Raymond et al. 2020) where the deceleration is faster, UV and optical line emission cools down and compresses the gas producing regions of radiative filaments. In between these dense clouds, the remnant expands in a low-density region (~ 0.4 cm^{-3}, Raymond et al. 2003) with a faster shock velocity (~ 350 km s^{-1}, Fesen et al. 2018; Raymond et al. 2015; Medina et al. 2014).

To compute the required physical parameters in the cooled radiative regions of the remnant, I followed the approach described in Uchiyama et al. (2010). The upstream magnetic field strength and density in the clouds are related by:

$$B_{0,\rm cl} = b\sqrt{\frac{n_{0,\rm cl}}{\rm cm^{-3}}}\ \mu G \tag{5.3}$$

where $b = v_{\rm A}/(1.84\ {\rm km\ s^{-1}})$, with $v_{\rm A}$ being the Alfvén velocity, and ranges between 0.3 and 3 (Hollenbach & McKee 1989). Raymond et al. 2020 found for the radiative regions

Table 5.5: Model Parameters for the Cygnus Loop.

Parameters	Values
SNR dynamics	
Distance[a]: D	735 pc
Radius[a]: R	18.5 pc
Age[a]: $t_{\rm age}$	21000 yr
Shock-cloud interaction[b]: $t_{\rm c}$	$\sim$ 1200 yr
Explosion Energy[a]: $E_{\rm SN}$	7×10^{50} erg
N-E region parameters (non-radiative shocks)	
Density[a]: $n_{0,\rm cl}$	1.5 cm^{-3}
Magnetic Field: $B_{0,\rm cl}$	3.0 μG
Cloud shock velocity[a]: $v_{\rm s}$	244 km s^{-1}
Cutoff energy[c]: $p_{\rm max}c$ ($\eta = 7$)	15 GeV
Break energy[c]: $p_{\rm br}c$ ($T = 10^4$ K)	62 GeV
Energy in CRs[c]: $W_{\rm tot}$	1.4×10^{49} erg
e/p ratio[c]: $K_{\rm ep}$ (at 10 GeV)	0.01
West region parameters (radiative shocks)	
Density[b]: $n_{0,\rm cl}$	6 cm^{-3}
Cooled gas density: $n_{\rm m}$	293 cm^{-3}
Magnetic Field[b]: $B_{0,\rm cl}$	6 μG
Compressed Field: $B_{\rm m}$	244 μG
Cloud shock velocity[b]: $v_{\rm s}$	130 km s^{-1}
Cutoff energy[c]: $p_{\rm max}c \times s^{1/3}$ ($\eta = 7$)	20 GeV
Break energy[c]: $p_{\rm br}c \times s^{1/3}$ ($T = 10^4$ K)	70 GeV
Filling factor[c]: f	0.013
Intercloud region	
Density[a]: n_0	0.4 cm^{-3}
Magnetic Field: B_0	2 μG
Shock velocity[a]: $v_{\rm s}$	350 km s^{-1}

[a] Taken from Fesen et al. 2018.
[b] Taken from Raymond et al. 2020.
[c] Fit to the data.

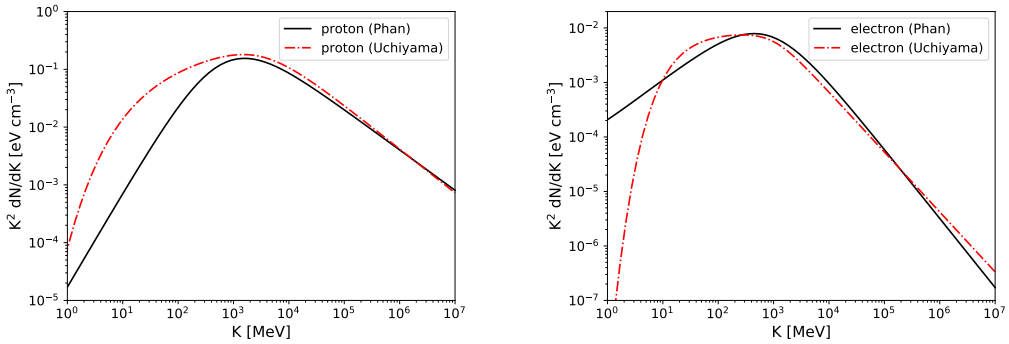

Figure 5.6: Pre-existing ambient CR spectra of protons (left) and electrons (right) as a function of particles kinetic energy. Black solid lines show the spectra from Phan et al. (2018), red dashed lines show the spectra from Uchiyama et al. (2010).

an upstream magnetic field value of 6μG that, following equation 5.3, implies $b = 2.5$. Using the same b value for the non-radiative shocks regions I found $B_{0,\rm cl} = 3\mu$G. The magnetic field just downstream (before radiative compression if any) is $B_{\rm d,cl} = r_{\rm B}\, B_{0,\rm cl}$, where the magnetic compression ratio $r_{\rm B} = \sqrt{(2r_{\rm sh}^2+1)/3}$ (Berezhko et al. 2002) assumes a turbulent field ($r_{\rm sh} = 4$ is the shock compression ratio).

The density of the cooled gas in the radiative shocks, $n_{\rm m}$, is obtained by assuming that the compression is limited by magnetic pressure. Since compression is large, only the tangential field remains in the compressed magnetic field

$$B_{\rm m} = \sqrt{2/3}\,(n_{\rm m}/n_{0,\rm cl})\,B_{0,\rm cl} \tag{5.4}$$

I note $v_{\rm s7}$ the shock velocity in 100 km s^{-1}. Equating $B_{\rm m}^2/8\pi$ with the shock ram pressure $n_{0,\rm cl}\,\mu_{\rm H}\,v_{\rm s}^2$, where $\mu_{\rm H} \sim 1.4\,m_{\rm p}$ is the mean mass per proton, one gets

$$n_{\rm m} \simeq 94\,n_{0,\rm cl}\,v_{\rm s7}\,b^{-1} \tag{5.5}$$

For the regions dominated by radiative shocks I computed values of $n_{\rm m} = 293$ cm^{-3} and $B_{\rm m} = 244\ \mu$G (consistent with those reported in Raymond et al. 2020). A summary of the parameters used can be found in Table 5.5.

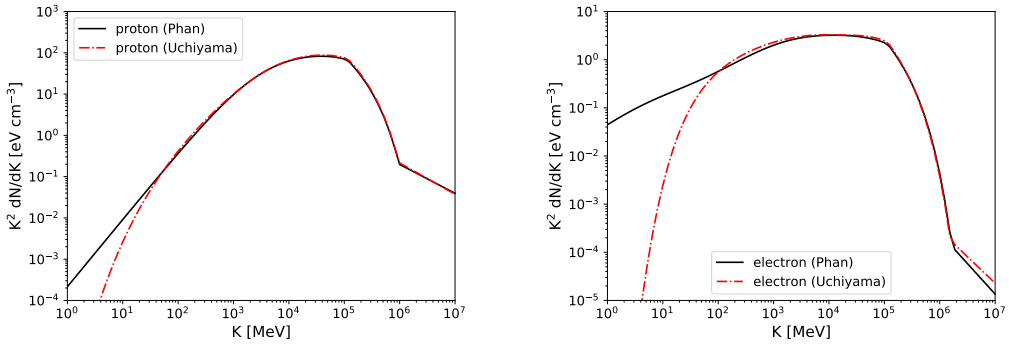

Figure 5.7: Re-accelerated and compressed protons (left) and electrons (right) vs kinetic energy with radiative compression $s = 12$, a cut-off at 100 GeV and a break at 50 GeV as reference values. Black solid lines show the spectra when starting from Phan et al. (2018), red dashed lines from Uchiyama et al. (2010).

5.4.2 Particle spectrum

Here, I discuss the CR spectrum used to model the multi-wavelength emission from the Cygnus Loop. Two mechanisms can contribute to the observed emission: the Diffusive Shock Acceleration (DSA) of thermal injected particles and re-acceleration of Galactic CRs (GCR). I first discuss the model involving Re-acceleration of Pre-existing ambient CRs (RPCR). This model was adopted by Uchiyama et al. (2010) to explain γ-ray and radio emission from W 44. At the main shock location the re-accelerated CRs number density $n_{\rm acc}(p)$ is given by:

$$n_{\rm int}(p) = (\delta+2)\,p^{-\delta}\int_0^p n_{\rm GCR}(x)x^{\delta-1}dx \tag{5.6}$$

$$n_{\rm acc}(p) = \begin{cases} \mathrm{e}^{-p/p_{\rm max}}\,n_{\rm int}(p), & p \le p_{\rm br}, \\ \frac{p_{\rm br}}{p}\,\mathrm{e}^{-p/p_{\rm max}}\,n_{\rm int}(p), & p \ge p_{\rm br}. \end{cases} \tag{5.7}$$

i.e., the steady state DSA spectrum $n_{\rm int}(p)$ (Blandford & Eichler 1987) with an exponential cutoff at $p_{\rm max}$ and a break at $p_{\rm br}$, where $\delta = \frac{r_{\rm sh}+2}{r_{\rm sh}-1}$ (in this work $\delta = 2$), $n_{\rm GCR}(p)$ is the pre-existing ambient CR density and p is the particle momentum.

I tried two parametrizations of the GCR spectrum: I used the spectra of the GCR protons and electrons from Uchiyama et al. (2010) and from Phan et al. (2018), the former derived by data from Shikaze et al. 2007 and Strong et al. 2004, the latter derived

by fitting together local CR data from the Voyager 1 probe (Cummings et al. 2016) and from the Alpha Magnetic Spectrometer (AMS, Aguilar et al. 2015). The two GCR spectra are shown in Fig. 5.6.

In order to take into account the maximum attainable energy in particles (due to energy loss and finite acceleration time) I introduced an exponential cut-off at $p_{\rm max}$. Following Uchiyama et al. (2010), the age-limited maximum momentum is

$$p_{\rm max} = 50\,(\eta/10)^{-1}\,v_{\rm s7}^{2}\,t_4\,(B_{\rm 0,cl}/10\mu G)\ {\rm GeV/c} \tag{5.8}$$

where t_4 is the remnant age (or the shock-cloud interaction age $t_{\rm c}$) in 10^4 yr. The gyro or Bohm factor η depends on the remnant age, being $\eta \sim 1$ for efficient and young SNRs like RX J1713.7−3946 (Tsuji et al. 2019; Uchiyama et al. 2007), but larger than 1 in older SNRs ($\eta = 10$ in Uchiyama et al. 2010).

I also considered a spectral steepening above $p_{\rm br}$ for both electrons and protons. The cooling break in the electrons population has been calculated by equating the synchrotron loss time (Parizot et al. 2006)

$$\tau_{\rm sync} = 1.25 \times 10^{3}\,E_{\rm TeV}^{-1}\,(B_{\rm m}/100\,\mu G)^{-2}\ {\rm yr} \tag{5.9}$$

and the remnant (or shock-cloud interaction) age. For the protons, I considered a spectral break at $p_{\rm br}$ induced by neutral-ion collisions (Malkov et al. 2011):

$$p_{\rm br} = \frac{2\,e\,B_{\rm 0,cl}\,v_{\rm A}}{c\,\nu_{\rm i-n}} \tag{5.10}$$

where $\nu_{\rm i-n} \simeq 9 \times 10^{-9} n_{\rm 0,cl}\,T_4^{0.4}\ {\rm s}^{-1}$ is the ion-neutral collision frequency and T_4 is the precursor temperature in 10^4K.

Because of the adiabatic compression in the radiative shocks, each particle gains energy as $p \rightarrow s^{1/3}p$, where $s \equiv (n_{\rm m}/n_{\rm 0,cl})/r_{\rm sh}$ ($s = 12.22$ in this work). Therefore, the number density of accelerated and compressed CR at the point where the density becomes $\sim n_{\rm m}$ is (Uchiyama et al. 2010):

$$n_{\rm ad}(p) = s^{2/3} n_{\rm acc}(s^{-1/3}p) \tag{5.11}$$

The CR proton and electron spectrum based on eq. 5.11 is shown in Figure 5.7. Fol-

lowing Uchiyama et al. (2010), I parametrized the emission volume as $V = f\,4/3\pi R^3$, where f is the filling factor of the clouds before they were crushed with respect to the entire SNR volume. The particle spectrum integrated over the SNR volume is therefore:

$$N(p) = \left(\frac{n_0}{n_{\rm m}}\right) f\,\frac{4}{3}\pi R^3\, n_{\rm ad}(p) \tag{5.12}$$

I then considered also the contribution of freshly accelerated CR at the blast wave, according to the DSA theory. The CR spectrum resulting from DSA of thermal injected particles, for both protons and electrons, is assumed to be a steady state DSA spectrum with a break and an exponential cut-off given by eqs. 5.10 and 5.8.

5.4.3 Non-radiative regions: DSA scenario

The non-radiative shocks of the Cygnus Loop are characterized by shocks fast enough to accelerate particles through the DSA mechanism. As showed in Figures 5.3 and 5.2, I described the γ-ray emission with a two-components model (X-ray+UV templates), with the X-ray emission arising from the fast non-radiative shocks. I therefore modeled the emission extracted with the X-ray component (radio data extraction described in Section 5.3.3, γ-ray data shown in lower panel of Figure 5.4) using a particle distribution arising from the DSA mechanism. In my model, on the one hand, the environmental parameters are kept fixed, on the other hand, the spectral parameters (the cut-off and break energies) depend on unknown parameters such as η and T_4.

The environmental parameters best suited to model the X-ray related emission should be those of the intercloud region ($v_{\rm s}$ = 350 km s^{-1}, n_0 = 0.4 cm^{-3}), where the shock is fast enough to generate X-ray emission. However, considering a pre-shock magnetic field of $B_0 = 2\mu$G (see eq. 5.3), eq. 5.8 yields $p_{\rm max}c > 260$ GeV ($t_4 = t_{\rm age}, \eta = 10$), incompatible with the soft γ-ray emission. I, therefore, decided to use intermediate values ($v_{\rm s} = 244$ km s^{-1}, $n_{0,\rm cl} = 1.5$ cm^{-3}, $B_{0,cl} = 3.0\mu$G) to better fit the data points. Following equations 5.8 and 5.10, the cut-off energy is $10 < p_{\rm max}c < 105$ GeV for $10 > \eta > 1$, the energy break is $33 < p_{\rm br}c < 62$ GeV for $10^5 > T > 10^4$ K. Here, the break in the electrons population can be neglected because synchrotron cooling is not relevant (see eq. 5.9).

In Figure 5.8 I present the γ-ray spectrum from the Cygnus Loop, and I demonstrate

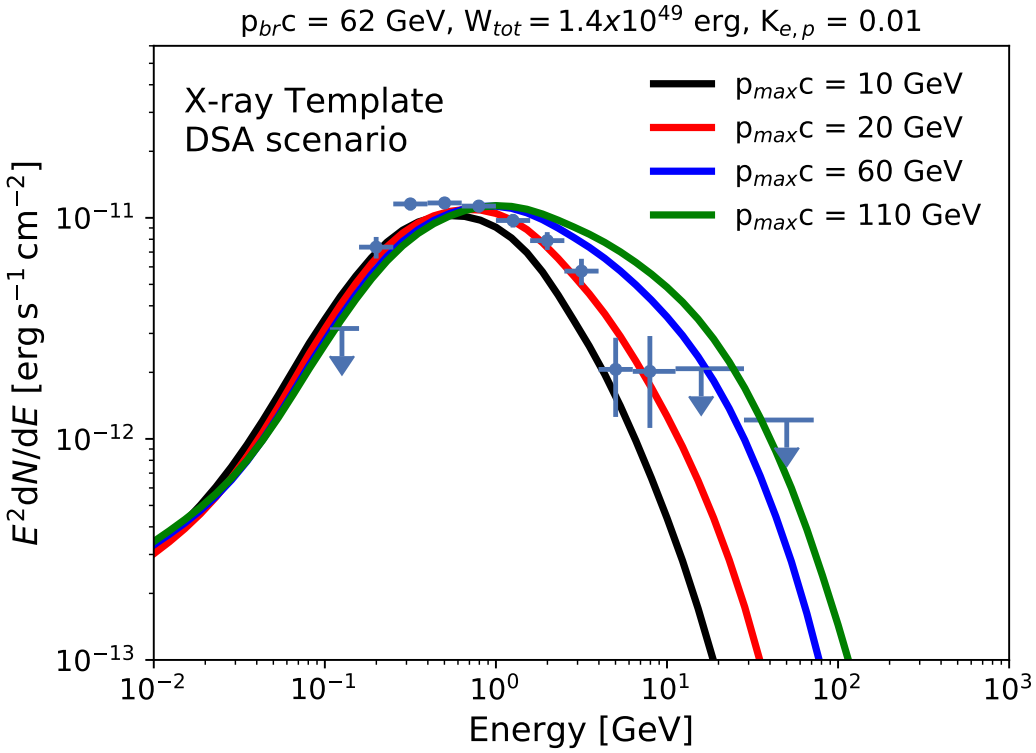

Figure 5.8: γ-ray spectrum of the Cygnus Loop extracted with the X-ray template and modeled emission in the DSA scenario. Solid lines show the total contribution of Bremsstrahlung radiation, IC and π^0-decay. The total energy ($W_{\rm tot} = 1.2 \times 10^{49}$ erg), the electron-to-proton ratio ($K_{\rm ep} = 0.01$ at 10 GeV) and the break energy ($p_{\rm br}$ = 62 GeV/c) are fixed. Different cut-off energy values are shown.

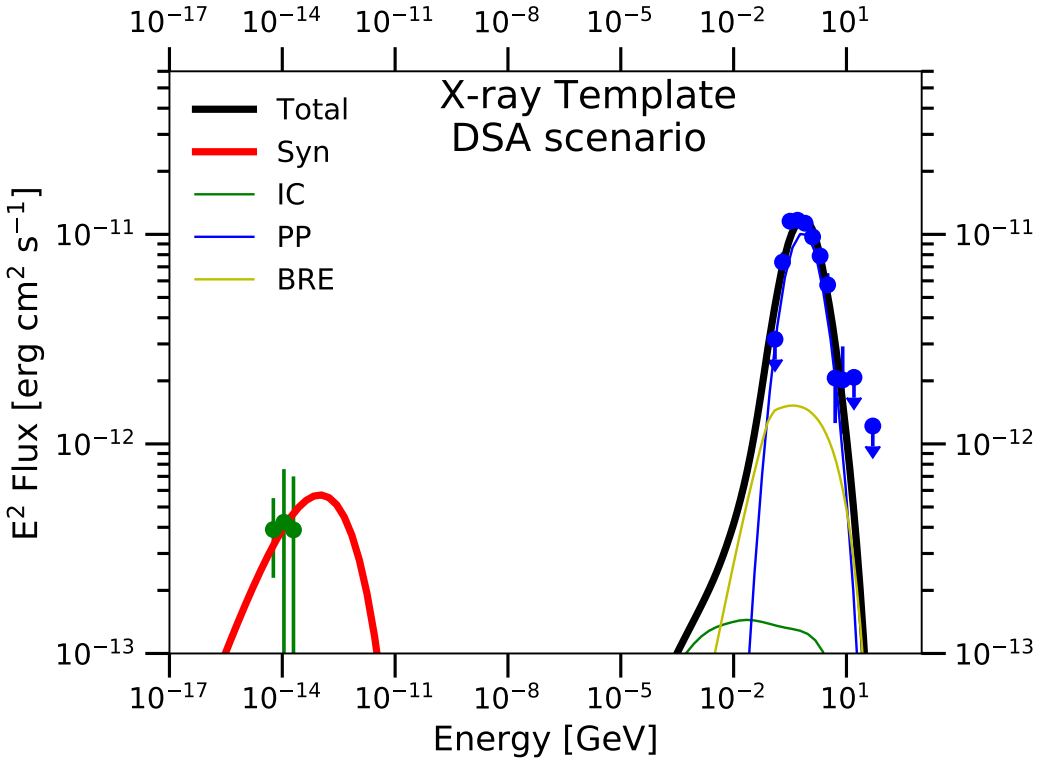

Figure 5.9: DSA scenario for the multiwavelength modeling of the emission, extracted with the X-ray template, toward the Cygnus Loop. Radio data are obtained as explained in Sect. 5.3.3. The total contribution from Bremsstrahlung, IC and π^0-decay is shown by the black solid line. The best model is obtained with a total energy $W_{\rm tot}$ of 1.2×10^{49} erg and the electron-to-proton ratio $K_{\rm ep} = 0.01$ at 10 GeV. Protons and electrons have an energy cut-off of 15 GeV and an energy break of 62 GeV.

the expected level of the γ-ray emission with varying $p_{\rm max}c$. To compute the γ-ray emission from π^0-decay, I used as the target density the upstream cloud density (1.5 cm^{-3}), as an average over the entire volume where cosmic rays are present. I kept fixed the total energy ($W_{\rm tot} = W_{\rm p} + W_{\rm He}$, where $W_{\rm p}$ and $W_{\rm He}$ are the total energy of protons and He, respectively) to $W_{\rm tot} = 1.2 \times 10^{49}$ erg (corresponding to $\sim 2\%$ of $E_{\rm SN}$) and the electron-to-proton differential spectrum ratio in kinetic energy $K_{\rm ep} = 0.01$ at 10 GeV. Figure 5.8 shows the effect of the cutoff energy on the modeled emission. Because a low value of $p_{\rm max}c$ is necessary to fit the data, $p_{\rm br}c$ does not affect the model. Hence, I decided to set $p_{\rm max}c = 15$ GeV and $p_{\rm br}c = 62$ GeV (see Table 5.5), which correspond to $\eta = 7$ and $T = 10^4$ K, in order to reproduce the γ-ray data as shown in Figure 5.9.

5.4.4 Radiative regions: Re-acceleration of pre-existing ambient CRs

In contrast to the non-radiative shocks, the radiative shocks are slower and cannot accelerate particles efficiently through the DSA mechanism. I then considered in regions dominated by radiative shocks a model involving the Re-acceleration of Pre-existing ambient CRs (RPCR). In Section 5.3 I showed that part of the γ-ray emission of the remnant is associated with the UV component (emitted by radiative shocks) in the X-ray+UV model. I then used the SED data points extracted with the UV component (radio data extraction described in Section 5.3.3, γ data shown in lower panel of Figure 5.4) to model these regions.

Again, the spectral parameters of the compressed and re-accelerated particle populations are not constrained, I therefore explored values of $14 < s^{1/3} p_{\rm max}c < 140$ GeV for $10 > \eta > 1$ and $6 < s^{1/3} p_{\rm br}c < 70$ GeV for $10^5 > T > 10^4$ K. The break due to synchrotron losses can be neglected. Another free parameter is the filling factor f of the clouds and it is obtained from the data.

I explored two different preexisting ambient CR spectra: the Galactic CR protons, and electrons from Uchiyama et al. (2010) and from Phan et al. (2018). By exploring different values of $p_{\rm max}$ and $p_{\rm br}$ for both preexisting CR spectra, I found that the differences between the two reaccelerated particle populations are minimal, also in terms of γ-ray emission (see Figures 5.6, 5.7 and 5.10). I therefore decided to use preexisting CRs from Phan et al. (2018), obtained from the more recent Voyager 1 (Cummings et al. 2016) and AMS-02 (Aguilar et al. 2015) data. In Figure 5.10, as in Figure 5.8, I present

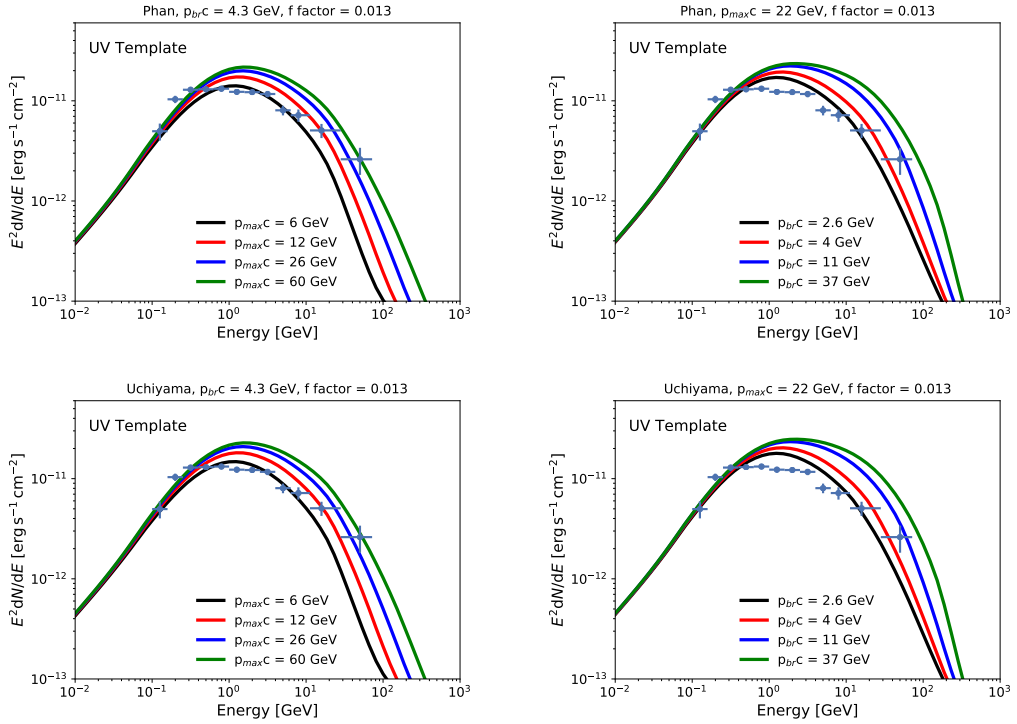

Figure 5.10: γ-ray spectrum of the Cygnus Loop extracted with the UV template and modeled emission in the RPCR scenario (eq. 5.12). Solid lines show the total contribution of Bremsstrahlung radiation, IC and π^0-decay. *Upper panels:* pre-existing CR from Phan et al. (2018). On the right (left) different cut-off (break) energy values at $p_{\rm br}c = 4.3$ GeV ($p_{\rm max}c = 22$ GeV). Note that the actual cut-off/break energies in the radiative zone are $s^{1/3}p_{\rm max}c$ and $s^{1/3}p_{\rm br}c$. The filling factor f is fixed to $f = 0.013$. *Lower panels:* pre-existing CR from Uchiyama et al. (2010). The filling factor f is fixed to $f = 0.013$.

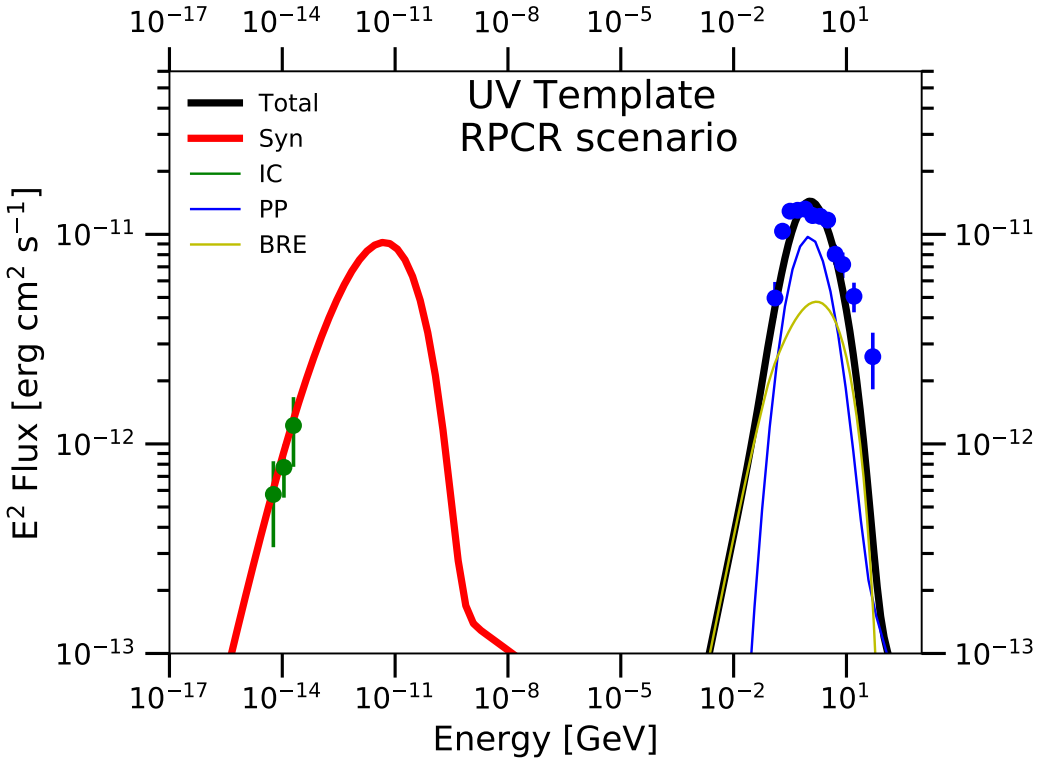

Figure 5.11: RPCR scenario for the multiwavelength modeling of the emission, extracted with the UV template, toward the Cygnus Loop. Radio data are obtained as explained in Section 5.3.3. The total contribution from Bremsstrahlung, IC, and π^0 decay is shown by the solid black line. My best model is obtained with preexisting CR populations from Phan et al. (2018) and a filling factor of $f = 0.013$. Spectral parameters for protons and electrons are $s^{1/3}p_{\rm max}c = 20$ GeV and $s^{1/3}p_{\rm br}c = 70$ GeV.

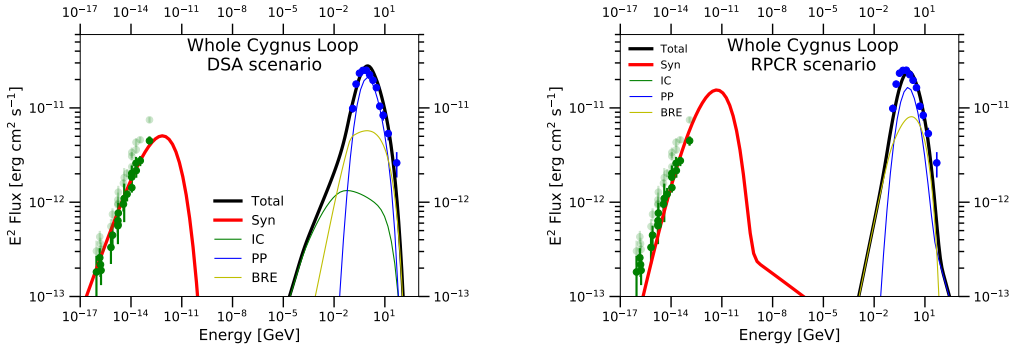

Figure 5.12: Radio and γ-ray emission from the entire Cygnus Loop. Radio data points (transparent green) from Uyanıker et al. (2004) and Loru et al. (2021) were scaled by a constant factor (dark green) to remove the contribution from the southern region (see Section 5.3.3). The total contribution from Bremsstrahlung, IC, and π^0 decay is shown by the solid black line. *Upper panel:* DSA scenario, adopting values of $p_{\rm max}c = 40$ GeV, $p_{\rm br}c = 62$ GeV, $W_{\rm tot} = 2.1 \times 10^{49}$ erg, and $K_{\rm ep} = 0.025$ for protons and electrons. *Lower panel:* RPCR scenario, adopting preexisting CR populations from Phan et al. (2018), $s^{1/3}p_{\rm max}c = 20$ GeV, $s^{1/3}p_{\rm br}c = 70$ GeV, and a filling factor $f \sim 0.02$.

the expected level of the γ-ray emission with varying $p_{\rm max}c$ and $p_{\rm br}$. To describe the data, I used $s^{1/3}p_{\rm max}c = 20$ GeV (corresponding to $\eta = 7$) and $s^{1/3}p_{\rm br}c = 70$ GeV (corresponding to $T = 10^4$ K). The best filling factor is $f = 0.013$ (see Table 5.5). The resulting fit to the spectrum of the radiative regions is shown in Figure 5.11. The model is too peaked in γ-ray and fails to fit the data at energies ¿ 10 GeV.

5.4.5 Modeling the entire Cygnus Loop

I first attempted to model the emission from the entire Cygnus Loop (obtained using the UV template alone), considering either a DSA or a RPCR scenario. Assuming the same environmental parameters of the north-east region ($v_{\rm s} = 244$ km s^{-1}, $n_{0,\rm cl} = 1.5$, $B_{0,\rm cl} = 3.0\mu$G), I tried to model the multiwavelength emission in a DSA scenario. Adopting values of $p_{\rm max}c = 40$ GeV and $p_{\rm br}c = 62$ GeV for protons and electrons, together with $W_{\rm tot} = 2.1 \times 10^{49}$ erg and $K_{\rm ep} = 0.025$, the γ-ray spectrum can be well reproduced by a DSA model shown in Figure 5.12 (upper panel). Such an energy cut-off requires $\eta = 3$ (see eq. 5.8), a value smaller than the typical $\eta = 10$ found in other middle-aged SNRs (Abdollahi et al. 2020b; Devin et al. 2020, 2018; Uchiyama et al.

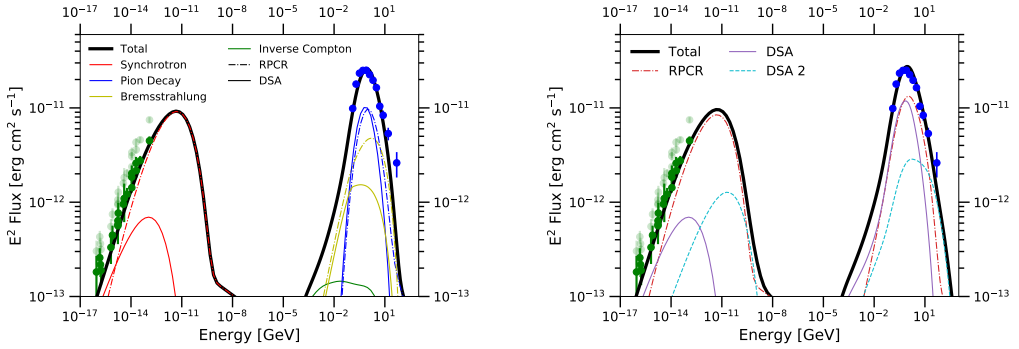

Figure 5.13: Same as Figure 5.12, but the multiwavelength model has multiple contributions. *Upper panel:* DSA scenario (solid lines) and RPCR scenario (dot-dashed lines). The total contribution from the two scenarios is shown by the solid black line. *Lower panel:* Same as the upper panel, but with contribution from the intercloud region (DSA 2).

2010).

In addition, from the morphological analysis (see Section 5.3), it clearly emerged that the γ emission is mainly correlated with the UV template and, as a consequence, with the radiative regions. Therefore the DSA mechanism is not favoured to explain the Cygnus Loop multiwavelength emission.

I also tried to model the overall spectrum assuming an RPCR scenario. I found that the best parameterization to model the overall spectrum is the same as that reported in Section 5.4.4 ($s^{1/3}p_{\rm max}c = 20$ GeV, $s^{1/3}p_{\rm br}c = 70$ GeV, and preexisting CRs from Phan et al. 2018), except for $f \sim 0.02$. However, this model presents several discrepancies with observed data, as shown in the lower panel of Figure 5.12. The synchrotron emission is not able to reproduce the radio points at lower energies, and the peak in the γ-ray emission (at ~ 2 GeV) is higher than in the LAT data. Therefore the RPCR scenario alone is not able to satisfactorily explain the emission from the entire remnant either.

From the analysis reported in Sections 5.4.3 and 5.4.4, it emerged clearly that the nonthermal emission from the radiative and nonradiative regions has a different physical origin. As a consequence, I modelled the total SNR spectrum with two contributions: an RPCR scenario caused by radiative shocks arising from the denser clouds, and a DSA contribution connected to the faster shock traveling in the lower density environment.

The upper panel of Figure 5.13 shows the corresponding emission model with the

contribution from the DSA (solid lines) and the RPCR (dot-dashed lines). The parameters are set exactly like those reported in Sections 5.4.3 and 5.4.4, for the DSA and RPCR contribution respectively (see Table 5.5). The high magnetic field in the cooled regions behind the radiative shocks makes the contribution of the RPCR scenario dominant with respect to the DSA in the radio band, while in the γ-ray band the two components have similar contributions, reflecting the γ-ray flux associated with the X-ray and UV templates (see Section 5.3.3). Overall, the modelled emission reproduces well the observed data points in the radio and γ-ray bands, unveiling the complex origin of the remnant's non-thermal emission.

The model is slightly too soft to fit the highest γ-ray energy points. A contribution at these energies could come from particles that are accelerated, through DSA, by the faster shocks in the low-density intercloud medium. This scenario (namely, DSA 2) could arise from the parameters described previously ($v_{\rm s} = 350$ km s^{-1}, $n_0 = 0.4$, and $B_0 = 2\mu$G), implying $p_{\rm max}c \sim 260$ GeV. I set the total energy of the protons and the electron-proton ratio equal to those of the DSA component (i.e., $W_{\rm tot} = 1.2 \times 10^{49}$ erg and $K_{\rm ep} = 0.01$). This new component is shown in the lower panel of Figure 5.13. By adding this new component, the model is able to explain the entire spectrum. When compared to the previous model, adding the DSA 2 component gives a TS value of 12 that is computed from the SED points.

Chapter 6

SNRs with the ASTRI Mini-Array

In the previous chapter, I showed the peculiar case of Cygnus Loop, a HE source with different acceleration mechanisms taking place, where sub-TeV particles emit MeV-GeV γ-ray radiation. However, as shown in Section 2, some SNRs are also VHE sources emitting in the TeV band and accelerating particles to the highest energies. New facilities will be devoted to the study of this energy band and before their realization it has become fundamental to individuated the most relevant targets.

In this chapter, I summarises the activities I carried out as a member of the ASTRI collaboration. In particular, I will highlight the contribution of the ASTRI Mini-Array to the observation and analysis of SNRs at the VHE.

6.1 Introduction

As mention in Section 2 the study of γ-ray radiation is of great importance to investigate several of the hottest topics in physics and astrophysics. To this end, a new generation of ground-based γ-ray detectors will widen our knowledge in this field. Among the upcoming facilities, the first to be built will be the ASTRI Mini-Array (see Section 3.2.1). In this chapter, I will present may study on best SNRs candidates which can potentially be primary targets for the ASTRI Mini-Array. The expected scientific performances of the ASTRI Mini-Array for these SNRs have been investigated through simulations.

I used CTOOLS v.1.7.2 (Knödlseder et al. 2016) to generate event lists, sky maps,

spectra and to perform maximum likelihood fitting. For every source model, 100 independent realizations have been produced and then averaged to obtain the best-fitting results (Romano et al. 2018, 2020), a procedure used in several CTA publications (Chernyakova et al. 2019; Lamastra et al. 2019). In the spectral fit, the background is treated using the IRF model, whereas I did not adopt any model for the diffuse γ-ray emission.

6.2 SNRs of interest for the ASTRI Mini-Array

The ASTRI collaboration plans to start the preparation of the observation site starting at the end 2022, commissioning and preliminary observations will begin in 2024, while the whole ASTRI Mini-Array lifetime will be of eight years. The first four years will be devoted to specific science topics, with the aim to provide robust answers to a few well-determined open questions. In particular, thanks to the wide field of view ($\sim 10^{\circ}$) it will be possible to simultaneously investigate multiple sources during the same pointing and to study at the same time vast Galactic regions.

One of the issue investigated by the ASTRI Mini-Array will be the acceleration of CRs in both Galactic and extra-galactic sources. In particular, PeVatron's research will be of particular relevance (see Section 2), by means of the capability of reaching energy boundaries above 100 TeV in conjunction with an excellent angular resolution. The acceleration of protons to PeV energies requires extreme physical conditions, representing a challenge for any Galactic source population, including SNRs. Very recently, LHAASO reported on the detection of photons at energies above 100 TeV and up to 1.4 PeV from 12 γ-ray sources, proving the existence of Galactic PeVatrons (Cao et al. 2021).

Among the SNRs visible from the Observatorio del Teide site (see Table 6.1), three are possible PeVatrons candidates, due to their high flux and hard spectra: the *historical* SNR Tycho (discussed in Section 2), VER J1907+062 and G106.3+2.7. Another interesting SNR would be IC 443: a probable hadronic accelerator with an unclear acceleration mechanism.

VER J1907+062 was discovered by the MILAGRO collaboration (Abdo et al. 2007) which exhibited VHE emission corresponding to $\sim 80\%$ of the Crab Nebula flux at 20 TeV and an upper limit on the intrinsic source extension of 2.6° . The VERITAS observations (about 62 hr of useful exposure) show diffuse TeV emission, whose origin

Table 6.1: List of identified TeV SNRs which were reported by MAGIC or VERITAS. Sky positions, source identifications and fluxes reported according to the TeVCat (Wakely & Horan 2008) catalogue.

Name	RA (deg)	Dec. (deg)	Flux Crab %
Supernova Remnants			
Tycho	6.34	64.14	1%
Cas A	350.85	58.81	2%
HESS J1912+101	288.00	10.10	0.1%
SNR G106.3+02.7	336.99	60.8769	5%
IC 443	94.21	22.50	3%
W 51	290.96	14.10	3%
SNR G015.4+00.1	274.02	-15.20	23%
Mixed PWN/SNR			
CTA 1	1.65	72.78	4%
3C 58	31.40	64.83	0.65%
Crab Nebula	83.633	22.0145	100%
Geminga	98.48	17.77	23%
HESS J1813-178	273.36	-17.85	6%
HESS J1825-137	276.55	-13.58	54%
HESS J1831-098	277.85	-9.90	4%
HESS J1837-069	279.51	-6.93	53%
IGR J18490-0000	282.26	-0.02	1.5%
VER J1907+062	286.91	6.32	17%
SNR G054.1+00.3	292.63	18.87	2.5%
MGRO J2019+37	305.02	36.72	67%

is not firmly established because of the complex morphology and the limited angular resolution. VER J1907+062 has been detected also by HAWC (2HWC J1908+063) up to $\sim$ 100 TeV with a relatively flat spectrum and no evidence of a cutoff (Abeysekara et al. 2020). According to Aliu et al. (2014), the emission in the northern region of VER J1907+062 has a probably hadronic origin connected to the SNR G40.5−0.5. In this scenario, protons accelerated at the shock front collide with target protons of the surrounding ISM, producing TeV photons via neutral pion decay. From the analysis of the spatial distribution of the ^{12}CO in the vicinity of the SNR G40.5−0.5, Duvidovich et al. (2020) found molecular clouds that match the eastern, southern, and western borders of the remnant and partially overlap with peaks of the TeV emission from VER J1907+062. Other possible counterparts, such as the PSR J1907+0602 cannot be exclude with the current data. Observations at VHE, with increased spatial resolution with respect to HAWC, can firmly constrain the origin of the emission from the northern region of VER J1907+062, thus assessing its PeVatron nature.

VER J2227+608 (Acciari et al. 2009a) is associated with the SNR G106.3+2.7 and is a potential target of great interest for two main reasons: it is a SNR with one of the highest TeV fluxes (5% in Crab units) and shows a hard spectrum (photon index $\Gamma = 2.29$) with no detected cut-off up to 10 TeV. The remnant G106.3+2.7 is extended and shows two compact and close-by regions: the "head" formed by the SNR shock, which also contains the bright pulsar PSR J2229+6114, powering a Pulsar Wind Nebulae (PWN), and an elongated, fainter, "tail" region, which contains VER J2227+608. It is worth noting that Milagro (Abdo et al. 2007, 2009) and, very recently, High Altitude Water Cherenkov Experiment (HAWC) (Albert et al. 2020), Tibet AS γ (Tibet ASγ Collaboration et al. 2021) and Large High Altitude Air Shower Observatory (LHAASO) (Cao et al. 2021) detected γ-rays from the remnant's region (up to $\sim$ 100 TeV in the case of HAWC, Tibet AS γ and LHAASO) although no clear association with a specific region of SNR G106.3+2.7 is possible, due to their low angular resolution. The VHE morphology can be well superimposed on the molecular gas images as traced by ^{12}CO radio maps, thus suggesting a potential hadronic origin, even if a leptonic origin is also possible (Liu et al. 2020; Yu et al. 2022). Here I show the main constraints on the spectral shape which would be obtained with an exposure of $\sim$500 hours with the ASTRI Mini-Array. These observations would firmly constrain the hadronic origin of the VER J2227+608 emission.

IC 443 (also known as G189.1 + 3.0) is a SNR located at 1.5 kpc with a $\sim 20'$ angular radius (Welsh & Sallmen 2003). The age of the SNR is still uncertain, with a possible range between $\sim$ 3 kyr (Troja et al. 2008) and $\sim$ 30 kyr (Bykov et al. 2008); recent 3D hydrodynamical simulations suggest an age of $\sim$ 8.4 kyr (Ustamujic et al. 2021). It is classified as a mixed-morphology SNR (MMSNR) (Rho & Petre 1998), i.e. a remnant with a shell-like morphology visible in the radio band and a centrally filled thermal X-ray emission. The environment around the remnant is rather complex: a dense molecular cloud in the northwest and southeast region (Cornett et al. 1977) forms a semi-toroidal structure that encloses IC 443 (Troja et al. 2006; Su et al. 2014) and an atomic cloud in the northeast (Denoyer 1978) confines the remnant. The remnant has been observed through radio (Leahy 2004; Lee et al. 2008, 2012), infrared (Su et al. 2014) and X-rays (Troja et al. 2006, 2008; Greco et al. 2018). Strong γ-ray emission is associated with the interaction of the SNR with the nearby molecular cloud at both HE (Tavani et al. 2010; Abdo et al. 2010; Ackermann et al. 2013) and VHE (Albert et al. 2007; Acciari et al. 2009b). Spectral features strictly related with the characteristic pion-bump (Ackermann et al. 2013) strongly suggests that IC 443 is a CR protons accelerator.

6.3 A PeVatron candidate: G106.3+2.7

Using the setup described in Section 3.2.1, I simulated SNR G106.3+2.7 as an extended elliptical source (*EllipticalDisk* in CTOOLS) with an angular extent of 0.27° along the major axis, 0.18° along the minor axis, an orientation angle of 22° east to north. Following Acciari et al. (2009a), I described the spectrum with a power-law with an index of 2.29. I do not consider Tibet ASγ Collaboration et al. (2021) and Cao et al. (2021) because of their higher flux observed compared to previous observations, so I made the conservative assumption assuming the lower flux spectrum seen by VERITAS (Acciari et al. 2009a). Event files were simulated with an exposure of 100, 200 and 500 hours. For each exposure, the spectral energy distribution was computed using ten logarithmically spaced energy bins between 3 TeV and 200 TeV.

6.3.1 Analysis and Results

I estimated the power-law spectral parameters for each exposure time, obtaining a photon index $\Gamma = (2.37 \pm 0.10); (2.34 \pm 0.06); (2.32 \pm 0.04)$ and differential flux $N_{3\mathrm{TeV}} = (1.2 \pm 0.2); (1.2 \pm 0.1); (1.2 \pm 0.1) \times 10^{-13}$ TeV^{-1} cm^{-2} s^{-1}, for 100, 200 and 500 hours, respectively. I found that the ASTRI Mini-Array can detect the SNR up to energies of $\sim$100 TeV with at least 500 hr of exposure. To obtain better constraints on the γ-ray emission, I combined both the 500h and 200h-exposure ASTRI Mini-Array data points with published data obtained by *Fermi* (Xin et al. 2019) and VERITAS Collaborations (Acciari et al. 2009a). In the analysis, I did not consider the Milagro, HAWC, Tibet ASγ and LHAASO (Abdo et al. 2007, 2009; Albert et al. 2020; Tibet ASγ Collaboration et al. 2021; Cao et al. 2021) points; in the case of HAWC and Milagro, because of their unclear spatial association within the SNR/pulsar region and, in the case of Tibet ASγ and LHAASO, because of the higher observed flux compared to the previous observations. Using the NAIMA package, I computed the expected γ-ray emission assuming a proton population described by a power-law with a cut-off. To evaluate the contribution of the ASTRI Mini-Array to this source analysis, I computed a confidence interval for the cut-off energy of the distribution of the protons. This gives us an indication of how the ASTRI Mini-Array would constrain the maximum energy achieve from this remnant. If we consider a model with parameters θ and δ where θ is the parameter of interest and δ is the (vector of) additional parameter(s) in the model and we denote by $\mathcal{L}(\theta, \delta)$ the likelihood function, the profile likelihood function for θ is

$$\mathcal{L}_1(\theta) = \max_{\theta} \mathcal{L}(\theta, \delta) \tag{6.1}$$

(for each value of θ, $\mathcal{L}_1(\theta)$ is the maximum of the likelihood function over the remaining parameters).

A $100(1-\alpha)\%$ confidence interval for θ is the set of all values θ_0 such that a test of the hypothesis would not be rejected at the α level of significance. The likelihood ratio test statistic (Mattox et al. 1996) of the hypothesis $\theta = \theta_0$ says that

$$2 \times (\log \mathcal{L}(\hat{\theta}, \hat{\delta}) - \log \mathcal{L}(\theta_0, \hat{\delta}_0)) = 2 \times (\log \mathcal{L}(\hat{\theta}, \hat{\delta}) - \log \mathcal{L}_1(\theta_0)) \tag{6.2}$$

where $\hat{\theta}$ and $\hat{\delta}$ are the maximum likelihood estimation's for the full model and $\hat{\delta}_0$ is

the maximum likelihood estimation of δ for the reduced model with $\theta = \theta_0$. As said in Section 5.3, equation 6.2 follows a χ^2 distribution, and the test $\theta = \theta_0$ will not be rejected at the α level of significance if and only if

$$2 \times (\log \mathcal{L}(\hat{\theta}, \hat{\delta}) - \log \mathcal{L}_1(\theta_0)) < \chi^2_{1-\alpha}(1) \tag{6.3}$$

or

$$\log \mathcal{L}_1(\theta_0) > \log \mathcal{L}(\hat{\theta}, \hat{\delta}) - \chi^2_{1-\alpha}(1)/2 \tag{6.4}$$

where $\chi^2_{1-\alpha}(1)$ is the $1-\alpha$ quantile of a χ^2 distribution with 1 degree of freedom.

I fixed the cut-off energy and considered both the power-law index and normalization as free parameters. I then produced a profile log-likelihood curve as a function of different cut-off energies, maximized over the power-law index and normalization. From the curve, I estimated the cut-off lower limit of the proton population, at different confidence levels, with and without the ASTRI Mini-Array data. With the 200h-exposure ASTRI Mini-Array data, I obtain a best fit value of the proton cut-off energy of 350 TeV, with a lower limit of 250, 180, 160 TeV at 68%, 90% and 95% confidence level respectively. These constraints improve considering an exposure time of 500 hr. In this case, with the 500h-exposure, I obtain a best fit value of the proton cut-off energy of 530 TeV, with a lower limit of 415, 340, 310 TeV at 68%, 90% and 95% confidence level respectively (results are showed in Fig. 6.1 and Fig. 6.2). Without the ASTRI Mini-Array data, the fit value of the proton cut-off energy is below 100 TeV, with a lower limit of $\sim$10 TeV at 95% confidence level. This simple analysis shows that the ASTRI Mini-Array could give a fundamental contribution to the study of particle acceleration in this SNR. The ASTRI Mini-Array will also investigate other potential interesting properties of this source, as its morphology. Thanks to its good angular resolution, the ASTRI Mini-Array will help to firmly distinguish, at energies > 10 TeV, the emission in the "head" region, where the pulsar is located, from the emission in the "tail" region, where molecular clouds are located. Another important point to be investigated would be a possible energy-dependent morphology for this source. This could explain the differences between the VERITAS and Tibet ASγ and LHAASO spectrum, being the latter steeper than the former, perhaps indicating different morphological characteristics. The ASTRI Mini-Array would help to study the possible implications of such differences.

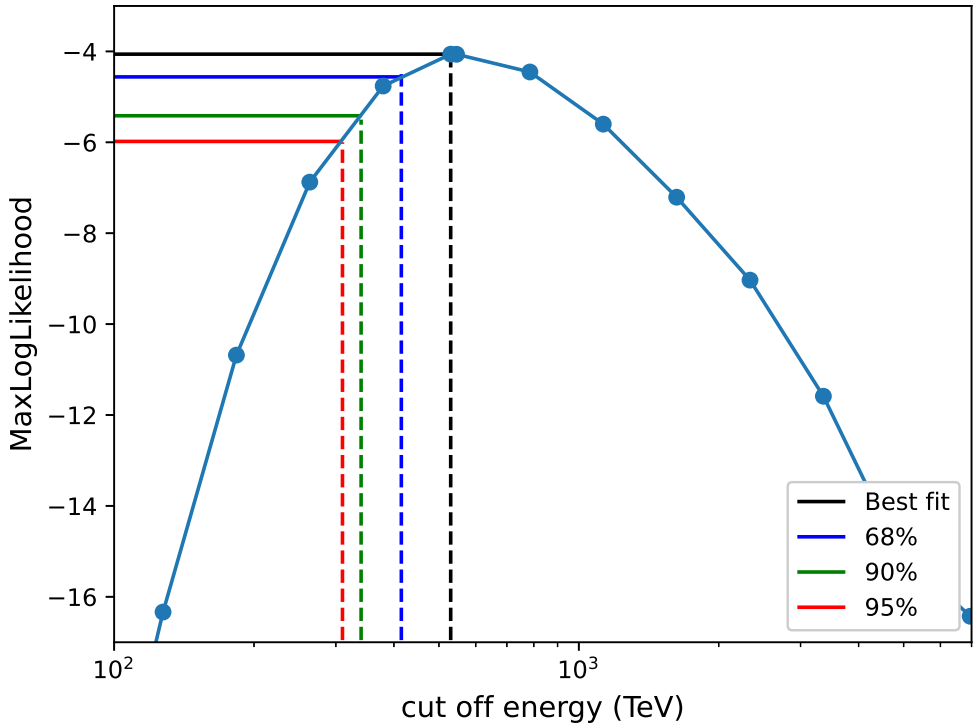

Figure 6.1: Likelihood curve for G106.3+2.7, using SED data points from *Fermi* (Xin et al. 2019), VERITAS (Acciari et al. 2009a) and ASTRI Mini-Array (500 hours exposure time). The red, green, blue and black solid (dashed) lines show the logarithm of the maximum likelihood value (cut-off) at 68%, 90% and 95% confidence level and for the full model respectively

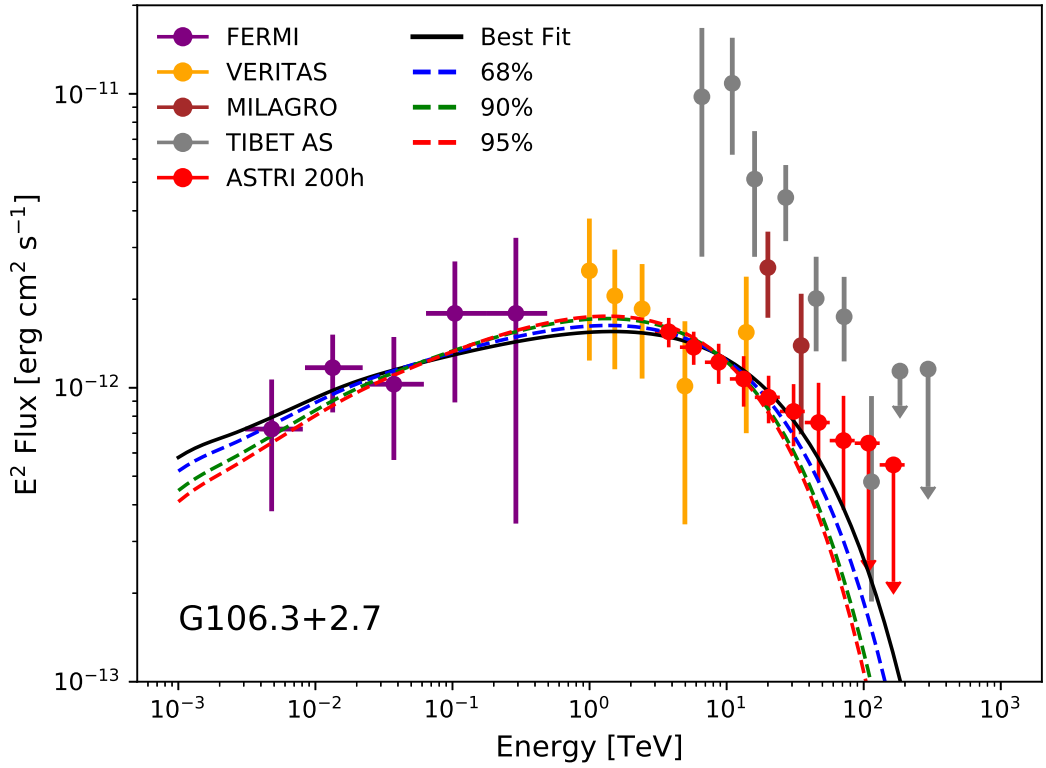

Figure 6.2: G106.3+2.7: γ-ray data from *Fermi* (Xin et al. 2019) (purple dots), VERITAS (Acciari et al. 2009a) (orange dots) and ASTRI Mini-Array (500 hours exposure time) (red dots). Milagro and Tibet AS γ data points from Abdo et al. (2007, 2009); Tibet ASγ Collaboration et al. (2021) are shown for reference only. The solid lines show the emission from a proton population with a best-fit cut-off energy of 530 TeV (black line) and lower-limit energy of 415 (blue line), 340 (green line) and 310 (red line) TeV, (corresponding to 68, 90 and 95% of confidence levels). The ASTRI spectral points and their error bars are obtained from the distribution of 100 simulations. See text for more details.

6.4 A hadronic source: IC 443

In a region with 10° radius around IC 443, two key target sources for the ASTRI Mini-Array are also located: the Crab PWN ($\sim$ 10° angular separation) and the TeV halo of Geminga ($\sim$ 6° angular separation). The vicinity to these promising sources on one hand and the large FoV of the ASTRI Mini-Array, on the other hand, will guarantee a long exposure for IC 443 in the first years of operation. Therefore, to understand what spectral and morphological constraints are achievable for reasonable observational exposures, I simulated the source for 100 and 200 hours. I adopted an extended spatial model (*RadialDisk* in CTOOLS) assuming a radius of 0.16° (Acciari et al. 2009b) and a position 3° off-axis from the pointing position; the spectrum is described as a power-law with an index of 2.99 (Acciari et al. 2009b). I fitted the data using a binned analysis likelihood in the 0.5–200 TeV range, according to standard procedures.

6.4.1 Analysis and Results

As a first step, I tested two spatial models to fit the simulated data: a point source and uniform disk. With 100 hours of exposure, I found a TS value of 334 for the disk morphology, computed using the point source morphology as the *null-hypothesis*, implying a significant improvement using an extended morphology, $> 18\sigma$, that increases to $\sim 25\sigma$ (TS = 664) for 200 hours of exposure. In particular, I found for 200h of exposure and a disk morphology a best fit value of 3.08 ± 0.07 for the power-law index and a radius of $0.166 \pm 0.004°$. Moreover, I found that the SNR is detected up to energies of $\sim$ 20 TeV with 200 hours of exposure, extending the current available SED in the TeV energy band (see Fig. 6.3) and allowing the ASTRI Mini-Array to detect the presence of any possible cut-off in the 1-10 TeV range. The contribution of the measurement of the emission below 60 MeV by *Fermi* (Ackermann et al. 2013) allowed detecting the π^0-decay signature in IC 433, providing direct evidence for the acceleration of protons in SNRs. However, the acceleration and diffusion processes that could cause the emission in this source are not yet well understood. The detection (or not detection) by the ASTRI Mini-Array could bring some new insight into these processes in IC 433 (Tang & Chevalier 2015).

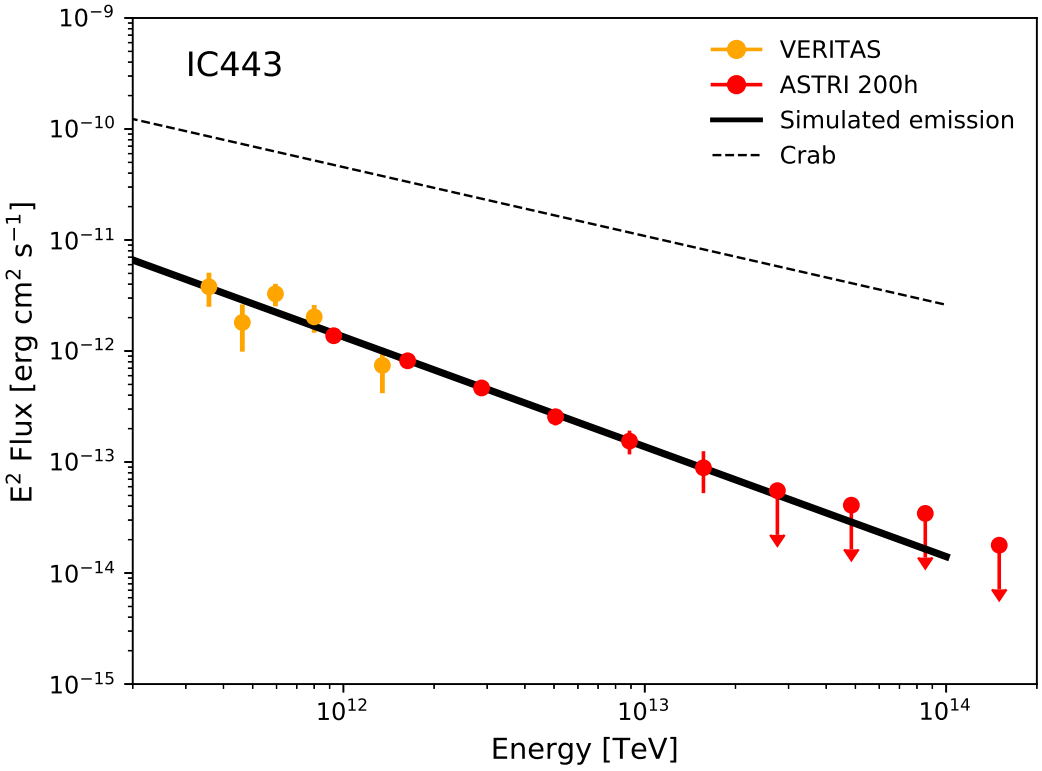

Figure 6.3: IC 443: γ-ray data from VERITAS (Acciari et al. 2009b) (orange dots) and ASTRI Mini-Array (red dots). The solid black line shows the best-fit model for the combined data-sets. I shown for illustrative purposes the Crab spectrum as a dotted line.

Chapter 7

Summary and Conclusions

SNRs are astrophysical sources of prime interest due to the vast physical event and processes that can be investigated through them: from stellar collapse, chemical enrichment of the ISM, thermal and non-thermal processes and CRs acceleration.

In this thesis I have exploited different tools (numerical simulations, multiwavelength analysis, observational previsions) to address various open issues.

- SNRs are complex objects, where physical and chemical properties are strongly affected by several factors such as the stellar progenitor and its CSM, the explosion mechanism and the evolution of the remnant itself. It is almost impossible to have a complete insight into all these phases, due to temporal, physical and observational issues. Numerical simulations are a powerful tool that can provide some answers to these long-standing problems, connecting the gap between SN and SNR on a logical and temporal level.

  I investigated the evolution of the ejecta in core-collapse SNRs from the onset of the SN to the full-fledged remnant. The aim was to analyze how matter mixing occurs during the remnant expansion and interaction with the CSM, how the various chemically homogeneous layers at the time of the explosion map into the resulting abundance pattern observed when the remnant is fully developed, and how the presence of large-scale anisotropies affects the evolution of these layers. To this end, I developed a 3D MHD model describing the evolution of a SNR starting soon after the SN explosion and following the interaction of the SN ejecta with the CSM for 5000 yr. The initial ejecta structure was modeled by including

small-scale clumping of material and larger-scale anisotropy. This type of model is at the state of the art as regards the study of the connection between SN and SNR (see Section 1.4), and provides a useful benchmark to obtain more detailed diagnostic of the ejecta inhomogeneities.

To ascertain the effect of the spherically symmetric expansion of the remnant on the matter-mixing, I first explored a case with small-scale clumpy structures of ejecta without considering any large-scale anisotropy. The ejecta soon after the SN explosion show the original onion-like structure, with elements arranged in concentric shells. Although the onion-like structure is maintained after 5000 years of evolution, which is due to the homologous expansion of the unshocked layers of the ejecta, I observed a significant matter mixing in the inter-shock region of the remnant, as also expected from previous studies (e.g., Gull 1973; Chevalier 1976; Fryxell et al. 1991; Chevalier et al. 1992; see Fig. 4.4). However, this mixing is not able to cause a spatial inversion between chemical layers, leaving the initial chemical configuration of the ejecta roughly preserved.

I then performed a set of simulations to study the evolution of post-explosion large-scale anisotropy (the clump) in the ejecta and its effects on the matter-mixing, investigating the role of its initial parameters (position, dimension, density, and velocity contrasts). I primarily explored two cases: (1) a clump initially located in the ^{56}Fe/^{28}Si region ($D = 0.24$) and (2) a clump in the ^{56}Fe region ($D = 0.15$). In both cases, the clump is located behind a thick and dense shell of lower-Z ejecta. For this thick and dense shell, a higher density contrast is required for the clump to reach the forward shock compared to previous works (Miceli et al. 2013; Tsebrenko & Soker 2015). The dense-shell structure could strongly depend on the progenitor model. This is because different progenitors could produce different density profiles after the explosion, and therefore one should obtain different initial conditions and the clump would evolve in a different environment. The progenitor discussed in this paper (a 19.8 M$_\odot$ progenitor RSG) is a generic case of a RSG among the different progenitors simulated in Ono et al. (2020). The magnetic field is not relevant for the overall evolution of the remnant (the value for plasma-β being much larger than 1) but plays some role in reducing the fragmentation of the clump caused by the HD instabilities that would develop at

its border (Fragile et al. 2005; Shin et al. 2008; Orlando et al. 2008, 2012).

The chemical stratification in the ejecta is strongly affected by the clump, especially in the region along the z-axis. The initial onion-like structure is not preserved, as the clump propagating through the remnant forms a stream of ^{28}Si(^{56}Fe) ejecta, for $D = 0.24$ ($D = 0.15$), from the inner regions up to the intershock region. The clump makes its way out to the external layer of the remnant by piercing the chemically homogeneous shells and pushing the layers on the side of the stream. These streams cause a spatial inversion of the chemical layers, bringing the ^{28}Si/^{56}Fe to the external ^{16}O shell (see Figs. 4.6 and 4.10). Where the effects of the clump's passage are not relevant, that is, in the $(x, y, 0)$ plane, the evolution of the chemical layer is analogous to that described by the spherically symmetric model (see Fig. 4.9). The main effect of this inversion is on the amount of shocked mass of both ^{56}Fe and ^{28}Si as shown in Figs. 4.8, 4.7, and 4.9. I find that a clump initially located in the ^{56}Fe/^{28}Si region does not increase the final amount of shocked ^{28}Si, whereas it doubles the amount of shocked ^{56}Fe. Although the density contrast ($\chi_{\rm n}$) does not produce large effects, the velocity contrast ($\chi_{\rm v}$) has an important role in determining the age of the shocking time of the elements: a higher contrast causes an earlier interaction. As a result, this will produce an earlier appearance of X-ray emission from shocked ejecta. In particular, I find that for a spherically symmetric expansion, the ^{28}Si (^{56}Fe) begins to be shocked after ~ 2000 yr (~ 3000 yr), while the presence of the clump causes an early interaction of both elements with the reverse shock ~ 100 yr (at most) in advance. For a clump initially located in the Fe shell (i.e., $D = 0.15$), I find that the trend over time of the shocked ^{28}Si mass is not affected by the presence of the initial large-scale anisotropy, while on the contrary the final amount of shocked ^{56}Fe increases with increasing size, velocity, and density contrast of the clump.

- I have presented the analysis of ~ 11 years of *Fermi*-LAT data in the region of the Cygnus Loop. The morphological analysis between 0.1 and 100 GeV confirmed an extended emission in the γ-ray band in the shape of a ring with maximum and minimum radii of 1.50° (+0.01,−0.02) and 0.50° (+0.04,−0.07) respectively. I found a strong correlation between the γ-ray emission, the X-ray and UV thermal emission. In particular, I found that the GeV morphology of the Cygnus Loop is

best described by a two-component model: one consisting of a spatial template obtained from the X-ray thermal emission, that is brightest in the north-east region of the remnant, the other consisting of a UV spatial template, that dominates the central and west regions of the remnant. The γ-ray spectra extracted from these two components present a peak at $\sim$ 1 GeV and they can be described by the LogParabola function. Overall, the Cygnus Loop has a γ-ray spectrum that can be described by a power law with subexponential cutoff toward low energies and an integrated energy flux, in the energy band 0.1 - 100 GeV, of $9.0 \pm 0.2 \times 10^{-11}$ erg cm^{-2} s^{-1}.

The peak in the γ-ray spectrum suggests a hadronic origin of the non-thermal emission, as already noted by Katagiri et al. (2011). I constrained the high-energy particles population using a multiwavelength combined fit from radio to γ-ray emission. The wide range of shock speeds in different regions in the Cygnus Loop, together with the results of my morphological analysis, hints at two different possible physical scenarios for the origin of these particles: the DSA mechanism in regions with shock velocity > 150 km s^{-1}, and RPCR otherwise. A caveat in the model is that it favors a distribution of pre-existing CRs softer at 10 MeV than that measured outside our Solar System. The multiwavelength analysis confirms that neither scenario alone is capable of explaining the entire non-thermal emission from the Cygnus Loop, but a model involving both scenarios simultaneously works well. I found that two different populations of hadrons and leptons are responsible for the non-thermal emission: one arising from the DSA mechanism, the other due to the RPCR.

The best-fit model requires a maximum attainable energy $\sim$ 15 GeV for hadrons and leptons in both DSA and RPCR populations. The model has 2% of the kinetic energy released by the SN ending into particles accelerated through DSA (another fraction could have already escaped), and an electron-proton ratio of $K_{ep} \sim 0.01$. The pre-shock filling factor for the RPCR scenario is < 0.01. Because the particles have a harder spectrum below the cut-off in the RPCR scenario, the RPCR component in the gamma-ray spectrum is harder than the DSA component. By extracting radio and γ-ray contributions from the entire Cygnus Loop using the X-ray and UV templates, I disentangled the two different contributions to the non-

thermal emission and unveiled the multiple origins of the accelerated particles in the remnant.

Despite being studied for many years, the Cygnus Loop continues to be of great interest to the community. Models describing the full evolution of the remnant (Ferrand et al. 2019; Ono et al. 2020; Orlando et al. 2020; Tutone et al. 2020) and its thermal and non-thermal emission (Orlando et al. 2012; Miceli et al. 2016; Orlando et al. 2019; Ustamujic et al. 2021) would be very useful.

- In this thesis, I have presented two scientific cases that the ASTRI Mini-Array will be able to address in a long-term planning of observations of the Northern Galactic sky. In the first years of operations, the ASTRI Mini-Array will focus on a core-science program, observing a short list of targets that will be deeply observed to answer primary and outstanding scientific questions. However, the large field of view of the array will allow the simultaneous observations of many close-by VHE targets that will constitute the initial base for the ASTRI Mini-Array observatory science program. In this thesis I have shown how the ASTRI Mini-Array will bring new insight in the quest for PeVatrons by analyzing the case of one of the hottest PeVatron candidates: G106.3+2.7.

  The analysis shows that the ASTRI Mini-Array observation of this remnant might detect is up to 100 TeV. Such detection (or the lack of it) would give tight constraints on the emission mechanisms, if leptonic or hadronic. This would help to understand if the source is an hadronic or leptonic accelerator, or both. Another important contribution would come from the higher spatial resolution of the ASTRI Mini-Array. Recent detections of emission above 10 TeV with Tibet AS γ (Tibet ASγ Collaboration et al. 2021) and LHAASO (Cao et al. 2021) telescopes, which due to their low angular resolution ($0.70 - -0.94^{\circ}$ at ~ 10 TeV for LHAASO) can not distinguish if this emission comes from the pulsar region or the molecular clouds near the remnant. The higher angular resolution of the ASTRI Mini-Array not only will allow associating the γ-ray emission to one specific region, but it will also allow an energy dependent study of the morphology of the remnant.

  Significant improvements, in terms of spectral and morphological estimations, can be obtained also for a sample case among the several sources listed in Ta-

ble 6.1: the SNR IC 443. The γ-ray emission from the remnant can be explained by an hadronic model, but it is not clear if hadrons come from RPCR and/or freshly accelerated particles that have entered the dense region around the remnant (Ackermann et al. 2013). By extending the γ-ray spectrum up to TeV energies the ASTRI Mini-Array would help to answer these questions. Moreover, the ASTRI Mini-Array would also look for possible spectral differences in different regions of the remnant that could reflect different environmental conditions.

Chapter 8

Acknowledgments

I would like to express my gratitude to my supervisor Dr. G. Cusumano and my co-supervisor Dr. A. D'Aì for the significant help, wise indications and constant support through all my PhD studies and for improving this thesis with their suggestions and indications. I sincerely acknowledge Dr. J. Ballet and Dr. F. Acero for the fruitful discussions, precious advices and kind hospitality they reserved to me and for their collaboration during the Covid lockdown. I extend my thanks to Dr. S. Orlando, Dr. M. Miceli , Dr. F. Bocchino and Prof. G. Peres for the support and hospitality in the Supernova Remnant astrophysics group at the INAF - Osservatorio Astronomico di Palermo. My sincere thanks also go to Prof. S. Nagataki, Dr. M. Ono, Dr. G. Ferrand and Dr. D.C. Warren for their contribution to some of the work presented here. Finally, I want to express my gratitude to all the people at the INAF - Istituto di Astrofisica Spaziale e Fisica Cosmica for their assistance and for make me feel like I was home.

Acronyms

AGILE Astrorivelatore Gamma ad Immagini LEggero.

AGN Active Galactic Nuclei.

ASTRI Astrofisica con Specchi a Tecnologia Replicante Italiana.

BH Black Hole.

CC Core-Collapse.

CMB Cosmic Microwave Background Radiation.

CR Cosmic Rays.

CSM Circumstellar Medium.

CTA Cherenkov Telescope Array.

DSA Diffusive Shock Acceleration.

EAS Extended Air Shower.

GBM Gamma-Ray Burst Monitor.

GCR Galactic CRs.

GTI Good Time Interval.

H.E.S.S. High Energy Stereoscopic System.

HAWC High Altitude Water Cherenkov Experiment.

HD Hydrodynamics.

HE High Energy.

IACT imaging atmospheric Cherenkov telescopes.

IC Inverse Compton.

INAF Italian National Institute for Astrophysics.

IRF Instrument Response Function.

ISM Interstellar Medium.

LAT Large Area Telescope.

LHAASO Large High Altitude Air Shower Observatory.

LP Log Parabola.

LST Large-Sized Telescope.

MAGIC Major Atmospheric Gamma-ray Imaging Cherenkov Telescopes.

MHD Magneto Hydrodynamics.

MMSNR mixed-morphology SNR.

MST Medium-Sized Telescope.

NS Neutron Star.

PSF Point Spread Function.

PWN Pulsar Wind Nebulae.

ROI Region of Interestf.

RPCR Re-acceleration of Pre-existing ambient CRs.

RRL Radiative Relaxation Layer.

RSG Red Supergiant.

RT Rayleigh-Taylor.

SASI Standing Accretion Shock Instability.

SED Spectral Energy Distribution.

SiPM Silicon Photo-Multipliers.

SN Supernova.

SNR Supernova Remnant.

SST Small-Sized Telescope.

TS Test Statistic.

UHECRs Ultrahigh-Energy Cosmic Rays.

VERITAS Very Energetic Radiation Imaging Telescope Array System.

VHE Very High Energy.

List of Figures

1.1 The classification of supernovae, based on optical spectroscopy and light-curve shape (Vink 2012). 10
1.2 Bolometric light curves of representative SNe. 11
1.3 Examples of SNRs morphology: a) Cygnus Loop, shell type SNR, b) Crab Nebula, plerion SNR, c) Kes 75, composite SNR.(Image Credit: NASA, ESA, J. Hester, A. Loll (ASU)) 14
1.4 Spherically-symmetric hydrodynamic model of the Cas A SNR. Upper and lower frames show velocity and density profiles along the radial direction of the SNR at t = 330 year. The density profile of SN ejecta is composed of a inner flat portion and outer steep power-law portion. The ambient medium is RSG wind with a density profile of $\propto r^{-2}$ (Chevalier & Oishi 2003). 17

2.1 γ-ray energy spectra for several of the most prominent SNRs. Young SNRs ($< 10^3$ years) are shown in green. Shell-type SNRs of ages $\sim 2 \times 10^3$ years are shown in shades of red. The middle-aged SNRs ($\sim 2 \times 10^4$ years) are shown in blue. Also shown are hadronic fits to the data (solid lines). Figure from Funk 2015. 29

3.1 Layout of the ASTRI Mini-Array. The figure shows the final positions of the 9 ASTRI telescopes (red circles). 37
3.2 On-axis energy resolution (top), angular resolution (middle) and differential sensitivity (bottom) of the ASTRI Mini-Array for 50 hours of observations as a function of the energy between $\simeq$ 0.3 TeV and $\simeq$ 200 TeV (Lombardi et al. 2021). 38

3.3 ASTRI Mini-Array differential sensitivity (Lombardi et al. 2021) compared with those of current imaging atmospheric Cherenkov telescope arrays. The differential sensitivity curves come from Aleksić et al. 2016 (MAGIC), the VERITAS official website (https://veritas.sao.arizona.edu) and Holler et al. 2015 (H.E.S.S.). 39

4.1 Initial conditions for the 3D simulations. *Top panel:* Radial profiles of initial ejecta density (black line) and pressure (red line). *Bottom panel*: Radial profiles of initial ejecta velocity (black line) and Mach number (red line). 46

4.2 Density (left-hand quadrants) and temperature (right-hand quadrants) sections $(x, 0, z)$ showing examples of the initial conditions. The values are color coded according to the scale shown for each quadrant. Upper quadrants show the case of a spherically symmetric explosion, and lower quadrants show a case with a dense, isobaric spherical anisotropy (namely run Si-R5-D750-V5 in Table 4.1). 47

4.3 Density distributions in the $(x, 0, z)$ plane at different simulation times for a spherically symmetric explosion (left-panel) and for model Fe-R5-D750-V6 of Table 4.1 (right-panel). From top left clockwise: $t = 10$, $t = 100$, $t = 1000$ and $t = 5000$ years from the explosion. The units in the color bars are g cm^{-3} logarithmically scaled. The color-coded density scale is shown close to each quadrant. In the right panel the contours enclose the computational cells consisting of the original anisotropy material by more than 50% (solid line) and 10% (dotted line). See also online Movie 1 and 2 for an animated version. 55

4.4 Mass distributions of selected elements as a function of radial velocity for the spherically symmetric explosion at the labeled years from the explosion. The upper left panel shows the initial conditions from Ono et al. (2020). Only the dominant fractions are considered. M_i is the total ejecta mass of element i, ΔM_i is the mass of the i-th element in the velocity range between v and $v + \delta v$. The size of the velocity bins δv is 100 km s^{-1}. The black dashed vertical line shows the approximate reverse shock position in each panel. 57

4.5 Same as the right panel of Fig. 4.3 but for model Fe-R5-D750-V3 (see Table 4.1) 58
4.6 Color-coded images of the logarithm of the ejecta mass fraction (¿ 10^{-4}) distributions at the end of the simulation ($t \approx 5000$ years) for different models (the model as presented in Table 4.1 is reported near each quadrant) in the $(x, 0, z)$ plane of ^{56}Fe (red), ^{28}Si (green), and ^{16}O (blue). Black contours enclose the computational cells consisting of the original clump material by more than 50% (solid line) and 10% (dotted line). The white dashed line represents the projected position of the forward shock; see also online Movie 3, 4, 5, and 6 for an animated version. . . 61
4.7 Mass of shocked ^{28}Si (upper panel) and ^{56}Fe (lower panel) vs. time for models assuming a clump initially located at $D = 0.15$ and characterized by different parameters (see Table 4.1). The shocked mass is normalized to the total mass of the relative element. 63
4.8 Same as Fig. 4.7 but for models with a clump initially located at $D = 0.24$. 66
4.9 Mass of shocked ^{28}Si (upper panel) and ^{56}Fe (lower panel) vs. time for the spherically symmetric explosion (green lines) and for model Fe-R5-D750-V7 (red lines, see Table 4.1). Solid and dashed lines show the shocked mass from cells within 45° of the z-axis and from 15° of the equatorial plane respectively, while the dotted lines show the mass from the others cells. The shocked mass is normalized to the total mass of the relative element in the region considered. 67
4.10 Upper panel: Density distribution map integrated along the line of sight (in this case the y-axis) of the run Fe-R5-D750-V7, showing the regions chosen for the spectral synthesis: red for the anisotropy protruding the remnant outline (the clump), black for the wake of the anisotropy, and green for a region of the shell not affected by the anisotropy (the shell). Lower panel: X-ray *Chandra* ACIS-S synthetic spectra in the 0.5-2 keV energy band for the clump (red), the wake (black), and the shell (green). 68

4.11 Left panel: Density distributions in the $(x, 0, z)$ plane at the end of simulation time for a SN explosion with a large-scale anisotropy (upper quadrants) (runs Fe-R4-D750-V6 and Fe-R4-D750-V6-512pt in Table 4.1) and for a spherically symmetric explosion (lower quadrants), at low resolution (256^3 grid points; left quadrants) and high-resolution (512^3 grid points; right quadrants). Right panel: Same but for color-coded images of the logarithm of the mass fraction distributions of Fe (red), Si (green), O (blue). In the upper quadrants of each panel, the black contours enclose the computational cells consisting of the original anisotropy material by more than 10% (dotted line) and 50% (solid line). The white dashed line represents the approximate position of the forward shock. 70

4.12 Left panel: Amount of ^{56}Fe and ^{28}Si mass vs. time in cells with a mass fraction between 10% and 50% for a spherically symmetric explosion at different resolution. Right panel: Amount of ^{56}Fe and ^{28}Si mass vs. time in cells with a mass fraction between 10% and 50% and with anisotropy material between 10% and 90% for models Fe-R4-D750-V6 (256^3 grid points) and Fe-R4-D750-V6-512pt (512^3 grid points) (see Table 4.1). 71

4.13 Density distribution maps in the (x,0,z) plane at $t \approx 100$ (upper panels) and $t \approx 5000$ years from the explosion (lower panels). Right: Model Fe-R4-D750-V6 (see Table 4.1). Left: Same model with the initial position of the clump located at 45° in the (x,0,z) plane, namely Fe-R4-D750-V6-ROT. On the left panels the (x,0,z) plane from the simulation is rotated to the z-axis for comparison, and thus the lower blue triangle is not part of the computational domain. The contours enclose the computational cells consisting of the original anisotropy material by more than 50% (continuous line) and 10% (dotted line). 73

4.14 Mass vs. time (in logarithmic scale) for the two models compared in Fig. 4.13. Total mass in cells with anisotropy material by more than 10% (continuous line) and in the range 10–90% (dotted line). In every case the mass is normalized to the value of the mass in the first step of the simulation. 74

5.1 Templates used to fit the γ-ray data, in celestial coordinates. Top left, X-rays (ROSAT, 5.2.2); top right, UV (GALEX NUV, 5.2.3); bottom left, optical (DSS2 red, 5.2.4); bottom right, radio (11 cm, Effelsberg, 5.2.5). All maps are aligned and shown in square root scaling from 0 to the maximum. 79

5.2 *Left:* Count map in a $10^\circ \times 10^\circ$ (pixel size of 0.05°) region around the Cygnus Loop (smoothed with a Gaussian kernel of 0.2°) from 0.1 to 100 GeV. *Center:* Count map expected from the X-ray+UV model (same spatial binning as the left map). Green crosses indicate the positions of γ-ray sources listed in the 4FGL catalogue. The cyan line is the contour (10% of the maximum) of the *ROSAT* X-ray template of the Cygnus Loop (see 5.2.2). *Right:* Residual count map from the X-ray+UV template model (pixel size of 0.5°). 84

5.3 Residual count map in a $6^\circ \times 6^\circ$ (pixel size of 0.05°) region around the Cygnus Loop (smoothed with a Gaussian kernel of 0.2°) obtained from 0.1 to 100 GeV without the Cygnus Loop included in the model (*null-hypothesis*), with different templates overlaid. *Top Left:* Best-fit disk and Gaussian models represented in red and white, respectively. The 4FGL sources are shown in green. The ring model (4FGL J2051.0+3049e) introduced by Katagiri et al. (2011) is shown in green. *Top right:* Best-fit ring model (green). The blue lines define the 4 sections used for the morphology analysis. *Bottom left:* Contours of the *ROSAT* X-ray (cyan, see 5.2.2) template. The templates were smoothed with a Gaussian Kernel of $\sigma = 0.2^\circ$ to make the contours more regular. Contours for the X-ray template are at $30\%, 20\%, 10\%$ and 1% of the maximum. *Bottom right:* Contours for the *GALEX* UV (cyan, see 5.2.3) template are at $40\%, 25\%, 15\%$ and 2% of the maximum. 85

5.4 Spectral energy distribution of the γ-ray emission measured with the LAT for the Cygnus Loop. The filled histograms show the TS values in each energy bin. Vertical bars show 1σ statistical errors. Where the detection is not significant (TS < 4), I show upper limits at the 95% confidence level. *Upper panel:* SED extracted using the UV template. The PLSuperExpCutoff4 best-fit spectrum for the global γ-ray data (Table 5.3) is plotted as the black dashed line, and its upper and lower 1σ bounds as the black solid lines. *Lower panel:* Red (green) points are LAT flux points using the X-ray (UV) maps as spatial templates together. The lines are the best-fit LogParabola models (Table 5.4). 92

5.5 Residuals after fitting the 11 cm Effelsberg map with a combination of the UV and X-ray templates. Left, standard χ^2 fit resulting in deep negative residuals. Right, fit increasing the errors by a factor 10 for positive residuals, with no negative residuals but larger positive residuals. 93

5.6 Pre-existing ambient CR spectra of protons (left) and electrons (right) as a function of particles kinetic energy. Black solid lines show the spectra from Phan et al. (2018), red dashed lines show the spectra from Uchiyama et al. (2010). 97

5.7 Re-accelerated and compressed protons (left) and electrons (right) vs kinetic energy with radiative compression $s = 12$, a cut-off at 100 GeV and a break at 50 GeV as reference values. Black solid lines show the spectra when starting from Phan et al. (2018), red dashed lines from Uchiyama et al. (2010). 98

5.8 γ-ray spectrum of the Cygnus Loop extracted with the X-ray template and modeled emission in the DSA scenario. Solid lines show the total contribution of Bremsstrahlung radiation, IC and π^0-decay. The total energy ($W_{\rm tot} = 1.2 \times 10^{49}$ erg), the electron-to-proton ratio ($K_{\rm ep} = 0.01$ at 10 GeV) and the break energy ($p_{\rm br}$ = 62 GeV/c) are fixed. Different cut-off energy values are shown. 101

5.9 DSA scenario for the multiwavelength modeling of the emission, extracted with the X-ray template, toward the Cygnus Loop. Radio data are obtained as explained in Sect. 5.3.3. The total contribution from Bremsstrahlung, IC and π^0-decay is shown by the black solid line. The best model is obtained with a total energy $W_{\rm tot}$ of 1.2×10^{49} erg and the electron-to-proton ratio $K_{\rm ep} = 0.01$ at 10 GeV. Protons and electrons have an energy cut-off of 15 GeV and an energy break of 62 GeV. . . . 102

5.10 γ-ray spectrum of the Cygnus Loop extracted with the UV template and modeled emission in the RPCR scenario (eq. 5.12). Solid lines show the total contribution of Bremsstrahlung radiation, IC and π^0-decay. *Upper panels:* pre-existing CR from Phan et al. (2018). On the right (left) different cut-off (break) energy values at $p_{\rm br}c = 4.3$ GeV ($p_{\rm max}c = 22$ GeV). Note that the actual cut-off/break energies in the radiative zone are $s^{1/3}p_{\rm max}c$ and $s^{1/3}p_{\rm br}c$. The filling factor f is fixed to $f = 0.013$. *Lower panels:* pre-existing CR from Uchiyama et al. (2010). The filling factor f is fixed to $f = 0.013$. 104

5.11 RPCR scenario for the multiwavelength modeling of the emission, extracted with the UV template, toward the Cygnus Loop. Radio data are obtained as explained in Section 5.3.3. The total contribution from Bremsstrahlung, IC, and π^0 decay is shown by the solid black line. My best model is obtained with preexisting CR populations from Phan et al. (2018) and a filling factor of $f = 0.013$. Spectral parameters for protons and electrons are $s^{1/3}p_{\rm max}c = 20$ GeV and $s^{1/3}p_{\rm br}c = 70$ GeV. 105

5.12 Radio and γ-ray emission from the entire Cygnus Loop. Radio data points (transparent green) from Uyanıker et al. (2004) and Loru et al. (2021) were scaled by a constant factor (dark green) to remove the contribution from the southern region (see Section 5.3.3). The total contribution from Bremsstrahlung, IC, and π^0 decay is shown by the solid black line. *Upper panel:* DSA scenario, adopting values of $p_{\rm max}c = 40$ GeV, $p_{\rm br}c = 62$ GeV, $W_{\rm tot} = 2.1 \times 10^{49}$ erg, and $K_{\rm ep} = 0.025$ for protons and electrons. *Lower panel:* RPCR scenario, adopting preexisting CR populations from Phan et al. (2018), $s^{1/3}p_{\rm max}c = 20$ GeV, $s^{1/3}p_{\rm br}c = 70$ GeV, and a filling factor $f \sim 0.02$. 106

5.13 Same as Figure 5.12, but the multiwavelength model has multiple contributions. *Upper panel:* DSA scenario (solid lines) and RPCR scenario (dot-dashed lines). The total contribution from the two scenarios is shown by the solid black line. *Lower panel:* Same as the upper panel, but with contribution from the intercloud region (DSA 2). 107

6.1 Likelihood curve for G106.3+2.7, using SED data points from *Fermi* (Xin et al. 2019), VERITAS (Acciari et al. 2009a) and ASTRI Mini-Array (500 hours exposure time). The red, green, blue and black solid (dashed) lines show the logarithm of the maximum likelihood value (cut-off) at 68%, 90% and 95% confidence level and for the full model respectively 116

6.2 G106.3+2.7: γ-ray data from *Fermi* (Xin et al. 2019) (purple dots), VERITAS (Acciari et al. 2009a) (orange dots) and ASTRI Mini-Array (500 hours exposure time) (red dots). Milagro and Tibet AS γ data points from Abdo et al. (2007, 2009); Tibet ASγ Collaboration et al. (2021) are shown for reference only. The solid lines show the emission from a proton population with a best-fit cut-off energy of 530 TeV (black line) and lower-limit energy of 415 (blue line), 340 (green line) and 310 (red line) TeV, (corresponding to 68, 90 and 95% of confidence levels). The ASTRI spectral points and their error bars are obtained from the distribution of 100 simulations. See text for more details. . . . 117

6.3 IC 443: γ-ray data from VERITAS (Acciari et al. 2009b) (orange dots) and ASTRI Mini-Array (red dots). The solid black line shows the best-fit model for the combined data-sets. I shown for illustrative purposes the Crab spectrum as a dotted line. 119

Bibliography

Abdo, A. A., Ackermann, M., Ajello, M., et al. 2011, The Astrophysical Journal, 734, 28

Abdo, A. A., Ackermann, M., Ajello, M., et al. 2010, The Astrophysical Journal, 712, 459

Abdo, A. A., Allen, B., Berley, D., et al. 2007, The Astrophysical Journal Letters, 664, L91

Abdo, A. A., Allen, B. T., Aune, T., et al. 2009, The Astrophysical Journal Letters, 700, L127

Abdollahi, S., Acero, F., Ackermann, M., et al. 2020a, The Astrophysical Journal Supplement, 247, 33

Abdollahi, S., Ballet, J., Fukazawa, Y., Katagiri, H., & Condon, B. 2020b, The Astrophysical Journal, 896, 76

Abeysekara, A. U., Albert, A., Alfaro, R., et al. 2020, Physical Review Letters, 124, 021102

Abeysekara, A. U., Alfaro, R., Alvarez, C., et al. 2013, Astroparticle Physics, 50, 26

Acciari, V. A., Aliu, E., Arlen, T., et al. 2009a, The Astrophysical Journal Letters, 703, L6

Acciari, V. A., Aliu, E., Arlen, T., et al. 2009b, The Astrophysical Journal Letters, 698, L133

Acero, F., Ackermann, M., Ajello, M., et al. 2016, The Astrophysical Journal Supplement, 224, 8

Ackermann, M., Ajello, M., Allafort, A., et al. 2013, Science, 339, 807

Aguilar, M., Aisa, D., Alpat, B., et al. 2015, Physical Review Letters, 114, 171103

Aharonian, F., Akhperjanian, A. G., Bazer-Bachi, A. R., et al. 2006, Astronomy and Astrophysics, 457, 899

Aharonian, F., Akhperjanian, A. G., Bazer-Bachi, A. R., et al. 2007, Astronomy and Astrophysics, 464, 235

Ahmad, I., Greene, J. P., Moore, E. F., et al. 2006, Physical Review C, 74, 065803

Akaike, H. 1974, IEEE Transactions on Automatic Control, 19, 716

Albert, A., Alfaro, R., Alvarez, C., et al. 2020, The Astrophysical Journal Letters, 896, L29

Albert, J., Aliu, E., Anderhub, H., et al. 2007, The Astrophysical Journal Letters, 664, L87

Aleksić, J., Alvarez, E. A., Antonelli, L. A., et al. 2012, Astroparticle Physics, 35, 435

Aleksić, J., Ansoldi, S., Antonelli, L. A., et al. 2016, Astroparticle Physics, 72, 61

Aleksić, J., Ansoldi, S., Antonelli, L. A., et al. 2015, Journal of High Energy Astrophysics, 5, 30

Aleksić, J., Ansoldi, S., Antonelli, L., et al. 2016, Astroparticle Physics, 72, 76–94

Aliu, E., Archambault, S., Aune, T., et al. 2014, The Astrophysical Journal, 787, 166

Amato, E. 2014, International Journal of Modern Physics D, 23, 1430013

Archambault, S., Archer, A., Benbow, W., et al. 2017, The Astrophysical Journal, 836, 23

Aschenbach, B., Egger, R., & Trümper, J. 1995, Nature, 373, 587

Aschenbach, B. & Leahy, D. A. 1999, Astronomy and Astrophysics, 341, 602

Atwood, W. B., Abdo, A. A., Ackermann, M., et al. 2009, The Astrophysical Journal, 697, 1071

Barbarino, C., Dall'Ora, M., Botticella, M. T., et al. 2015, Monthly Notices of the Royal Astronomical Society, 448, 2312

Bear, E. & Soker, N. 2018, Monthly Notices of the Royal Astronomical Society, 478, 682

Bell, A. R. 1978a, Monthly Notices of the Royal Astronomical Society, 182, 147

Bell, A. R. 1978b, Monthly Notices of the Royal Astronomical Society, 182, 443

Berezhko, E. G., Ksenofontov, L. T., & Völk, H. J. 2002, Astronomy and Astrophysics, 395, 943

Bertin, E. & Arnouts, S. 1996, Astronomy and Astrophysics Supplement Series, 117, 393

Bionta, R. M., Blewitt, G., Bratton, C. B., et al. 1987, Physical Review Letters, 58, 1494

Blair, W. P., Sankrit, R., & Tulin, S. 2002, The Astrophysical Journal Supplement, 140, 367

Blandford, R. & Eichler, D. 1987, Physics Reports, 154, 1

Blandford, R. D. & Ostriker, J. P. 1978, The Astrophysical Journal Letters, 221, L29

Blasi, P. 2013, The Astronomy and Astrophysics Review, 21, 70

Blondin, J. M., Mezzacappa, A., & DeMarino, C. 2003, The Astrophysical Journal, 584, 971

Blondin, J. M., Wright, E. B., Borkowski, K. J., & Reynolds, S. P. 1998, The Astrophysical Journal, 500, 342

Brinkmann, W., Siebert, J., Feigelson, E. D., et al. 1997, Astronomy and Astrophysics, 323, 739

Bruenn, S. W., Mezzacappa, A., Hix, W. R., et al. 2013, The Astrophysical Journal Letters, 767, L6

Burrows, A., Radice, D., & Vartanyan, D. 2019, Monthly Notices of the Royal Astronomical Society, 485, 3153

Bykov, A. M., Krassilchtchikov, A. M., Uvarov, Y. A., et al. 2008, The Astrophysical Journal, 676, 1050

Cao, Z., Aharonian, F. A., An, Q., et al. 2021, Nature, 594, 33

Caprioli, D. 2012, Journal of Cosmology and Astroparticle Physics, 2012, 038

Cardillo, M., Amato, E., & Blasi, P. 2015, Astroparticle Physics, 69, 1

Cardillo, M., Amato, E., & Blasi, P. 2016, Astronomy and Astrophysics, 595, A58

Catalano, O., Capalbi, M., Gargano, C., et al. 2018, in Society of Photo-Optical Instrumentation Engineers (SPIE) Conference Series, Vol. 10702, Ground-based and Airborne Instrumentation for Astronomy VII, ed. C. J. Evans, L. Simard, & H. Takami, 1070237

Cherenkov Telescope Array Consortium, Acharya, B. S., Agudo, I., et al. 2019, Science with the Cherenkov Telescope Array

Chernyakova, M., Malyshev, D., Paizis, A., et al. 2019, Astronomy and Astrophysics, 631, A177

Chevalier, R. A. 1976, The Astrophysical Journal, 207, 872

Chevalier, R. A., Blondin, J. M., & Emmering, R. T. 1992, The Astrophysical Journal, 392, 118

Chevalier, R. A. & Oishi, J. 2003, The Astrophysical Journal, 593, L23

Choudhuri, A. R. 1998, The physics of fluids and plasmas : an introduction for astrophysicists (Cambridge University Press)

Condon, J. J., Cotton, W. D., Greisen, E. W., et al. 1998, The Astronomical Journal, 115, 1693

Cornett, R. H., Chin, G., & Knapp, G. R. 1977, Astronomy and Astrophysics, 54, 889

Couch, S. M. & O'Connor, E. P. 2014, The Astrophysical Journal, 785, 123

Cristofari, P., Blasi, P., & Amato, E. 2020, Astroparticle Physics, 123, 102492

Crowther, P. A. 2001, in Astrophysics and Space Science Library, Vol. 264, The Influence of Binaries on Stellar Population Studies, ed. D. Vanbeveren, 215

Cummings, A. C., Stone, E. C., Heikkila, B. C., et al. 2016, The Astrophysical Journal, 831, 18

DeLaney, T., Rudnick, L., Stage, M. D., et al. 2010, The Astrophysical Journal, 725, 2038

Denoyer, L. K. 1978, Monthly Notices of the Royal Astronomical Society, 183, 187

Devin, J., Acero, F., Ballet, J., & Schmid, J. 2018, Astronomy and Astrophysics, 617, A5

Devin, J., Lemoine-Goumard, M., Grondin, M. H., et al. 2020, Astronomy and Astrophysics, 643, A28

Dewey, D., Dwarkadas, V. V., Haberl, F., Sturm, R., & Canizares, C. R. 2012, The Astrophysical Journal, 752, 103

Diehl, R., Halloin, H., Kretschmer, K., et al. 2006, Nature, 439, 45

Duvidovich, L., Petriella, A., & Giacani, E. 2020, Monthly Notices of the Royal Astronomical Society, 491, 5732

Dwarkadas, V. V. 2005, The Astrophysical Journal, 630, 892

Dwarkadas, V. V. & Chevalier, R. A. 1998, The Astrophysical Journal, 497, 807

Fang, J., Yu, H., & Zhang, L. 2017, Monthly Notices of the Royal Astronomical Society, 464, 940

Fermi, E. 1949, Physical Review, 75, 1169

Ferrand, G. & Safi-Harb, S. 2012, Advances in Space Research, 49, 1313

Ferrand, G., Warren, D. C., Ono, M., et al. 2019, The Astrophysical Journal, 877, 136

Fesen, R. A., Hammell, M. C., Morse, J., et al. 2006, The Astrophysical Journal, 636, 859

Fesen, R. A., Weil, K. E., Cisneros, I. A., Blair, W. P., & Raymond, J. C. 2018, Monthly Notices of the Royal Astronomical Society, 481, 1786

Filippenko, A. V. 1997, Annual Review of Astronomy and Astrophysics, 35, 309

Fragile, P. C., Anninos, P., Gustafson, K., & Murray, S. D. 2005, The Astrophysical Journal, 619, 327

Fryxell, B., Mueller, E., & Arnett, D. 1991, The Astrophysical Journal, 367, 619

Fryxell, B., Olson, K., Ricker, P., et al. 2000, The Astrophysical Journal Supplement, 131, 273

Funk, S. 2015, Annual Review of Nuclear and Particle Science, 65, 245

Gabler, M., Janka, H.-T., & Wongwathanarat, A. 2017, in IAU Symposium, Vol. 331, Supernova 1987A:30 years later - Cosmic Rays and Nuclei from Supernovae and their Aftermaths, ed. A. Marcowith, M. Renaud, G. Dubner, A. Ray, & A. Bykov, 141–147

Gaisser, T. K. 1990, Cosmic rays and particle physics.

García, F., Suárez, A. E., Miceli, M., et al. 2017, Astronomy and Astrophysics, 604, L5

Gawryszczak, A., Guzman, J., Plewa, T., & Kifonidis, K. 2010, Astronomy and Astrophysics, 521, A38

Giordano, F., Naumann-Godo, M., Ballet, J., et al. 2012, The Astrophysical Journal Letters, 744, L2

Giuliani, A., Cardillo, M., Tavani, M., et al. 2011, The Astrophysical Journal Letters, 742, L30

Greco, E., Miceli, M., Orlando, S., et al. 2018, Astronomy and Astrophysics, 615, A157

Greco, E., Vink, J., Miceli, M., et al. 2020, Astronomy and Astrophysics, 638, A101

Green, D. A. 2014, Bulletin of the Astronomical Society of India, 42, 47

Grefenstette, B. W., Fryer, C. L., Harrison, F. A., et al. 2017, The Astrophysical Journal, 834, 19

Grefenstette, B. W., Harrison, F. A., Boggs, S. E., et al. 2014, Nature, 506, 339

Gull, S. F. 1973, Monthly Notices of the Royal Astronomical Society, 161, 47

Haas, M. R., Colgan, S. W. J., Erickson, E. F., et al. 1990, The Astrophysical Journal, 360, 257

Hanabata, Y., Katagiri, H., Hewitt, J. W., et al. 2014, The Astrophysical Journal, 786, 145

HI4PI Collaboration, Ben Bekhti, N., Flöer, L., et al. 2016, Astronomy and Astrophysics, 594, A116

Hirata, K., Kajita, T., Koshiba, M., et al. 1987, in The Standard Model. The Supernova 1987A, ed. J. Tran Thanh Van, 727–734

Hollenbach, D. & McKee, C. F. 1989, The Astrophysical Journal, 342, 306

Holler, M., de Naurois, M., Zaborov, D., Balzer, A., & Chalmé-Calvet, R. 2015, in International Cosmic Ray Conference, Vol. 34, 34th International Cosmic Ray Conference (ICRC2015), 980

Huang, F., Wang, X., Zhang, J., et al. 2015, The Astrophysical Journal, 807, 59

Hughes, J. P., Rakowski, C. E., Burrows, D. N., & Slane, P. O. 2000, The Astrophysical Journal Letters, 528, L109

Janka, H.-T. 2017, Neutrino-Driven Explosions (ISBN 978-3-319-21845-8. Springer International Publishing AG), 1095

Janka, H.-T., Melson, T., & Summa, A. 2016, Annual Review of Nuclear and Particle Science, 66, 341

Joggerst, C. C., Almgren, A., & Woosley, S. E. 2010, The Astrophysical Journal, 723, 353

Joggerst, C. C., Woosley, S. E., & Heger, A. 2009, The Astrophysical Journal, 693, 1780

Jogler, T. & Funk, S. 2016, The Astrophysical Journal, 816, 100

Katagiri, H., Tibaldo, L., Ballet, J., et al. 2011, The Astrophysical Journal, 741, 44

Katsuda, S., Acero, F., Tominaga, N., et al. 2015, The Astrophysical Journal, 814, 29

Katsuda, S., Maeda, K., Ohira, Y., et al. 2016, The Astrophysical Journal Letters, 819, L32

Katsuda, S., Mori, K., Tsunemi, H., et al. 2008a, The Astrophysical Journal, 678, 297

Katsuda, S., Tsunemi, H., Kimura, M., & Mori, K. 2008b, The Astrophysical Journal, 680, 1198

Katsuda, S., Tsunemi, H., Mori, K., et al. 2011, The Astrophysical Journal, 730, 24

Kifonidis, K., Plewa, T., Scheck, L., Janka, H.-T., & Müller, E. 2006, Astronomy and Astrophysics, 453, 661

Kim, I.-J., Seon, K.-I., Lim, Y.-M., et al. 2014, The Astrophysical Journal, 784, 12

Knödlseder, J., Mayer, M., Deil, C., et al. 2016, Astronomy and Astrophysics, 593, A1

Koo, B.-C., Lee, J.-J., Jeong, I.-G., Seok, J. Y., & Kim, H.-J. 2016, The Astrophysical Journal, 821, 20

Lamastra, A., Tavecchio, F., Romano, P., Landoni, M., & Vercellone, S. 2019, Astroparticle Physics, 112, 16

Landau, L. D. & Lifshitz, E. M. 1959, Fluid mechanics

Law, C. J., Milisavljevic, D., Patnaude, D. J., et al. 2020, The Astrophysical Journal, 894, 73

Leahy, D. A. 2004, The Astronomical Journal, 127, 2277

Lee, J.-J., Koo, B.-C., Snell, R. L., et al. 2012, The Astrophysical Journal, 749, 34

Lee, J.-J., Koo, B.-C., Yun, M. S., et al. 2008, The Astronomical Journal, 135, 796

Lee, S.-H., Patnaude, D. J., Raymond, J. C., et al. 2015, The Astrophysical Journal, 806, 71

Levenson, N. A., Graham, J. R., Keller, L. D., & Richter, M. J. 1998, The Astrophysical Journal Supplement, 118, 541

Liu, S., Zeng, H., Xin, Y., & Zhu, H. 2020, The Astrophysical Journal, 897, L34

Lombardi, S., Antonelli, L. A., Bigongiari, C., et al. 2021, 884

Lombardi, S., Catalano, O., Scuderi, S., et al. 2020, Astronomy and Astrophysics, 634, A22

Long, K. S., Blair, W. P., Vancura, O., et al. 1992, The Astrophysical Journal, 400, 214

Longair, M. S. 2011, High Energy Astrophysics (Cambridge University Press)

Loru, S., Pellizzoni, A., Egron, E., et al. 2021, Monthly Notices of the Royal Astronomical Society, 500, 5177

Maeda, K., Kawabata, K., Mazzali, P. A., et al. 2008, Science, 319, 1220

Malkov, M. A., Diamond, P. H., & Sagdeev, R. Z. 2011, Nature Communications, 2, 194

Malkov, M. A. & Drury, L. O. 2001, Reports on Progress in Physics, 64, 429

Marek, A. & Janka, H.-T. 2009, The Astrophysical Journal, 694, 664

Mattox, J. R., Bertsch, D. L., Chiang, J., et al. 1996, The Astrophysical Journal, 461, 396

McKee, C. F. 1974, The Astrophysical Journal, 188, 335

Medina, A. A., Raymond, J. C., Edgar, R. J., et al. 2014, The Astrophysical Journal, 791, 30

Miceli, M., Bocchino, F., & Reale, F. 2008, The Astrophysical Journal, 676, 1064

Miceli, M., Orlando, S., Burrows, D. N., et al. 2019, Nature Astronomy, 3, 236

Miceli, M., Orlando, S., Pereira, V., et al. 2016, Astronomy and Astrophysics, 593, A26

Miceli, M., Orlando, S., Reale, F., Bocchino, F., & Peres, G. 2013, Monthly Notices of the Royal Astronomical Society, 430, 2864

Miceli, M., Reale, F., Orlando, S., & Bocchino, F. 2006, Astronomy and Astrophysics, 458, 213

Mignone, A., Bodo, G., Massaglia, S., et al. 2007, The Astrophysical Journal, 170, 228

Milisavljevic, D. & Fesen, R. A. 2013, The Astrophysical Journal, 772, 134

Morlino, G. & Caprioli, D. 2012, Astronomy and Astrophysics, 538, A81

Nadyozhin, D. K. 1994, The Astrophysical Journal Supplement, 92, 527

Nagataki, S. 2000, The Astrophysical Journal Supplement, 127, 141

Nagataki, S., Hashimoto, M.-a., Sato, K., & Yamada, S. 1997, The Astrophysical Journal, 486, 1026

Nagataki, S., Hashimoto, M.-a., Sato, K., Yamada, S., & Mochizuki, Y. S. 1998, The Astrophysical Journal Letters, 492, L45

Nakamura, K., Takiwaki, T., Kuroda, T., & Kotake, K. 2015, Publications of the Astronomical Society of Japan, 67, 107

Oakley, P., McEntaffer, R., & Cash, W. 2013, The Astrophysical Journal, 766, 51

O'Connor, E. P. & Couch, S. M. 2018, The Astrophysical Journal, 865, 81

Ono, M., Nagataki, S., Ferrand, G., et al. 2020, The Astrophysical Journal, 888, 111

Ono, M., Nagataki, S., Ito, H., et al. 2013, The Astrophysical Journal, 773, 161

Orlando, S., Bocchino, F., Miceli, M., Petruk, O., & Pumo, M. L. 2012, The Astrophysical Journal, 749, 156

Orlando, S., Bocchino, F., Reale, F., Peres, G., & Pagano, P. 2008, The Astrophysical Journal, 678, 274

Orlando, S., Miceli, M., Petruk, O., et al. 2019, Astronomy and Astrophysics, 622, A73

Orlando, S., Miceli, M., Pumo, M. L., & Bocchino, F. 2015, The Astrophysical Journal, 810, 168

Orlando, S., Miceli, M., Pumo, M. L., & Bocchino, F. 2016, The Astrophysical Journal, 822, 22

Orlando, S., Ono, M., Nagataki, S., et al. 2020, Astronomy and Astrophysics, 636, A22

Orlando, S., Peres, G., Reale, F., et al. 2005, Astronomy and Astrophysics, 444, 505

Parizot, E., Marcowith, A., Ballet, J., & Gallant, Y. A. 2006, Astronomy and Astrophysics, 453, 387

Park, S., Hughes, J. P., Slane, P. O., et al. 2004, The Astrophysical Journal Letters, 602, L33

Parker, E. N. 1958, The Astrophysical Journal, 128, 664

Patnaude, D. J., Lee, S.-H., Slane, P. O., et al. 2015, The Astrophysical Journal, 803, 101

Phan, V. H. M., Morlino, G., & Gabici, S. 2018, Monthly Notices of the Royal Astronomical Society, 480, 5167

Potter, T. M., Staveley-Smith, L., Reville, B., et al. 2014, The Astrophysical Journal, 794, 174

Pumo, M. L. & Zampieri, L. 2011, The Astrophysical Journal, 741, 41

Raymond, J. C., Chilingarian, I. V., Blair, W. P., et al. 2020, The Astrophysical Journal, 894, 108

Raymond, J. C., Edgar, R. J., Ghavamian, P., & Blair, W. P. 2015, The Astrophysical Journal, 805, 152

Raymond, J. C., Ghavamian, P., Sankrit, R., Blair, W. P., & Curiel, S. 2003, The Astrophysical Journal, 584, 770

Reed, J. E., Hester, J. J., Fabian, A. C., & Winkler, P. F. 1995, The Astrophysical Journal, 440, 706

Rho, J. & Petre, R. 1998, The Astrophysical Journal Letters, 503, L167

Romano, P., Böttcher, M., Foschini, L., et al. 2020, Monthly Notices of the Royal Astronomical Society, 494, 411

Romano, P., Vercellone, S., Foschini, L., et al. 2018, Monthly Notices of the Royal Astronomical Society, 481, 5046

Sankrit, R., Raymond, J. C., Bautista, M., et al. 2014, The Astrophysical Journal, 787, 3

Sano, H., Sato, J., Horachi, H., et al. 2010, The Astrophysical Journal, 724, 59

Scuderi, S. 2019, in European Physical Journal Web of Conferences, Vol. 209, European Physical Journal Web of Conferences, 01001

Sedov, L. I. 1959, Similarity and Dimensional Methods in Mechanics

Shikaze, Y., Haino, S., Abe, K., et al. 2007, Astroparticle Physics, 28, 154

Shin, M.-S., Stone, J. M., & Snyder, G. F. 2008, The Astrophysical Journal, 680, 336

Siegert, T., Diehl, R., Krause, M. G. H., & Greiner, J. 2015, Astronomy and Astrophysics, 579, A124

Sottile, G., Catalano, O., La Rosa, G., et al. 2016, in Society of Photo-Optical Instrumentation Engineers (SPIE) Conference Series, Vol. 9906, Ground-based and Airborne Telescopes VI, ed. H. J. Hall, R. Gilmozzi, & H. K. Marshall, 99063D

Strong, A. W., Moskalenko, I. V., & Reimer, O. 2004, The Astrophysical Journal, 613, 962

Su, Y., Fang, M., Yang, J., Zhou, P., & Chen, Y. 2014, The Astrophysical Journal, 788, 122

Sukhbold, T., Ertl, T., Woosley, S. E., Brown, J. M., & Janka, H.-T. 2016, The Astrophysical Journal, 821, 38

Sun, X. H., Reich, W., Han, J. L., Reich, P., & Wielebinski, R. 2006, Astronomy and Astrophysics, 447, 937

Takiwaki, T., Kotake, K., & Sato, K. 2009, The Astrophysical Journal, 691, 1360

Tanaka, T., Uchiyama, Y., Aharonian, F. A., et al. 2008, The Astrophysical Journal, 685, 988

Tang, X. 2019, Monthly Notices of the Royal Astronomical Society, 482, 3843

Tang, X. & Chevalier, R. A. 2015, The Astrophysical Journal, 800, 103

Tavani, M., Barbiellini, G., Argan, A., et al. 2009, Astronomy and Astrophysics, 502, 995

Tavani, M., Giuliani, A., Chen, A. W., et al. 2010, The Astrophysical Journal Letters, 710, L151

Taylor, G. 1950, Proceedings of the Royal Society of London Series A, 201, 159

Tessore, B., Lèbre, A., Morin, J., et al. 2017, Astronomy and Astrophysics, 603, A129

The Pierre Auger Collaboration. 2015, arXiv e-prints, arXiv:1502.01323

Thorstensen, J. R., Fesen, R. A., & van den Bergh, S. 2001, The Astronomical Journal, 122, 297

Tibet ASγ Collaboration, Amenomori, M., Bao, Y. W., et al. 2021, Nature Astronomy

Troja, E., Bocchino, F., Miceli, M., & Reale, F. 2008, Astronomy and Astrophysics, 485, 777

Troja, E., Bocchino, F., & Reale, F. 2006, The Astrophysical Journal, 649, 258

Truelove, J. K. & McKee, C. F. 1999, The Astrophysical Journal Supplement, 120, 299

Tsebrenko, D. & Soker, N. 2015, Monthly Notices of the Royal Astronomical Society, 453, 166

Tsuji, N., Uchiyama, Y., Aharonian, F., et al. 2019, The Astrophysical Journal, 877, 96

Tutone, A., Ballet, J., Acero, F., D'Aì, A., & Cusumano, G. 2021, arXiv e-prints, arXiv:2109.15238

Tutone, A., Orlando, S., Miceli, M., et al. 2020, Astronomy and Astrophysics, 642, A67

Uchida, H., Tsunemi, H., Katsuda, S., et al. 2009, Publications of the Astronomical Society of Japan, 61, 503

Uchiyama, Y., Aharonian, F. A., Tanaka, T., Takahashi, T., & Maeda, Y. 2007, Nature, 449, 576

Uchiyama, Y., Blandford, R. D., Funk, S., Tajima, H., & Tanaka, T. 2010, The Astrophysical Journal Letters, 723, L122

Uchiyama, Y., Funk, S., Katagiri, H., et al. 2012, The Astrophysical Journal Letters, 749, L35

Ustamujic, S., Orlando, S., Greco, E., et al. 2021, Astronomy and Astrophysics, 649, A14

Utrobin, V. P., Chugai, N. N., & Andronova, A. A. 1995, Astronomy and Astrophysics, 295, 129

Utrobin, V. P., Wongwathanarat, A., Janka, H.-T., & Müller, E. 2015, Astronomy and Astrophysics, 581, A40

Uyanıker, B., Reich, W., Yar, A., & Fürst, E. 2004, Astronomy and Astrophysics, 426, 909

Uyanıker, B., Reich, W., Yar, A., Kothes, R., & Fürst, E. 2002, Astronomy and Astrophysics, 389, L61

Vassiliev, V., Fegan, S., & Brousseau, P. 2007, Astroparticle Physics, 28, 10

Vink, J. 2012, The Astronomy and Astrophysics Review, 20, 49

Völk, H. J., Berezhko, E. G., & Ksenofontov, L. T. 2008, Astronomy and Astrophysics, 483, 529

Wakely, S. P. & Horan, D. 2008, International Cosmic Ray Conference, 3, 1341

Wang, C.-Y. 2011, Monthly Notices of the Royal Astronomical Society, 415, 83

Wang, C.-Y. & Chevalier, R. A. 2001, The Astrophysical Journal, 549, 1119

Wang, C.-Y. & Chevalier, R. A. 2002, The Astrophysical Journal, 574, 155

Weekes, T. C., Badran, H., Biller, S. D., et al. 2002, Astroparticle Physics, 17, 221

Weekes, T. C., Cawley, M. F., Fegan, D. J., et al. 1989, The Astrophysical Journal, 342, 379

Welsh, B. Y. & Sallmen, S. 2003, Astronomy and Astrophysics, 408, 545

Woltjer, L. 1972, Annual Review of Astronomy and Astrophysics, 10, 129

Wongwathanarat, A., Janka, H. T., & Müller, E. 2013, Astronomy and Astrophysics, 552, A126

Wongwathanarat, A., Janka, H.-T., Müller, E., Pllumbi, E., & Wanajo, S. 2017, The Astrophysical Journal, 842, 13

Xin, Y., Zeng, H., Liu, S., Fan, Y., & Wei, D. 2019, The Astrophysical Journal, 885, 162

Yu, H., Wu, K., Wen, L., & Fang, J. 2022, , 90, 101669

Zabalza, V. 2015, Proc. of International Cosmic Ray Conference 2015, 922

Zirakashvili, V. N. & Aharonian, F. A. 2010, The Astrophysical Journal, 708, 965